December 1994 Report No. UMCEE 94-35

ELECTRORHEOLOGICAL DAMPERS FOR STRUCTURAL VIBRATION SUPPRESSION

by

Henri P. Gavin

Robert D. Hanson

A report on research sponsored by
National Science Foundation
Grant No. NSF-BCS-9201787

The Department of Civil and Environmental Engineering
The University of Michigan
Ann Arbor, Michigan 49109-2125

ACKNOWLEDGEMENTS

The author thanks the National Science Foundation for providing the financial resources to conduct the research described in this report. This report is, in essence, the doctoral dissertation of Henri P. Gavin. This dissertation was supported financially by a grant from the National Science Foundation under Award No. BCS-9201787 as part of the Coordinated USA Research Program on Structural Control for Safety, Performance, and Hazard Mitigation. Any opinions, findings, and conclusions or recommendations expressed in this publication are those of the author and do not necessarily reflect the views of the National Science Foundation.

The contributions of Professors Hanson, McClamroch, Filisko, and Peek to this work are gratefully acknowledged. It is a privilege and an inspiration to be associated with internationally renowned leaders in their fields.

Professor Hanson's skills go beyond his technical knowledge of earthquake engineering and his ability to extract the most important mechanisms from very complicated systems. He is a consummate organizer, leader, and mediator. I am indebted to him for providing me an opportunity to work in structural control, for his mentorship, and for his expert guidance.

Extensive discussions with Professor Filisko contributed largely to my concept of ER materials. His explanations of the intricacies of these materials, and his wealth of vivid analogies for their behavior, gave me a perspective that can not be obtained from the minutiae reported in technical journals.

I doubt that I could exhaust the ever-expanding capabilities of Michigan's Computer Aided Engineering Network (CAEN). Amadi Nwankpa, at CAEN's User Services, has found the solution to my computer problems on numerous occaisons. The University's computer, library, and laboratory facilities are a tremendous asset; but the quality, depth, and availability of its faculty and technical staff are its greatest resource. On numerous occasions, a brief, clear, and insightful discussion with a faculty member has saved me from weeks of library work. In this regard, I would like to acknowledge Professors D.S. Bernstein, G.B. Brereton, S. Ceccio, P.L. Duren, S.K. Jain, N.D. Katopodes, W.J. Williams, A.S. Wineman, and especially my committee members. As anyone who does lab work knows, experiments can not be run without capable technical assistance. For this I thank Bob Fischer, Bob Spence, and Dave Bigelow.

Robin, my wife and companion, has given me nothing but encouragement in this endeavor. Her unwavering support, even during the grimmest periods, made the occasional drudgery a joy.

TABLE OF CONTENTS

ACKNOWLEDGEMENTS ii

LIST OF FIGURES vii

LIST OF SYMBOLS xii

LIST OF APPENDICES xv

CHAPTER

I. INTRODUCTION 1

1.1 Electrorheological Materials 2
1.1.1 Macroscopic Properties 2
1.1.2 Electrorheological Mechanisms 4
1.1.3 Composition of ER Materials 5
1.1.4 Anhydrous ER Materials 5
1.2 The Flow of ER Materials in Vibration Control Devices . . . 7
1.3 Approaches to Control 7
1.4 Organization of the Thesis 9

II. THE EMERGENCE OF ELECTRORHEOLOGY 12

2.1 An Overview of the ER effect 12
2.2 Early Observations 17
2.3 Modern ER Materials 22
2.4 Visco-elastic Behavior 26
2.5 Post-Yielding Behavior 29
2.5.1 Observation of Post-Yield Behavior 32
2.5.2 Micro-mechanical Simulations 34
2.6 Response Times of ER Suspensions 41
2.7 Summary 45

III. THE FLOW OF ELECTRORHEOLOGICAL FLUIDS 48

3.1 Poiseuille Flow of Electrorheological Fluids 48

3.1.1 Non-dimensional Forms 52
3.1.2 Solutions of the Dimensionless Poiseuille Flow Equations 54
3.2 ER Flow Transients 57
3.2.1 The Bingham-to-Newtonian Transient 57
3.2.2 Entrance Effects 62
3.2.3 Measurement and Analysis of ER Flow Transients . 63
3.3 Bingham Flow in Other Geometries 64
3.4 Measuring Yield Stresses 68
3.5 Summary 70

IV. ER DEVICES 73

4.1 Applications of ER Materials 73
4.1.1 Shear Mode 74
4.1.2 Flow Mode 74
4.1.3 Mixed Mode 76
4.1.4 Control of Visco-elastic Properties 77
4.1.5 Wear and Durability Properties of ER Materials . . 78
4.2 Vibration Actuators 78
4.3 Engine Mounts 81
4.4 Vehicle Suspensions 84
4.5 Clutches 87
4.6 High Voltage Control 88
4.7 Summary 88

V. MODELING OF ER FLUID DAMPERS 90

5.1 Parametric Models 91
5.2 Non-Parametric Models 92
5.2.1 Chebyshev Polynomial Approximation 93
5.2.2 Modeling ER Devices for Simulation and Control . . 97
5.2.3 Other Polynomial Bases 98
5.3 Summary 99

VI. DESIGN, TESTING, AND MODELING OF MIXED-MODE ER FLUID DAMPERS 100

6.1 Device Design and Analysis 101
6.2 Small Scale Device 104
6.2.1 Dimensions, Materials, and Test Configuration . . . 104
6.2.2 Constant Voltage Tests 109
6.2.3 Variable Voltage Tests 116
6.3 Large Scale Device 120

6.3.1 Dimensions, Materials, and Test Configuration . . . 120
6.3.2 Experimental Data . . . 122
6.3.3 Non-Parametric Modeling . . . 127
6.4 Summary . . . 136

VII. SUMMARY AND CONCLUSIONS . . . 137

7.1 ER Materials . . . 137
7.2 Semi-Active Damping Devices . . . 138
7.2.1 Design . . . 138
7.2.2 Modeling . . . 140
7.2.3 Control . . . 141
7.3 Future Work . . . 142
7.3.1 ER Flow in a Concentric Annulus . . . 142
7.3.2 Horizontal Flow with a Free Surface . . . 142
7.3.3 Structural Control Experiments . . . 143

APPENDICES . . . 145

BIBLIOGRAPHY . . . 171

LIST OF FIGURES

Figure		
1.1	Qualitative stress - strain behavior of ER materials.	3
1.2	Qualitative stress - strain rate behavior of ER materials.	4
2.1	Variation of point dipole interaction force with φ.	14
2.2	A mechanical analogue for ER materials.	26
2.3	Variation of elastic strain energy, U, with shear strain γ for visco-elastic - plastic ER behavior.	38
3.1	Poiseuille flow of Bingham materials.	49
3.2	Six possible stress conditions and the resulting velocity profiles.	51
3.3	Solution to the cubic Bingham flow equation.	55
3.4	Error of the approximation to the exact solution of the cubic Bingham flow equation.	55
3.5	Dynamic range, P, as a function of gap size, h, and flow rate, Q.	56
3.6	Development of a Newtonian flow profile from a Bingham flow profile.	58
3.7	Flow transient from Bingham to Newtonian behavior.	61
3.8	Dynamic range, P, as a function of response time, $\hat{t}$, and flow rate, Q.	61
3.9	Bingham flow between diverging parallel walls.	65
3.10	The bi-viscosity constitutive model.	66
3.11	Static and dynamic yield stresses in flowing ER materials.	69

4.1 A shear-mode ER device. 75

4.2 A flow-mode ER device. 76

4.3 A mixed-mode ER device. 77

4.4 A bi-directional ER vibration actuator. 79

4.5 An ER fluid-inertia engine mount. 81

4.6 Free body digram of an ER fluid-inertia engine mount. 82

4.7 Adjustable dynamic stiffness of a fluid inertia engine mount. 83

5.1 The first six Chebyshev polynomials $T_n(x) = \cos(n \arccos(x))$ 93

5.2 Zeros of the product of two 10th degree Chebyshev polynomials, $T_{10}(x)T_{10}(y)$. 95

6.1 Variation of $\frac{V}{6A}$ with T and V. 104

6.2 Shear thinning behavior of the ER materials used in the small device: (a) τ v. $\dot{\gamma}$ for 0 kV/mm $< E <$ 4 kV/mm, (b) τ_y v. E for 0.0048/sec $< \dot{\gamma} <$ 0.48/sec. 105

6.3 Configuration of the small-scale ER test device. 107

6.4 Configuration of the small test device, hydraulic actuator, high voltage supply, data acquisition, and control. 108

6.5 Applied test motions for the small ER device at a constant electric field. The period of the sinusoidal motion in this test is 3 seconds. . 110

6.6 Experimental ER hysteresis loops at constant voltages ($E = 0.0$ kV/mm and $E = 3.34$ kV/mm) and increasing sinusoidal amplitudes (1.2 sec. sinusoidal period, $h = 2.38$ mm). 111

6.7 Experimental ER hysteresis loops at constant voltages ($E = 0.0$ kV/mm and $E = 2.50$ kV/mm) and increasing sinusoidal amplitudes (1.2 sec. sinusoidal period, $h = 0.96$ mm). 111

6.8 Experimental ER hysteresis loops at constant voltages ($E = 0.0$ kV/mm and $E = 3.34$ kV/mm) and increasing sinusoidal amplitudes (3.0 sec. sinusoidal period, $h = 2.38$ mm). 112

6.9 Experimental ER hysteresis loops at constant voltages ($E = 0.0$ kV/mm and $E = 2.50$ kV/mm) and increasing sinusoidal amplitudes (3.0 sec. sinusoidal period, $h = 0.96$ mm). 112

6.10 Experimental ER hysteresis loops at constant voltages ($E = 0.0$ kV/mm and $E = 3.34$ kV/mm) and increasing sinusoidal amplitudes (6.0 sec. sinusoidal period, $h = 2.38$ mm). 113

6.11 Experimental ER hysteresis loops at constant voltages (E =0.0 kV/mm and $E = 2.50$ kV/mm) and increasing sinusoidal amplitudes (6.0 sec. sinusoidal period, $h = 0.96$ mm). 113

6.12 Quantitative evaluation of the Bingham flow equations for ER materials: (a) h=0.96 mm (b) h=2.38 mm. 114

6.13 Experimental ER pressure response and the pressure response of a corresponding Bingham material. ($E = 2.92$ kV/mm) and increasing sinusoidal amplitudes (6.0 sec. sinusoidal period, $h = 2.38$ mm). . . 115

6.14 Applied test motions for the small ER device at variable electric fields. The period of the constant velocity motion in this test is 6 seconds. 116

6.15 Applied electric field for the small ER device at variable electric fields. The period of the electric field application in this test is 3 seconds. . 117

6.16 Effect of the high voltage relay on transient electric fields. 117

6.17 Effect of the high voltage relay on ER pressure transients. 118

6.18 Transient pressure responses for an actual ER fluid: — and an ideal inertialess Bingham fluid: - - - -. (a) $h = 0.96$ mm, $E = 2.21$ kV/mm (b) $h = 2.38$ mm, $E = 1.57$ kV/mm. 119

6.19 Configuration of the large test device and hydraulic actuator. 121

6.20 Hysteresis loops from initial tests using a mineral oil based ER fluid. The period of the sinusoidal motion in this test was 14.3 seconds. . 123

6.21 Displacement based hysteresis loops from initial tests using a kerosene based fluid. The period of the sinusoidal motion in this test was 9.1 seconds. 125

6.22 Velocity based hysteresis loops from initial tests using a kerosene based fluid. The period of the sinusoidal motion in this test was 9.1 seconds. 125

6.23 Shear thinning behavior of the ER materials used in the large device: (a) τ v. $\dot{\gamma}$ for 0 kV/mm $< E <$ 6 kV/mm (b) τ_y v. E for 0.142/sec $< \dot{\gamma} <$ 45/sec. 126

6.24 Applied test motions for the large ER device at a constant electric field. The period of the sinusoidal motion in this test was 4.3 seconds. 127

6.25 Effect of amplitude of motion and electric field on the equivalent damping ratio, c_{eq}. The period of the sinusoidal motion in this test was 4.3 seconds. 128

6.26 (a) Analytical and (b) experimental hysteresis loops for an electro-rheological damper at low and high electric fields. 129

6.27 Convergence of $\hat{f}$ to f with increasing I, J, K and P, Q, R. 130

6.28 Non-parametric estimation of ER damper force (data—, curve-fit– –) 0.0 kV/mm 131

6.29 Non-parametric estimation of ER damper force (data—, curve-fit– –) 3.2 kV/mm 131

6.30 Error surface of $f(x, \dot{x}) - \hat{f}(x, \dot{x})$ at $E = 3.2$ kV/mm. 132

6.31 Irregular applied test motions for the large ER device at a constant electric field. 133

6.32 Prediction of ER forces based on a previous test at 0.0 kV/mm . . . 134

6.33 Prediction of ER forces based on a previous test at 3.2 kV/mm . . . 134

6.34 Prediction of ER displacement hysteresis based on a previous test at 3.2 kV/mm 135

6.35 Prediction of ER damper forces at $E = 1.3$ kV/mm, based on tests at 0.0, 0.6, 1.9, 2.4, and 3.2 kV/mm. 135

A.1 The electric field, $E(r, \varphi)$, due to a point dipole, $p = aq$. 147

A.2 Two aligned point dipoles. 148

B.1 Variation of dimensionless pressure gradient, P, with yield stress, T. Solid line: exact, Dashed line: approximation 156

B.2 Approximation errors of $P \approx 1 + 2.07T + T/(1 + 0.4T)$ to the exact solution, $P_1(T)$. 156

B.3 Variation of dimensionless pressure gradient, P, with wall velocity, V, and yield stress, T. —: numerical solution, - - - -: closed form approximation 161

B.4 Approximation errors of $P \approx 1 - V + 2.07T + \frac{T}{1+0.4T} - \frac{1.5TV^2}{1+0.4T^2}$ to the numerical solution. 161

B.5 Verification of the inequality $|V| \leq \frac{3A^2}{P}$ for small T. $\frac{1}{2} < \frac{3A^2}{P}$ when $P(T, V)$ is above the line labeled: $P >$ - - - -. 162

B.6 Verification of the inequality $|V| \leq \frac{3A^2}{P}$ for large T. $\frac{1}{2} < \frac{3A^2}{P}$ when $P(T, V)$ is above the line labeled: $P >$ - - - -. 162

B.7 Damper velocity for the parameter estimation 165

B.8 Calculated pressure gradient 165

B.9 Identified Yield Stress, τ_y. 166

B.10 Identified viscosity, η 166

LIST OF SYMBOLS

A	dimensionless excess pressure
a	charge separation distance in a point dipole
b	wide dimension of a rectangular duct, the duct width
C	Coulomb, unit of electrical charge
°C	degrees Centigrade
C, c	coefficients of a polynomial expansion
c_{r}	damping rate of the rubber bearing in an engine mount model
c_{f}	damping rate of the fluid in an engine mount model
D_k	coefficients of the Fourier expansion used to solve (3.26)
E	the electric field component normal to the electrodes
$\hat{E}$	an approximated electric field
E_{i}	electric field inside of a spherical particle
E_{o}	un perturbed electric field far from an isolated particle
e	average relative root mean square error
F	Farad, unit of capacitance
f	an analytically evaluated or interpolated force
$\hat{f}$	an approximation to f
h	narrow dimension of a rectangular duct, the gap size
h_{i}	the gap size in the inner gap of a parallel plate damper
h_{o}	the gap size in the outer gap of a parallel plate damper
J_2, J_∞	the Euclidean norm, and the infinity norm
j	$\sqrt{-1}$
K	an empirical constant relating Mn^* to ϕ
kV	kilo-Volt, unit of voltage
kW	kilo-Watt, unit of power
k_{b}	stiffness of the bottom rubber housing in an engine mount
k_{er}	dielectric constant of the ER suspension
k_{f}	dielectric constant of the dispersant
k_{p}	dielectric constant of the particulate
k_{r}	stiffness of the rubber bearing in an engine mount
k_{t}	stiffness of the rubber bearing in an engine mount which acts on the fluid in the mount
l	length of the plates in a parallel plate damper (in the direction of motion)
Mn	the Mason number: the ratio of viscous to electrostatic stresses.

Mn^*	critical Mason number, marks the transition to viscous flow
m, mm,	meter, milli-meter, units of length
ms,	milli-second, unit of time
m_f	inertia in a fluid inertia engine mount
N	Newton, unit of force
N	the number of plates in a parallel plate dash-pot damper
n	an exponent used in various equations
P	dimensionless pressure gradient, the dynamic range
Pa	Pascal, N/m^2, unit of pressure
p	point dipole strength
p'	pressure gradient, $-\frac{\partial p}{\partial x}$, of a fluid with an arbitrary yield stress
p'_N	pressure gradient, $-\frac{\partial p}{\partial x}$, of a Newtonian fluid
Q	total (shear and pressure driven) volumetric flow rate
Q_i	volumetric flow rate in an inner duct of a parallel plate dash-pot
Q_o	volumetric flow rate in an outer duct of a parallel plate dash-pot
Q_s	shear-driven volumetric flow rate
q	the value of a point charge
r	radial position of a point dipole
$\hat{r}$	unit vector in the radial direction
T	Chapter III, B: the dimensionless yield stress Chapter V: the number of sampled points, $(t = 1, \ldots, T)$.
T_i	the i^{th} Chebyshev polynomial
T_w	the dimensionless wall stress
$\mathbf{T}$	deviatoric portion of the stress tensor
$\mathcal{T}(t)$	separated variable for solution of the p.d.e. (3.26)
t	time, Chapter VI: plate thickness
t^*	characteristic time scale for ER material property changes
$\hat{t}$	characteristic time scale for the Bingham-to-Newtonian flow transient
t_c	column formation time
U	the velocity of one duct wall with respect to the other duct wall
U_0	mean flow velocity along the axis of the duct
$\mathcal{U}$	elastic strain energy of a fibril of ER particles
u	Chapter II, A: point dipole pair interaction energy Chapter III, B: flow velocity along the axis of the duct
u_h	homogeneous solution to the p.d.e.(3.26)
u_p	particular solution to the p.d.e. (3.26)
V	Volt, unit of voltage
V	dimensionless wall velocity
V_f	mean fluid velocity through a duct
v	flow velocity across the axis of the duct
x	coordinate along the axis of the duct
x_1, x_2	coordinates of the 2DOF model of an engine mount
x_p, y_q, z_r	the roots of $T_P(x)$, $T_Q(y)$, and $T_R(z)$.
$\mathcal{Y}(y)$	separated variable for solution of the p.d.e. (3.26)

y	coordinate across the axis of the duct
y_1, y_2	coordinates where $\|\tau\| = \|\tau_y\|$, $(y_1 \leq y_2)$
α_i	coefficients to a generalized constitutive model
β	particle dipole coefficient: a measure of the polarizability of a particle
ϵ_0	the permittivity of free space
γ	shear strain
$\dot{\gamma}_w$	shear strain rate at the wall $(y = 0)$
γ_y	yield shear strain
η	viscosity of the ER material
η_0	large viscosity in a bi-viscosity model
η_1	small viscosity in a bi-viscosity model
η_{app}	apparant viscosity, $\tau/\dot{\gamma}$
η_c	viscosity of the dispersant (continuous phase)
Φ	electro-static potential
ϕ	volume fraction of the particulates in the ER suspension
$\phi_i(x)$	the i^{th} orthogonal function of x
φ	angular position of a point dipole
$\hat{\varphi}$	unit vector in the angular direction
λ	eigenvalue of the p.d.e. (3.26)
θ	Chapter II: temperature, Appendix B: angle
ρ	density
$\sigma_{11}, \sigma_{22}, \sigma_{33}$	normal stresses
τ, τ_{12}	shear stress
τ_0, τ_1	fictitious yield stresses in the bi-viscosity model
τ_w	shear stress at the wall $(y = 0)$
τ_y	yield shear stress
Ω	the domain of an approximation
ω	frequency in radians per second

LIST OF APPENDICES

Appendix

A. Point Dipole Interactions and Dielectric Polarization of Spheres 146

A.1 Interaction Energy of Two Aligned Point Dipoles of Identical Strength 146
A.2 Dielectric Polarization of Spheres 149

B. Solution of the Poiseuille Flow Equations 153

B.1 Analytic Solution for Fixed Walls 153
B.1.1 Simulation: $P(T)$ 154
B.1.2 Identification: $T(P)$ 157
B.2 Numerical Solutions and an Approximation for Moving Walls 158
B.2.1 Simulation: $P(T, V)$ 159
B.2.2 Identification: $T(P, V)$ 162
B.3 Estimating Parameters τ_y and η from Experimental Data . . 163
B.4 Summary 167

C. A Note on Chebyshev Polynomials 168

CHAPTER I

INTRODUCTION

Whether playing a musical instrument, driving a car, walking or even breathing, we use our senses to perceive the effects of our actions and to intelligently modify our behavior to achieve a desired result. Our actions are almost always modified by feedback information (sensory, verbal, or otherwise). In performing motor coordination tasks, for example, we often use sight and touch to decide how far to move, or how hard to push. The control of our motor functions is similar to the control of structural systems in that muscles are analogous to force generating actuators.

Controlling structures with actuators is intuitively appealing because it not unlike controlling our muscular motor functions. However, actuating internal forces is not the only possible method for modifying structural behavior. Unlike muscular-skeletal systems, structural elements can have adjustable physical properties, such as stiffness or damping. Intelligent adjustment of the properties of such *semi-active* members can be used to satisfy structural control objectives, such as reducing the vibrational energy of a structure. The operation of semi-active members requires insignificant amounts of power as compared to the operation of fully active force actuated members, i.e., hydraulic actuators.

Materials with properties which can change as a function of an electrical stimulus

are attractive candidates for use in semi-active control members. Electrorheological (ER) materials exhibit dramatic changes in behavior when subjected to strong electric fields. As the electric field through an ER material increases, the yield stress, stiffness, and viscous damping increase. Order of magnitude changes in these properties occur in a matter of milli-seconds and these changes are reversed as soon as the electric field is discharged.

This dissertation describes ER materials and their use in dampers for structural vibration control. Not all devices using ER materials can be classified as dampers. ER materials also offer the possibility of semi-active variable stiffness devices.

1.1 Electrorheological Materials

1.1.1 Macroscopic Properties

Electrorheological (ER) materials are suspensions of unique micron-sized particles in hydrophobic, insulating, dielectric oils. The mechanical properties of these materials (stiffness, damping, and yielding behavior) can be controlled by regulating an electric field through them. These material properties can change almost as fast as the applied electric field can be switched. Typical material response times are on the order of 1–10 milli-seconds. Changes in properties are completely and immediately reversible. At high electric fields and low levels of strain, ER materials are essentially visco-elastic plastic materials [99, 100]. The stiffness properties (shear and tensile moduli), the yield stresses, and the yield strains are strongly dependent on the electric field. At pre-yield strains, linear viscosity increases dramatically with the electric field. Yield strains typically decrease with the electric field and yield stresses increase roughly quadratically with the electric field. An accompanying dramatic increase in pre-yield stiffness follows from this behavior. Figure 1.1 illustrates

the qualitative stress-strain behavior, and gives ultimate values of yield stresses, τ_y, and yield strains, γ_y.

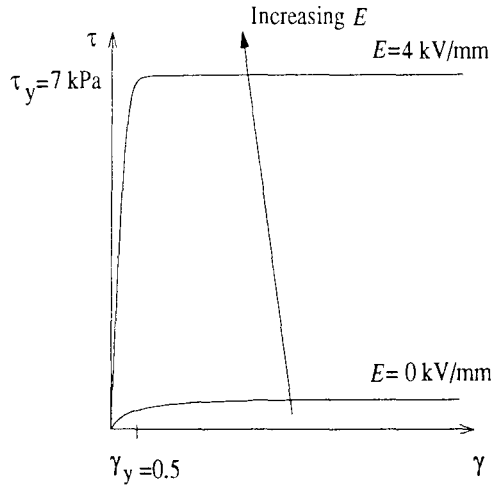

Figure 1.1: Qualitative stress - strain behavior of ER materials.

In fully developed flow, an electric field dependent yield stress can conveniently model the energy dissipation mechanisms. In this situation, an applied shear stress is resisted by both a yielding mechanism and a Newtonian viscous mechanism. At low shear rates, the energy dissipation is primarily a frictional or Coulomb damping effect [99, 100]. The Newtonian viscosity is roughly independent of the applied electric field. Figure 1.2 illustrates the qualitative macroscopic behavior of ER materials in steady flow and at large deformations. The primary features of flowing ER materials are:

- The dominant damping mechanism changes from viscous to Coulomb damping at high electric fields, and large deformations.

- The yield strength varies with the square of the electric field.

The highly controllable yielding nature of these materials can be exploited in the design of controllable damping devices.

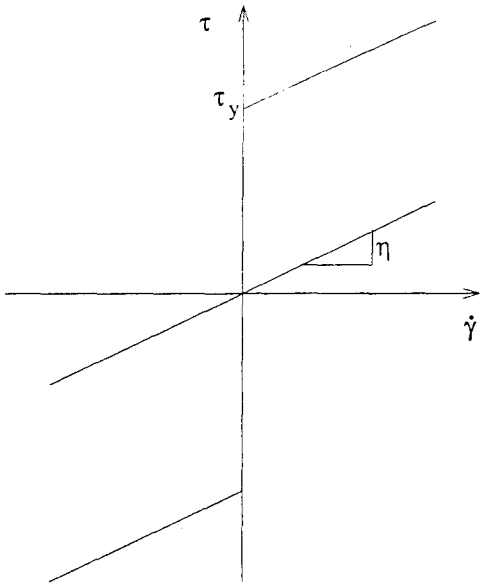

Figure 1.2: Qualitative stress - strain rate behavior of ER materials.

1.1.2 Electrorheological Mechanisms

The basis of the ER effect has been attributed to the induced polarization of the dispersed particles of a colloid or the dissolved phase of a solution [28]. The polarization of the dispersed phase of the substrate can be accomplished via several types of charge migration in or on the particles. Independent parameters, such as the permittivity,[1] dielectric loss, mobile ion concentration, polar surfactant concentration, field strength, shear rate, and temperature all play a role in the ER effect [28]. Under increasing shear deformations, charged particles are forced to overcome their electrostatic attraction. Inter-particle interaction energies are enhanced when ionic double layers overlap. During flow, the charged particles experience a force mutually orthogonal to the stream and field lines. The resulting across-stream flow of the particles dissipates energy. The electrostatic attraction of the polarized particles

[1] Permittivity is a material property relating the electrostatic force between two point charges in the material to their magnitudes and separation distance. This property determines the amount of work dissipated by interacting charged particles in an ER material.

does not account for the entire observed effect. The measured viscosities and yield stresses are, in fact, greater than electrostatic forces alone can predict [93].

1.1.3 Composition of ER Materials

The composition of ER materials can vary widely. The level of ER activity (a wide range of controllable properties, high dielectric strength, and low current densities) depends strongly on the material's constitutive parts, and on the synthesis procedure. Suspensions as simple as corn starch in cooking oil will exhibit an ER effect. The hydrophilic nature of corn-starch[2] and the polar nature of water molecules is a likely source of ER activity in such materials. The conductance of moist ER materials, or ER materials with mobile ions, limits their potential use. Water adsorbed into the dispersed phase of these ER materials allows electrical currents to flow between the electrodes. Current in moist ER materials can be conducted through a dielectric breakdown of the fluid, charge transfer between particles themselves, and charge tunneling in the gaps between the particles. Significant power is therefore required to produce the required electric fields. As the materials conduct electricity, they become hotter. Water is driven off by iR heating as well as through electrolysis. Moist ER materials become more conductive as they heat up. The concentration of the activating ingredient (water) in these materials is therefore very difficult to control.

1.1.4 Anhydrous ER Materials

Discoveries in the late 1980's of anhydrous electrorheologically active materials led to a significant increase in ER research, and portended the advent of a new and potentially lucrative industry. The particles in these modern materials are typically

[2]The corn starch found on grocery store shelves is about 20% water in the box.

dried zeolites or amorphous alumino-silicates. Unlike water-based materials (whose particles become polarized through an ionic double layer surrounding the particle), mobile ions, intrinsic to the particle, polarize these anhydrous zeolites. Zeolites have a net negative charge. Cations are therefore required to balance the charges in particles made of these molecules. The morphology of alumino-silicates is highly irregular. Because of the tight crystal structure, cations can reside only on the surface of these particles [100]. Electrostatic forces hold the ions to the surface [92].

The polarization of zeolite particles is accomplished via the motion of loosely bound charges that are chemically part of the particles. Materials made with zeolites are *intrinsically* electrorheological. Materials which rely on water or mobile ions in the dispersing phase are *extrinsically* electrorheological. Intrinsic ER materials have much lower current densities than do suspensions of corn starch in olive oil.[3] Higher electric fields, and higher yield stresses, can be more easily achieved. The behavior of intrinsic materials is easy to control; by heating the particles above 200°C, almost all the water is driven off. In comparison, in moist ER materials, it is more difficult to drive off *only some* water and control the moisture content of the partially dried particles.

Electrorheological materials are complex. Interactions among the dispersed particles, fluid, electric field, fluid flow, mobile ions, and electrostatic fields contribute to the changes in material properties. The development of anhydrous ER materials is promising in that strong forces can be generated with power requirements several orders of magnitude less than those of moist substrates. In order to take full advantage of these materials, their special properties must be considered when designing the devices and methods in which they are to be implemented.

[3]But they don't taste as good!

1.2 The Flow of ER Materials in Vibration Control Devices

In viscous-fluid vibration-damping devices, the flow of the fluid in the device is prescribed by the device motion. If the device is of a dash-pot configuration, the fluid shear rates in the device can become quite high (on the order of a thousand per second). If this is the case, the pre-yield material behavior is of secondary importance. An idealized ER fluid resists shear stress with an electric field dependent yield stress and a viscous stress proportional to the shear-rate. This simplifying assumption leads to models relating the device geometry and material properties to the pressure gradients in a prescribed flow.

The flow field in damping devices can be categorized as shear, flow, or a combination of shear and flow. Continuity conditions require rotational motion in any sealed device which produces a pure-shear flow field. Velocity fields caused by rectilinear motion in confined geometries necessarily have a non-zero flow component, and possibly a shear component as well.

1.3 Approaches to Control

Techniques for abating the motion of structures due to external loads (earthquake, wind, or machinery) can be grouped in four major categories: passive, active, hybrid, and semi-active vibration control.

- **Passive** vibration control is accomplished by adding energy dissipating devices or energy absorbing devices. Bracing members with viscous, visco-elastic or frictional properties are common energy dissipating devices which can be found in tall flexible structures, such as the World Trade Center [183]. Tuned mass dampers absorb vibrational energy by inducing resonance in an SDOF sub-

system which is designed to tolerate large deformations [76].

- **Active** vibration control systems utilize force generating members such as hydraulic actuators or piezo-electric elements [249]. The control forces depend on measured structural motions and in some cases measured disturbances. Through the incorporation of active vibration control methods, the dynamic characteristics of the controlled system (natural frequencies and damping properties) can be dramatically altered. Typically the addition of an active control system is analogous to adding substantial damping to the structure. (In certain cases the damping of some modes may be required to decrease, which can only be accomplished with active members.) Other control objectives, such as tracking a prescribed motion trajectory, can also be satisfied, but have limited applications in civil engineering structures. Perhaps the most important application of active control is the stabilization of inherently un-stable systems. By incorrectly designing the controller, it is possible for active control systems to actually increase the vibration levels of a structure. Furthermore, active control methods require external energy sources to power the active structural elements.

- **Hybrid** vibration control systems combine passive and active elements. Because of the enormous forces required to control vibrations in civil structural systems, it is advantageous to achieve as much of the control objective as possible with passive elements, and thereby alleviate the demand on the active elements.

- **Semi-active** control methods make use of members which can change their mechanical properties (stiffness and damping). These members are *passive* in

that they can only produce forces in response to actions across their terminals. Although semi-active control rules can be derived which increase structural vibrational energy, the passivity constraint on the actuators allows a wide range of control rules to be investigated.

The passivity constraint is effectively a discontinuity, and it precludes analytic evaluation of some semi-active controllers. Evaluation is often conducted with time-domain simulations. Simulated performance of a semi-actively dampened structure is often compared to the structures behavior with light damping. Such a comparison does not test the semi-active control rule as compared to an *optimal* level of constant damping.

The ability to regulate forces by several orders of magnitude, in a matter of milli-seconds, and with very little required input energy, is attractive for various actuation and control applications. The potential applications of battery operated control devices and actuators, is motivating the study of ER materials for many control applications [8, 10, 11, 12, 13, 14, 17, 23, 39, 42, 46, 47, 65, 66, 67, 80, 86, 101, 112, 122, 148, 171, 198, 199, 200, 201, 217, 218, 219, 246, 252, 279, 280].

1.4 Organization of the Thesis

This thesis is organized into seven chapters.

Chapter II reviews work published from 1875 to the present on the behavior and mechanisms of ER materials. Many erroneous assumptions have led to misconceptions regarding the ER effect. In reviewing the early research, this chapter, and Appendix A, highlight the sources of error in these simplified models. By including some of the complexities of the ER effect, more recent models have approximated the actual stresses observed in *some* ER fluids.

Chapter III describes the flow of ER materials in rectangular duct geometries. The Navier-Stokes equations are solved for steady flows and for the transient resulting from time-varying material properties. A useful dimensionless polynomial, derived in 1969 from the steady flow equations, is adopted in this chapter. In certain important cases, roots of this polynomial form can be found analytically. In general, a numerical solution is required. A simple, yet robust, numerical technique is presented in Appendix B, and simple closed form approximations to the numerical solutions are presented. This approximation reduces to a very good approximation to the analytical roots, when appropriate. These analyses lead to an explicit trade-off between the dynamic range of ER dampers and their response times. The use of these equations for design of ER dampers, and identification of ER material properties, is addressed in Appendix B. Lastly, device geometries are described which contradict assumptions regarding the constitutive laws.

Chapter IV describes the use of ER materials in controllable vibration actuators, engine mounts, vehicle suspensions, and clutches.

Chapter V expands a previously known two-dimensional curve-fitting technique to multiple dimensions and describes the application of this *non-parametric* modeling method to ER dampers. Device and fluid specific models for simulation and for feedback linearization can be obtained with this technique. The issue of the convergence of this curve-fit to a minimax approximation is addressed in Appendix C.

Chapter VI presents experimental results from tests on small and large-scale ER dampers. Methods for analyzing and designing these devices based on the relations described in Chapter III are described. The small scale experiments were designed to assess the strengths and weaknesses of the flow approximations. Pressure gradients in steady flow and transients resulting from time-varying material properties were

measured. The high voltage test environment and the fast slewing electric fields necessary to produce these transients required specialized electronics. These small scale tests evaluated the effect of device geometry on the dynamic range and on the response times.

Large scale experiments were conducted to assess the design equations, to gain experience in using ER devices for civil engineering structural applications, and to develop a data base for testing the accuracy of the curve-fit technique. A summary and conclusions are presented in Chapter VII.

CHAPTER II

THE EMERGENCE OF ELECTRORHEOLOGY

2.1 An Overview of the ER effect

Electrorheological (ER) materials are suspensions of specialized, micron-sized particles in non-conducting oils. When electric fields are applied to ER materials, they exhibit dramatic changes in material properties. The exact causes of this ER effect are not completely understood, but have been attributed to trivial consequences of the electric field, i.e., polarization [93, 97]. A dielectric mis-match between the particles and the fluids makes the particles polarizeable in the presence of any strong electric field (2–7 kV/mm). If the particle dielectric constant is higher than that of the fluid, the electric field is intensified in the fluid near the particle, and attenuated within the particle. Perfectly conducting particles (infinite dielectric constant) can have no internal field.

The polarization of particles probably plays an important role in the ER effect. Particles can become polarized through a variety of mechanisms:

- If the particles, or fluid, contain mobile ions, polar molecules such as water, or both, the ions will be attracted to the particle's surface. Polar molecules or mobile ions in the fluid will form an electric double layer around the particle, aligned with the electric field.

- Polar molecules or mobile ions within the particle will become desorbed to the particle's surface, and migrate to align with the field. These ionic double layers may be thin and tightly bound to the particle surface, or they may be disperse.

- Particles with immobile charges will rotate to align with the field.

- Mobile charges inherent to the particle will migrate through or along the particle to align with the field.

The *nature* of the polarization mechanism governs important properties, such as the current density and stability of the ER suspension. While the details of the polarization mechanisms have not been fully identified, understanding and controlling them is essential in designing ER materials for commercial applications. If a bi-polar double layer forms, water, salts, or other mobile charge carriers in the oil phase adhere to the particles. An applied electric field will cause the non-adhered ions to attach to the particles and the adhered ions to migrate toward the electrode of opposite charge. Two types of electrical double layers have been postulated [28]. First, a particle can be coated with a thin conducting layer such as water. Under electric fields, the charged water molecules can migrate to the cathodic side of the particle. Second, the particle can be coated with a conducting layer of ions which extends into the (non-conducting) surrounding media. Both of these double layers are probably present to a greater or lesser degree in many ER suspensions.

Aligned charges in a polarized particle create a dipole moment, $p \propto a^3 \beta E$, and aligned with the external field, E. The factor β is a measure of the polarizability of the particle and a is the particle diameter [119]. The electrostatic potential energy between two of these particles is called the *point dipole pair interaction energy*,

$u(r, \varphi)$,

$$u(r, \varphi) = -\frac{p^2}{4\pi k_f \epsilon_0 r^3}(3\cos^2\varphi - 1), \tag{2.1}$$

where ϵ_0 is the permittivity of free space, r is the inter-particle separation, and φ is the angle between the inter-particle axis and the electric field vector.[1] Differentiating the potential with respect to r, the inter-particle axial force is seen to vary with p^2/r^4 (or $a^6(\beta E)^2/r^4$). This force is anisotropic. Particles aligned along the electric field are attracted to each other. Particles arranged across the electric field are repelled [120]. The theoretical variation of the interparticle forces is illustrated in Figure 2.1 The polarization force is long-range, quadratically related to the electric field, and is

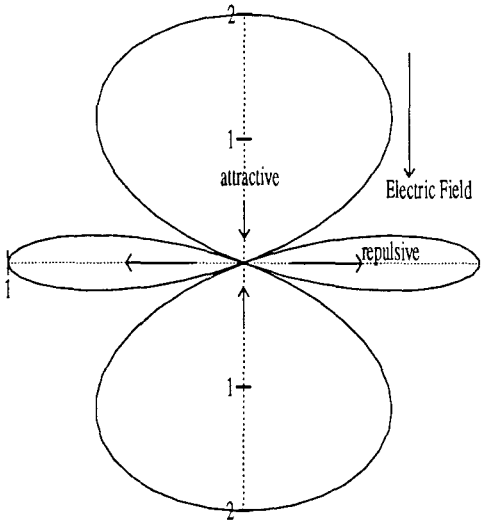

Figure 2.1: Variation of point dipole interaction force with φ.

very sensitive to the particle size.

When an electric field is applied to an ER suspension, the particles polarize and align themselves in the direction of the electric field within milli-seconds. On a longer time-scale, these fibrils drift together and bridge the electrode gap. At high electric

[1]See Appendix A for a derivation of (2.1).

fields and low levels of strain, ER materials are essentially visco-elastic plastic materials [99, 100]. The stiffness properties (shear and tensile moduli), the yield stresses, and the yield strains are strongly dependent on the electric field. Observed yield strains typically decrease with the electric field and yield stresses increase roughly quadratically with the electric field. An accompanying dramatic increase in pre-yield stiffness follows from this behavior. Also, at pre-yield strains, linear viscosity increases dramatically with the electric field.

Under steady-shear conditions, the fibrated structures remain in tension until they form a critical angle with the field, ($\varphi \approx 55°$) at which time the particles repel each other (and form a new inter-electrode fibril with other particles) [120, 156]. Shear strains close to unity ($\gamma \approx 1$) produce this critical angle. Under steady-flow, the continuous breaking and re-forming of fibrated particle chains, and the presence of a solid slip surface, resembles solid-yielding mechanisms. This mechanism manifests itself on a macroscopic level as a yield stress, τ_y, and is commonly observed in ER materials. Theoretically, the yield stress scales with $\phi(\beta E)^2$, where ϕ is the volume fraction of particles in the suspension [119]. At high fields, the dipoles become saturated and a further increase of the electric field produces only a linear increase in τ_y with E [251]. The exponent of power laws relating yield stresses to electric fields ranges from 1.2 to 2.5 in typical ER suspensions.

The observation of a yield stress motivated the use of the *Bingham* constitutive model for the fluid, in which an applied shear stress, τ, is resisted by a yielding component, τ_y, and a viscous component, $\eta\dot{\gamma}$

$$\tau = \tau_y \mathrm{sgn}\dot{\gamma} + \eta\dot{\gamma}. \tag{2.2}$$

Assumptions implicit in the Bingham approximation are:

- The material has no deformation below the yield stress.

- The flow of the material is steady and fully developed.

The Bingham model can not account for all the interactions and mechanisms in actual ER materials. The scaling of ER activity with component material properties, ϕ and β, electric field, E, and shear rate, $\dot{\gamma}$, grossly under-estimates the yield stress observed in experiments. Nevertheless, post-yielding ER behavior qualitatively approaches a Bingham model [97].

Many concentrated colloidal suspensions, such as crude oil, paints, fiber dispersions, food products, polymer systems, concrete, and slurries, exhibit Bingham-like behavior [192]. As in ER materials, the yield stress is related to structure formation in the suspension. These structures may assume different forms, such as entangled macro-molecules, fibrated chains, flocculated aggregates, or card-house structures [192]. Because the yield stress in all of these Bingham fluids is related to electrostatic interactions between the particulates, they all exhibit an ER effect to a greater or lesser degree. ER materials are a class of these Bingham fluids in which the yield stress is significant, and is easily controllable through the interaction of the suspended phase with an electric field.

Contemporary investigations have led to models of the micro-mechanical aspects or bulk properties of existing ER materials [1, 31, 32, 33, 54, 116, 188, 239]. Studies relating to particle composition and morphology, mobile ions, electric field intensification, dielectric breakdown, conduction mechanisms, and consistent sample preparation are much rarer, but address the current research needs relating to these materials [92, 94, 97, 235]. When these items are better understood, ER materials will be very attractive for a variety of commercial and industrial applications [8, 9, 10, 11,

12, 13, 14, 17, 20, 38, 39, 47, 57, 65, 67, 82, 83, 86, 165, 197, 205, 231, 236, 237, 238].

2.2 Early Observations

The remarkable pre-yield, field-dependent behavior of ER materials was not noted until recently [99, 100]. Early work focused on the post-yielding behavior in steady flows.

The effect of electric fields on the optical and structural properties of dielectric suspensions was reported 1875 and led to experiments to study the effect of electric field on viscosity [85]. Wilmer Duff measured the time required for a mercury droplet to fall through a vertical glass tube filled with paraffin or castor oil with and without an electric field applied across the tube[2] [85]. He noted an increase of viscosity of castor oil by 0.5% in the presence of a 2.7 kV/mm electric field. Paraffin oil exhibited the opposite effects. After repeating tests with a variety of beads in liu of the mercury droplets, he rejected temperature, horizontal deflection (electrophoresis), electrical retardation of the droplets due to field interaction, droplet deformation, and rotation of the droplets in the electric field as causes for the noted viscosity changes. But he offered no alternative explanation. Although micro-structure in the oil had been noted by Kerr in 1875, Duff did not propose the formation of inter electrode fibrils as a possible viscosity-increasing mechanism [85].

Half a century passed before the increased resistance to flow in an electric field was associated with fibration of particles. In the 1940's Willis M. Winslow, while searching for relays with better mechanical properties, experimented with the known high electrical attraction between a charged metal plate and a smooth marble surface [175]. When marble particles became entrained in the lubricating oil between the

[2]The rate of descent is theoretically independent of the droplet size.

marble and the electrode, he found that electrical pulses to the electrode were translated to mechanical forces in the "dirty oil". He improved the effect by replacing the marble with another electrode and undertook a series of experiments on suspensions of hydrophilic particles in dielectric suspensions [303]. These studies led to patented designs for valves, clutches, brakes, loudspeakers, and the suspensions required for their operation. He noted that electric fields across the suspensions induced fibration of the particles parallel to the field, and that the yield stress was proportional to the dielectric constant of the material and the electric field squared [303]. Tests on ferro-magnetic particles in suspension exhibited similar effects in a magnetic field, but residual magnetization of the particles slowed their response times significantly.

The electric field induced torque and rotation of polarized prolate spheriods in Couette flow was solved analytically in 1958 [74]. In 1967, experimental studies by Klass and Martinek on the electroviscous effect of silica particles in mineral oil, led to a theory of electroviscosity based on interfacial polarization between particles [153, 154]. Although field dependent yield stresses were apparent in the experimental results, the effect of the electric field was presented in terms of apparent viscosity, η_{app}, which was defined as the ratio of the shear stress, τ, to the shear rate, $\dot{\gamma}$. The apparent viscosity was found to increase quadratically with the electric field, to increase with the volume fraction of silica particles, and to decrease with shear rate [153]. Electric field induced fibration and increased viscosity were attributed to interactions of polarized charged double layers. In an electric field, the double layers deform. Migration of charged ions along the double layer, toward the electrode of polarity opposite to that of the ions, polarizes the particles. Polarized particles align themselves in the direction of the electric field, and form fibrils connecting the electrodes. When the double-layers over-lap, interparticle forces increase significantly

[153]. Because ions move more freely at elevated temperatures, the electroviscous effect increases with temperature. The fibrils conduct current through the desorption of ions from the particles into the double layer, and the motion of ions between particles. The electric current was found to drop significantly under shear but finite currents and mobile ions were thought necessary to produce any electroviscous effect whatsoever [154].

Water adsorbed into the strongly hydrophilic silica particles of Klass and Martinek was the source of the double layer and mobile ions. Early attempts to find sources or the electroviscous effect identified three likely mechanisms [182]:

1. field induced orientation of particles,

2. formation of a fibrous micro-structure, and

3. interaction of disperse electrical double layers.

Experiments aimed at quantifying the effect of water concentration on the electroviscous effect showed that a threshold moisture content of 2% was required for any electroviscous effect. The electroviscous effect was found to be maximum at a moisture content of 6% and to diminish with increasing moisture. At a moisture content of 20%, no effect was observed [182].

These results were qualitatively confirmed in experiments by Uejima, in which both the weight fraction of absorbed water on the particles and the weight fraction of crystalline cellulose particles were tabulated [278]. The electroviscous effect reached a threshold at particle weight fractions of 6% to 7% and exhibited peak performance with a water weight fraction of 10%. In this 1972 study, Uejima noted that a Bingham model could describe the behavior of these materials, and that the term *electrorheological* was more descriptive than electroviscous, since the resistance

to flow was more complicated than a viscous model could easily describe. According to a Bingham constitutive relation, the stress in electrorheological (ER) materials has a field-dependent yield stress, τ_y, and a Newtonian viscous stress, $\eta\dot{\gamma}$.

$$\tau = \tau_y(\theta, E)\mathrm{sgn}\dot{\gamma} + \eta(\theta, E)\dot{\gamma}, \tag{2.3}$$

where θ and E indicate a temperature and electric field and dependence. The yield stress was found to be roughly proportional to the electric field squared, and the viscosity was found to decrease with increasing fields [40]. Variations from the quadratic dependence of shear strength on electric field are partially due to a threshold electric field effect (required to produce any ER activity), and short-range electrostatic interparticle repulsive forces [104]. Spherical particles have lower threshold fields than rod-shaped or disk-shaped particles [269]. And the threshold field decreases with the concentration of particles [304]. When electric fields are applied to quiescent ER materials, yield stresses are stronger than they would be in flowing ER materials [278]. Yield stresses become stronger with time in quiescent materials. In other words, ER materials exhibit negative *thixotropy*[3]. Because the ER effect is fully reversible, ER materials are thixotropic upon removal of the field.

Sugimoto, in developing resin-based ER particles, noted that using water as the ER activator had undesirable properties [266]. Specifically, drier ER materials conducted lower electrical currents.

In an early survey, Deinega noted some properties characteristic of ER behavior [73].

- Lower currents were drawn at high rates of deformation.
- Electrical fields affect the migration of different particles differently. Anaphore-

[3]Thixotropy is the property of certain gels of becoming liquid when shaken or stirred.

sis, cataphoresis, double electrophoresis, interelectrode oscillations, interelectrode contraction, rotation, and fibration of particles were among the possible particle migrations presented.

- The yield stress, τ_y varied with E^2 at low field strengths, but became saturated at high fields.

- The ER effect was most pronounced at 40°C-50°C, but diminished as the temperature reaches the boiling point of water.

- The relatively high yield stresses of ER materials which use water as an activator were attributed to the formation of hydrogen bonds.

Modeling the structure formation in a quiescent suspension of rigid spherical dipoles, Mors observed the formation of a dense structure and a spatial correlation of the dipole orientation [202].

In one series of experiments on water-activated materials, Sprecher used 125 micron diameter, glass spheres in silicone oil [251], and observed fibration under fields of 2.5 kV/mm. Shear stresses measured in Poiseuille flow experiments followed a Bingham-type constitutive model. A static yield stress, in excess of the dynamic yield stress, was observed at higher electric fields and higher volume fractions of silica particles. The yield stress varied with the square of the electric field and with the silica volume fraction to the (2/3) power. Microscopic observation of the fibrils during shearing revealed that the fibers tended to break and reform close to their centers.

2.3 Modern ER Materials

As had been noted previously, the water adsorbed into the hydrophilic particles (silica, cellulose, or corn starch) limited their performance. The current drawn by these materials was attributed to surface conduction along the electric double-layer [153, 154]. Electric fields are intensified between closely spaced particles. Localized high electric fields in the continuous phase result in finite conductivities, due to the non-ohmic nature of the dispersant. Electricity is conducted primarily through non-ohmic effects in the continuous phase and disperse ionic double layers, rather than through bulk conductance of the particles [104]. Mobile ions in the continuous phase are a likely source of the non-ohmic effects, which are less pronounced in dry ER fluids.

Kilowatts of power are required to achieve kN levels of force in hydrous ER materials [29]. Resistive (iR) heating increases the conductivity and current draw, which further increases the temperature. With continued heating, water is driven off through evaporation or electrolysis, and the ER effect disappears. It is therefore difficult to control the level of the ER effect in hydrous ER materials [43]. Furthermore, when hydrous particles settle, hydrate bonds irreversibly flocculate the particles into sedimentary layers, and it is difficult to return the particles into a useful suspension.

The 1988 patent of Frank E. Filisko [91, 135] and the 1986 patent of Henry Block [27] for anhydrous ER materials heralded the beginning of increased research into the ER effect and its potential applications [5, 10, 11, 13, 86, 95, 135, 230, 231, 232]. Block's ER materials use semi-conducting particles and Filisko's materials make use of zeolite and amorphous alumino-silicates particles. Ions, locally mobile but chemically associated with the particles, allow these particles to polarize [93]. Mobile cations,

required to balance the zeolite particle's charge, are trapped Coulombically by the particle's convoluted morphology and tight molecular structure, are intrinsic to the particle, and cannot carry charge from particle to particle. Comparisons of zeolite-based ER performance at various water concentrations [92] show that reducing the concentration below 0.5% by weight leads to:

- ER materials with conductivities on the order of those of dry paraffin oil, ($10^{-4}\mu$Amm/cm^2),
- dielectric strengths comparable to mineral oil (10 kV/mm), and
- yield stresses comparable to those of moist materials.

Recently, yield stresses in excess of 50 kPa with fields of 2 kV/mm and currents of 20μAmm/cm^2 have been reported in ER materials with zeolite particles protonated with transitional metals [304].

In 1988 Block reviewed the wide range of ER materials available at that time [28]. All the materials required an activating additive to produce any ER effect. In most of these materials, the additive was water, and almost all of the additives were ionic in nature. In the same review, Block described the effect of different electrical, mechanical, and thermal operating environments on ER activity.

- **Electric fields** induce a yield stress in ER materials. A threshold electric field may be required for any ER activity. Careful experiments have identified the presence of a threshold field of 0.1–0.3 kV/mm [298]. The threshold field was found to increase to 0.8 kV/mm with increasing fluid shear rates [296]. Dielectric breakdown limited the electric field to 3–9 kV/mm, depending on the composition.

- **High electric field frequencies** result in reduced ER activity. Behavior at electric field frequencies below 100 Hz is qualitatively similar to the behavior at DC fields.

- **Temperature** ranges between 20°C and 50°C are required for hydrous ER materials. Anhydrous zeolite-particle and silicone-oil materials are active between −60°C and 350°C [93].

- **Shear flow** rotates particles and their polarization vectors. This flow induced rotation is resisted by an electric-field induced torque on the rotated polarization vector, which enhances the viscosity under electric fields.

Block also reviewed issues of composition, such as the chemistry of particles, and dispersants, the volume fraction of particles, and the role of additives. He identified design issues for ER materials:

- **Particles** can become polarized by adsorbed electrolytes migrating through the particle, along the surface of the particle, through an electric double layer, or by particle rotation. Interfacial polarization of the double layer is probably at the source of the ER effect in hydrous materials. Porosity, mobile ion content, and abrasiveness are important factors in designing particles for engineering applications. ER systems in which the particles polarize easily are more active. Systems which make use of ionic activators are better characterized by the properties of the activators rather than the bulk dielectric properties of the particles [94]. In systems in which activators are not present, the dielectric constant of the particles should be high. Particles of irregular shape behave hydro-dynamically as spheres [29].

- **Dispersants** should have high dielectric strengths and low conductivities. They should be non toxic, stable, and have low dielectric constants.

- **Additives** such as water, salts, or other mobile ionic conductors, provide ion sources for interfacial polarization. An excess of ionic additives, however, results in excessive currents. For clay particles, water content between 5% and 10% by weight is optimal while starch particles work best with water content at 35% by weight. Water and salts introduce issues of corrosion as well.

- **Volume fractions** of 0.1 to 0.4 are preferred. The ER effect is too small at volume fractions below 0.1, and the effect saturates at volume fractions above 0.4. At very high volume fractions, the materials become conductive and, therefore, impractical.

Draw-backs of ER materials with ionic activators (iR heating, high currents, limited temperature range, electrolysis, corrosion, stability, and reproducibility) disappear for the most part when anhydrous intrinsic ER materials are used [94]. While intrinsic systems may share many ER mechanisms with hydrous systems, focusing exclusively on hydrous systems cannot lead to commercial applications.

The rate of polarization is tantamount to ER material response times. The polarization mechanism and the dielectric properties of the particles influence the polarization rate, as well as magnitude of the dipole moment (yield stress) [29]. If the polarization rate is too slow, however, flow induced particle orientations will weaken the ER effect. The relationship between polarization rates and yield stress may be at the source of a static yield stress in excess of the dynamic yield stress, different stress-strain curves for loading and un-loading, and high yield stresses at electric field frequencies above 100 Hz. Large static yield stresses have also been attributed

to particle jamming or dilatant behavior [47].

2.4 Visco-elastic Behavior

Under low-level cyclic strains, ER materials deform, but do not yield. The controllable storage and loss moduli of ER materials can be exploited as a variable shear-transfer link in beams [101, 184].

In a pre-yield region, the mechanical behavior can be described by a Zener element (a Voigt element in series with a spring). The major ER effects can be qualitatively modeled by a Zener element in series with a solid-friction element and a viscous element [99]. This mechanical model is illustrated in Figure 2.2. All the elements are influenced, to a greater or lesser extent, by the electric field.

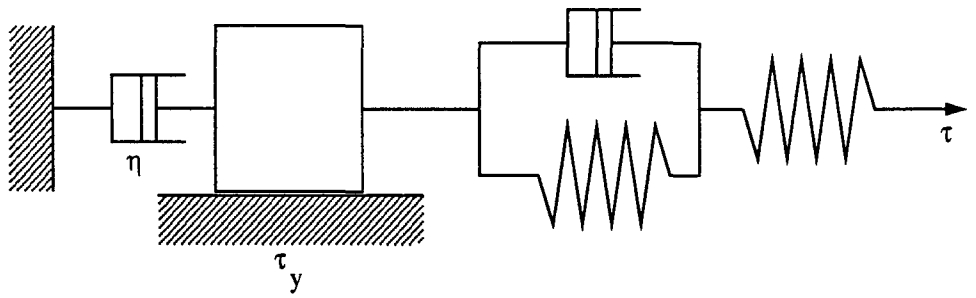

Figure 2.2: A mechanical analogue for ER materials.

The response of ER materials with weak to moderate particle concentrations can be modeled with a strain frequency-dependent complex modulus [191]. ER elasticity is primarily related to an affine increase of potential energy of fibrils spanning the electrodes. Experiments show this modulus to be frequency independent. The loss modulus, however, decreases with the frequency of the applied strain. A source for this frequency-dependence was identified by considering the response of broken fibers to small strain oscillations [191]. A normal mode model for the motions of the fibers, led to a loss modulus which increased at low frequencies, reached a plateau,

and decreased with higher frequencies. Increased particle concentration enlarged the plateau region. Increasing strain and electric field both increase the potential energy of fibrils. So fibrils can be broken by simply increasing the electric field [191].

Subsequent video imaging of shearing ER suspensions showed that at larger strains, electric fields, and volume fractions, thin fibrils tended to break at their centers and re-attach to thicker columns. The columns tended to break at the electrode. At high shear rates, most of the columns dragged along the electrode surface [141].

Increasing the electrode surface adhesion properties seems like a promising approach toward increasing ER yield stresses [192, 206]. Rheometers with rough surfaces are essential in overcoming wall-slip effects when testing foams [151]. Tests on cement grouts in a Couette rheometer with rough walls yielded shear stresses 50% larger than stresses in a smooth-walled rheometer, at low shear rates [55]. In fact, the fluid shear stresses may be governed by the adhesion (and the local concentration) of the particles at the walls [55]. As in the deformation of granular solids, concentrated suspensions flow by developing slip surfaces. If rough walls prevent slip surfaces near the surface, then the slip will occur within the material itself. By enhancing the adhesion of ER particles to the walls, the slip plane is forced into a region of higher inter-particle interaction. Mildly di-electrophoretic ER suspensions may also have enhanced wall adhesion properties.

Gamota conducted extensive tests at high frequency Couette flow oscillations (300–400 Hz) and found that the storage modulus increased with $E^{2.1}$, and that the loss modulus increased with $E^{1.1}$ [100]. The loss modulus increased slightly over this frequency range. A fibril breaking mechanism was considered an unlikely source for the dependence of the loss modulus on frequency and electric field because the

strains at these frequencies were so small. Two other dissipative mechanisms, were proposed:

1. Increased resistance to flow of the dispersant through the fibrated structure could explain the increase of the loss modulus with field.

2. Motion of mobile ions in the flow-driven oscillating particles can dissipate energy, and could explain the shear rate dependence.

A Zener element (a parallel dash-pot and spring in series with a spring) can model a frequency dependent loss modulus. The loss modulus first increases with frequency then decreases, but no plateau region is predicted by the Zener model [100]. Because this plateau region stems from broken fibrils resisting flow, it was not observed in these high frequency, small strain, experiments.

Considering the statistical distribution of disperse rigid-sphere dipole pairs subjected to Brownian effects in a dielectric fluid, Adriani and Gast calculated the bulk stress due to small strain, high frequency, sinusoidal shear flow [1]. For proper scaling of the Brownian stress, the particles were assumed to be small (less than 0.5 microns in diameter) and inertialess. Particles were distributed elliptically, with the major axis aligned with the electric field vector [104]. The linear elastic and loss moduli calculated from the bulk stress underestimated experimental values. Multi-pole electrostatic interactions and many-sphere hydrodynamic effects (in fluids with volume fractions on the order of 0.4) were not included in this analysis, which led to the low modulus and viscosity estimates. Adriani and Gast's study did, however, point toward dynamic simulations of multi-particle systems. These simulations have clarified some aspects of ER phenomena.

2.5 Post-Yielding Behavior

In contrast to the theoretical approach of Adriani and Gast, Marshall, *et al.* described an empirical approach toward parameterizing ER behavior in a single dimensionless number [187]. A series of steady-flow Couette rheometer measurements, in which the volume fraction, ϕ, the particulate and dispersant (fluid) dielectric constants, k_p and k_f, the continuous phase viscosity, η_c, the shear rate, $\dot{\gamma}$, and the applied electric field, E, were measured, led to the observations that

- under an electric field, ER materials are shear-thinning,
- the effect of the electric field is diminished at high $\dot{\gamma}$, and
- the behavior at high $\dot{\gamma}$ depends primarily on η_c.

These results imply that yielding mechanisms govern the behavior at high electric fields and low shear rates, while the behavior at high shear rates is primarily viscous in nature. The relative importance of Brownian, van der Waals, electro-static, polarization, and viscous forces were assessed as well [187].

- In the absence of electric field, van der Waals forces exceed Brownian forces by a factor of 2.
- Short range repulsive electro-static forces (due to the overlapping of the diffuse double layer) are overcome by attractive van der Waals forces at finite particle separations. This leads to weakly flocculated particles in quiescent fluids.
- The characteristic scale of the viscous forces on the (spherical) particles is $6\pi\eta_c a^2\dot{\gamma}$, where a is a characteristic particle length (microns). Viscous forces overcome the flocculating van der Waals forces at low shear rates (0.02/sec), and can be 10^4 times as great as Brownian forces at shear rates of 200/sec.

- In the presence of an electric field, interparticle attractive electrostatic forces are 10^4 times as great as the van der Waals forces, but are on the order of the viscous forces for current ER materials.

Hence, the behavior of ER materials is strongly dependent on the ratio of viscous forces to polarization forces. This is the basis for the dimensionless *Mason number*. The Mason number, Mn, as defined by Marshall, *et al.* is

$$Mn = \frac{\eta_c \dot{\gamma}}{2\epsilon_0 k_f (\beta E)^2} \tag{2.4}$$

where the parameter β is the *particle dipole coefficient*, which describes the polarizability of a single spherical particle in a dielectric continuum with an electric field,

$$\beta = \frac{k_p - k_f}{k_p + 2k_f}, \tag{2.5}$$

and $-(1/2) < \beta < 1$. Many active ER materials have $(k_p/k_f) \gg 1$ and $\beta \approx 1$ [104].

The dielectric constant of the particulates cannot be measured directly but can be estimated using the rule of mixtures [61] from measured values of the continuous phase dielectric constant, k_f, the dielectric constant of the suspension, k_{er}, and the volume fraction, ϕ,

$$k_p = (k_f(1-\phi) - k_{er})/\phi. \tag{2.6}$$

Another method used for calculating k_p makes use of Maxwell's equation for the effective dielectric constant of suspensions [158],

$$k_{er} = k_f \left(\frac{1 + 2\beta\phi}{1 - \beta\phi} \right). \tag{2.7}$$

Substituting (2.5) into (2.7) and solving for k_p leads to

$$k_p = k_f \frac{k_f(2\phi - 2) + k_{er}(\phi + 2)}{k_f(2\phi + 1) + k_{er}(\phi - 1)}. \tag{2.8}$$

The Mason number (and particle dipole coefficient) cannot, however, parameterize all ER materials. Values of k_p derived from (2.6) or (2.8) will not indicate the polarizability of the particles if the ER fluid relies on ionic activators. Indeed, there is evidence that surface effects dominate the polarization of even intrinsic ER materials [96]. The dipole coefficient for extrinsic ER materials depends more strongly on ionic activators than the bulk dielectric properties of the particles [93]. Extrinsically active particles, such as silica, can be much more active than β would indicate. In concentrated suspensions ($\phi > 0.3$), the yield stress can scale with $(\beta E)^{2.4}$ [211], and can be increased further through gentle agitation of the fluid, and densification of the structure [257]. With the decrease in inter-particle spacing, there is a concomitant increase in conductivity.

Marshall found that steady shear of an ER material of known composition could be parameterized by Mn; and found that effects of temperature on ER behavior can be adequately modeled by considering only the variation of η_c with temperature, θ [187].[4] The Bingham constitutive relation can be written in terms of Mn:

$$\frac{\tau}{\dot{\gamma}\eta} = \frac{Mn^*}{Mn} + 1, \tag{2.9}$$

where

$$Mn^* = \frac{\eta_c}{\eta} \frac{\tau_y}{2k_f\epsilon_0(\beta E)^2} \tag{2.10}$$

is the *critical Mason number*. At $Mn > Mn^*$, the resistance to steady flow of the ER material is almost entirely viscous. The critical Mason number was empirically demonstrated to vary linearly with the volume fraction, ϕ, in some materials [187].

$$Mn^* = K\phi \tag{2.11}$$

[4]Other researchers, however, have noted a strong dependence of β (and τ_y) on θ through variations of k_p and k_f with θ [61].

Combining (2.9) and (2.11), the behavior of a wide range of ER materials were parameterized by the single dimensionless group, Mn/ϕ [187].

The Bingham model requires instantaneous disintegration and reformation of structure during steady flow. In fact, in a steady shear flow, viscous forces continuously work to disrupt the structure while electrostatic forces act to re-form the structure [243]. Stable equilibrium structures are seldom observed. Rather, fluctuations in observed shear stresses are indicative of a continuous destruction and re-creation of a fibrated structure [36, 45, 214]. Because the micro-structure of ER materials degrades over a range of Mason numbers, the Bingham model under-estimates ER behavior in the vicinity of $Mn = Mn^*$ [187]. Fringing of the electric field magnifies inter-particle polarization interactions, and is empirically accounted for, through the constant K.

While (2.3) can model ER behavior under steady flow conditions, a generalized Casson model [206] has been proposed to model threshold effects [244, 241],

$$(\tau \mathrm{sgn}\tau)^{1/n} = \tau_y^{1/n} + (\eta\dot{\gamma}\mathrm{sgn}\dot{\gamma})^{1/m}, \tag{2.12}$$

where the exponent n and $\eta^{1/m}$ are of the form $c_1 + c_2 E^2$. Studies using the Bingham model are, nevertheless, most common to date.

2.5.1 Observation of Post-Yield Behavior

The transition region, between pre-yield and post-yield states is the most difficult region to characterize. Many investigators have reported a hysteretic behavior in shear rate, associated with shear-thinning behavior during loading and Bingham plastic behavior during unloading [257]. See Figure 3.11. This behavior indicates the presence of a static yield stress in excess of the dynamic yield stress.

In fitting power laws between temperature and yield stress, temperature and

current, and yield stress and current, Conrad, *et al.* report consistent correlation between the yield stress and current (for $2°C < \theta < 120°C$) [60, 62]. They attribute both yield stress and conductivity to cation diffusion, which implies that finite currents are required for ER effects.

Under continuous shear, complete failure under continuous flow is not observed; fibrils are continuously broken and recaptured. Electrophoresis was observed in that the fibrils were coarser near one of the electrodes and remained attached to that electrode during shear [156]. This feature is specific to their specific material, and not a property of ER materials in general. Considering only electrostatic interactions of point dipole particle-pairs, a field-independent yield strain, γ_y, of 0.36 was predicted, which slightly underestimated their experimentally observed yield strains of 0.38 to 0.59 in concentrated suspensions. The authors concluded from shear stress measurements that the Bingham equation is accurate to at least second order in capturing the limiting mechanisms of ER fluids: electrostatic attraction and viscous resistance. Shear stresses were only slightly underestimated in the transition region (near $Mn = Mn^*$). Although the fibrated structure does not completely disintegrate upon shear, the electrophoretic residual structures do not influence the shear stress significantly [156].

Gow conducted Couette shear measurements of polyaniline particles in silicon oil. These measurements correlated well with the Mason number [113]. He then proposed an expression more sophisticated than (2.11), relating the volume fraction and the critical Mason number,

$$Mn^* = K\phi^n(k_p/k_f)^B, \tag{2.13}$$

where the empirical exponent $n = 1.3$; particle packing effects are incorporated in the empirical constant K; and the empirical exponent $B = 0.369$ [113].

Gamota noted that the behavior of ER materials in cyclic Couette shear, at strain rates between 10/sec and 50/sec, can be qualitatively described by the sum of Coulomb friction and viscous mechanisms [99]. The dominant mechanism changes from viscous to Coulomb as the field increases. This is equivalent to a Bingham model.

Not all investigators support the Bingham model. Halsey, *et al.* modeled a droplet of polarized particles in a shearing ER suspension as a rotated rigid ellipsoid [118]. Balancing the hydrodynamic and electrostatic torques gave a field and flow dependent rotation to the particle. Rotations increase with droplet size [119]. For small rotations, minimizing the polarization energy of the droplet led to characteristic droplet dimensions. The major axis, c, and minor axis, b, were found to be related by $b \propto c^{2/3}$, which led to a shear rate-dependent viscosity ($\eta_{app} \propto \phi\eta_c Mn^{-2/3}$).[5] For small Mn, the droplets spanned the electrodes, and Halsey's experimental data was best approximated with an exponent of –0.9. For $Mn \approx 1$, the droplets approach the particle size, and an exponent of –0.68 fit the data [119]. The authors observed no yielding behavior in their experiments, which they attribute to lack of adhesion of the particles to the electrode [118]. If particles do not adhere to an electrode, wall stresses can not be directly transferred to the fibrated structure. Another possible explanation is that the volume fraction was below a threshold level required for fibration.

2.5.2 Micro-mechanical Simulations

An early micro-mechanical model of ER behavior idealized the fiber of particles as a one-dimensional strand of prismatic segments with sequentially low and high dielectric constant, k_f and k_p, where the subscripts f and p refer to continuous (fluid)

[5] Recall that the Bingham model predicts $\eta_{app} \propto Mn^{-1}$.

phase and particulate phase [21]. If the strand has several particles, the field between the particles is magnified. The maximum field magnification factor was found to be $(2/(3\phi))$, assuming arbitrarily small particle spacing, where ϕ is the particle volume fraction [21].[6] Forming the potential energy of a particle and differentiating with respect to a coordinate normal to the strand axis, the force required to displace a particle (in the coordinate direction) was obtained. The pressure gradient required to flow an ER suspension was compared to experimental results. Only by adjusting edge effect factors to the experimental data, in a least squares fashion, could the theory match the major features of the experimental data [21].

Simulating a monolayer of ER fluid particles between shearing electrodes, Klingenberg *et al.* used a point-dipole approximation for the polarization forces between particle pairs [157]. Simulated stresses were an order of magnitude smaller than the yield stresses observed experimentally. In an attempt to include the dipole strengthening effects of multiple-particle interactions, and high order dipole moments, they adopted a perturbation approach [158]. Multiplicative correction factors to the yield stress were calculated using an exact formula for sphere-dipole pair interactions, and a previously-calculated particle distribution calculated using point-dipole pair interactions. This approach increased yield stresses somewhat, and the authors concluded that short-range interactions were important in describing ER behavior [158]. However, long-range multiple particle interactions were never calculated.

Modeling an ER fluid under shear as a periodically repeated monolayer of particles, Bonnecaze and Brady succeeded in predicting ER stresses and matched the scaling with Mn reported by Marshall [31, 187]. The evolution of the fibrated structure was continuously updated in this dynamic simulation. Hydrodynamic resistance

[6] Other researchers have found field magnification factors of 10 or greater [61] which will increase yield strengths one hundredfold.

of the (inertialess, rigid) spherical particles to flow was modeled as Stokes flow. Inter-particle polarization forces were initially simulated as point dipole-pair interactions only. Brownian thermal forces were also modeled. The spatially distorted electric field was recomputed at each time step by solving Laplace's equation. Results compared favorably with the experimental results report by Marshall [31, 187]. Like the Bingham model, the simulation results slightly under-estimate the experimentally observed stresses near Mn^*. This implied the existence of an unmodeled attractive colloidal interaction [187].

Expanding the inter-particle forces to include near-field repulsion, inter-particle friction, and many-particle electro-static interactions, Bonnecaze and Brady closely examined the kinetics of micro-structure formation [33]. Multi-particle electrostatic interactions were incorporated by calculating the capacitance between all the particle locations. The resulting capacitance matrix depended on the instantaneous particle orientation and was updated at each time step. Assumptions regarding the point dipole were retained. Aggregation of closely spaced particles in a quiescent fluid was observed. The clusters percolated to bridge the electrodes. Under shear, ($Mn = 2 \times 10^{-4}$) the structure was seen to deform finitely, snap, rapidly translate, and re-attach to the closest particle cluster. The time scale for structure re-formation was much shorter than the inverse shear rate [33]. Klingenberg and Zukoski observed this behavior in micro structure visualization experiments as well [156]. The yielding shear strains, γ_y, resulting from this simulation are close to unity (as predicted by the point dipole-dipole interaction energy (2.1)) and are about twice as large as those observed by Klingenberg [156].[7] This model implies an accumulation of elastic energy during structure elongation, which is viscously dissipated when the structure

[7]Premature yielding in Klingenberg's experiments could be related to inadequate adhesion at the electrodes.

snaps, translates, and reforms with a new configuration.

Even in the absence of an electric field, particles in concentrated suspensions can jam together and release [55]. This stick-slip behavior of the particle structure leads to fluctuations in shear stresses [137, 265] and in some cases, the particle structure can remain long after the electric field is removed [214].

Bonnecaze and Brady's simulation quantitatively followed the yielding behavior observed in experiments and the results correlated well with the Mason number [187]. Yield stresses were computed by numerically differentiating the potential energy in the suspension. The realistically large yield stresses resulting from this model are due to accurate modeling of many-particle effects and near-field interactions [33].[8] Perhaps the most useful result of these simulations is the validation of the Bingham model for ER materials in steady flow.

Next, Bonnecaze and Brady applied their simulation model to the optimization of ER component properties [32]. The maximum stresses saturated at a volume fraction, ϕ, of 0.4. Stresses increased monotonically with dielectric ratios, k_p/k_f.[9] Assuming that the fibril snapping frequency rate is proportional to the shear rate, $\dot{\gamma}$, balancing energy input with viscous (Stokes flow) dissipation, averaging over arbitrarily large periods, and taking the limit of vanishing Mn, Bonnecaze and Brady derived the Bingham constitutive relation (2.3) from first principles. (A similar derivation is due to Mokeev, *et al.* [194].) The Bingham yield stress, τ_y is equal to the chain potential energy, $\mathcal{U}$, divided by the strain when the chains break, γ_y, and reaches a maximum when $\phi = 0.4$. Strain energy is also relieved if fibrils break at the electrode [211].

Noting that at small strains, ER materials experimentally exhibit linear visco-

[8]Near-field repulsion becomes large at small Mn.

[9]Limiting factors, such as dielectric breakdown of the fluid, precludes the use of perfectly conducting particles ($k_p = \infty$).

elastic behavior, the authors postulated that the chain energy, $\mathcal{U}$, increases quadratically with low shear strains, γ, but tapers off to a constant value during yielding. Defining a static yield stress as the maximum of $\frac{d\mathcal{U}}{d\gamma}$, they concluded that a static yield stress exists which is necessarily larger than the Bingham yield stress [32],

$$\tau_y = \frac{\mathcal{U}(\gamma_y)}{\gamma_y} < \max_{0 \le \gamma \le \gamma_y} \frac{d\mathcal{U}}{d\gamma}. \tag{2.14}$$

This relationship is illustrated in Figure 2.3.

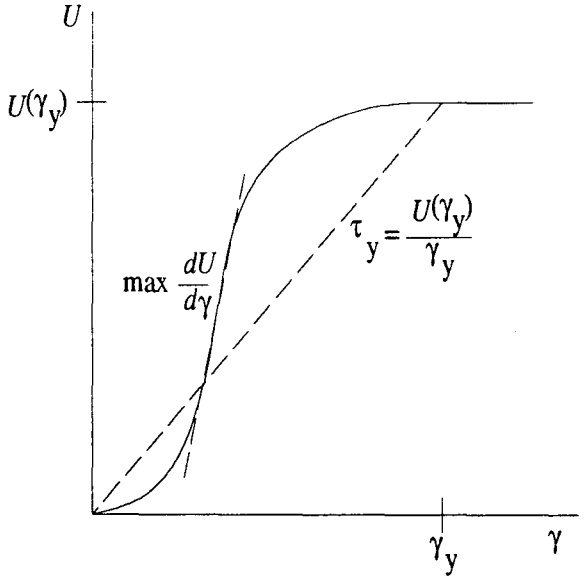

Figure 2.3: Variation of elastic strain energy, U, with shear strain γ for visco-elastic - plastic ER behavior.

Chen demonstrated the importance of multi-particle interactions by analytically solving Laplace's equation for E. Inter-particle forces in a single infinite chain of mono-disperse spherical particles was then calculated [54]. The local electric field between the particles was found to increase by an order of magnitude for small particle spacing and $k_p/k_f = 10$. The field intensified primarily in the direction of the un-perturbed electric field and reached a maximum at a value of 20 times the un-perturbed field, for $k_p/k_f = 200$. But little additional field intensification was

observed above $k_p/k_f = 50$. Yield stresses based on this field intensification were close to those observed experimentally [63]. These effects are particularly important in concentrated ER suspensions in which interparticle spacing is small. When the fibrated structure was coarser, the field concentration effects became more important, and were therefore structure-dependent [63]. This structure dependence on ER activity implies a shear-rate dependence as well. Field intensification was seen to decrease with $\dot{\gamma}$ for $\dot{\gamma} < 10$ and increase again for $\dot{\gamma} > 10$ [63]. The increase in field intensification at higher shear rates implies a layered densification of particles which may be caused by, for example, electrophoresis or interelectrode contraction. An interesting result of this analysis is that a dielectric constant ratio of $k_p/k_f \approx 13.5$ is optimum in the sense that τ_y/E^2 is maximized. Without field intensification considerations, $k_f\beta^2$ is maximized for $k_p/k_f \approx 5$. An increase in electric field by a factor of 10 or 20 is usually enough to cause dielectric break-down of the continuous phase. Dielectric breakdown lowers the shear stresses, is responsible for non-Ohmic electrical behavior, and causes other problems.

In another investigation, Laplace's equation was solved using finite-difference techniques [210]. An assumed three-dimensional, periodically repeating, trigonal lattice configuration with cube-shaped particles simplified calculation of the field. Calculated yield stresses exceeded those of a point-dipole model, but underestimated experimental values somewhat. Maximum ER activity was noted for $\phi \approx 0.4$.

Davis applied the finite element method to a simple periodic tetragonal lattice under shear [69]. Multi-particle interactions, high order multi-pole moments, and electric field concentration were incorporated and the shear modulus was calculated for a variety of dielectric constant ratios, k_p/k_f. Yielding shear strains, γ_y, of 0.5 were noted. The shear modulus increased linearly with k_p/k_f for $(k_p/k_f) > 8$. Davis

remarked that if the particles are at all conductive, the conductivity will dominate their polarization mechanism in dc fields [70]. He theorized that the relative conductivities, σ_p/σ_f, are more important than the relative dielectric constants in this case. In fact, if $(k_p/k_f) < (\sigma_p/\sigma_f)$, conductivity dominates the polarization mechanism and the ER system is more responsive to dc fields than to ac fields. Likewise, if $(k_p/k_f) > (\sigma_p/\sigma_f)$, dielectric effects dominate the polarization mechanism and the ER system is more responsive to ac fields than to dc fields. Particles surrounded by a conductive (ionic) layer are functionally equivalent to fully conductive particles [70]. Increasing ER activity with increasing field frequency may indicate the transition from a weak, conductivity-based, polarization mechanism to a stronger, dielectric-based, polarization. In proposing the use of conductive particles, such as oxidized aluminum, for ER suspensions, Davis suggests that much greater dipole moments can be generated with a conductivity-based mechanism than with dielectric polarization [71].

Issues of electrical break-down, excessive currents, and particle settling make these suspensions impractical. Suspensions with high k_p/k_f or σ_p/σ_f do not exhibit the increase in yield stress that these ratios would indicate. In fact, many of the most active ER suspensions have small dielectric constant ratios k_p/k_f [93].

Microscope observations of single chain deformations due to a flowing continuous phase was successfully modeled by point dipole pair interactions [53]. The slowly flowing oil applied viscous forces on the chain. For purposes of viscous force computation, the chain was modeled as a thin cylinder. Near the electrodes, the chain was several particles thick, and the deformations were much smaller than the point dipole pair model predicted [53]. Again, many particle effects on ER behavior are especially important at high volume fractions.

Minimizing the Coulomb energy of a three-dimensional lattice of an ideal ER fluid with weightless spherical particles, Tao found that the preferred structure was a body centered tetragonal (bct) lattice [270]. In laser diffraction experiments, using mono-disperse 20 micron diameter glass microspheres as the particulate phase, the bct lattice was confirmed [52]. No indication of face centered cubic or body centered cubic configurations was seen. Further Monte-Carlo simulations showed that the formation of single strands at low electric fields has an insignificant effect on the structure order when compared to the highly ordered bct lattice formation [271, 272].

2.6 Response Times of ER Suspensions

The broad range of controllable properties of ER suspensions are useful for semi-active damping applications only if they can be modified instantaneously upon demand. The fast response times of many ER materials is a key property for a variety of control applications. In combined structure visualization and shear stress measurements, Klingenberg and Zukowski note two time-scales: an instantaneous formation of a skeletal structure, and a coarsening of the structure over a period of minutes [156].

Using the point dipole pair interaction energy (2.1), and the Stokes flow resistance equation, Whittle calculated characteristic particle velocities and response times [297]. The characteristic time, t^*, is $t^* = Mn/\dot{\gamma}$.[10] Depending on the field intensification effects and the viscosity of the continuous phase, t^* can range from 0.05ms to 10ms. In high shearing regions, no aggregation is observed. Simulation results illustrated that aggregation kinetics are governed by at least three interaction time-scales [297].

[10]This characteristic time scale is independent of the shear rate.

1. Repulsions between particles perpendicular to the field occur within $0.1t^*$.

2. Chains are created within $5t^*$.

3. Chains consolidate into thicker columns within $90t^*$.

Incorporating the relation between inter-particle distance and volume fraction. See and Doi [239] derived an aggregate size, s, dependent on the volume fraction and the response time, $s = \phi^{1/2}t^{*1/2}$. This square-root rule corresponds well to exponents obtained from regressions on experimental data, $s = \phi^{0.72}t^{0.50}$.

Halsey, *et al.* studied the kinetics of fibril disassociation. Strong inter-particle electrostatic repulsion forces and Brownian forces act to disrupt the fibrated structure [116]. Strong electric fields over-come the electrostatic repulsions, and the time scale for the Brownian disruption of the fibrated structure is much longer than the time scale for fibril aggregation [117]. However, the Brownian oscillations of particle pairs perpendicular to the electric field are unstable [119, 188].

Adriani and Gast experimentally confirmed the relative magnitudes of strong electrostatic repulsion forces and weak Brownian forces [2]. Digital image analysis of particle chain formation in dilute ER suspensions of Lucite particles confirmed an analytically predicted threshold field for chain formation in ac fields [2]. Slow particle diffusion under weak fields is on the order of Brownian motion. Fast structure disassociation upon removal of the electric field was attributed to strong near field electrostatic repulsions [2].

Hill, *et al.* carried out video image processing of particle aggregation, in a mono-layer of water-coated mono-disperse glass spheres, for ac and dc fields and different particle concentrations [125]. They observed a power-law dependence of response times on concentration and faster response times in suspensions of higher particle

concentration. The response time was defined as the time to form a single bridging fibril [126]. Response times were longer in the case of ac field excitation, especially at low volume fractions. These slower response times were attributed to observed particle oscillation at the electric field frequency. Dielectrophoresis occurred in ac fields, but not in dc fields [125]. Modeling only dipole pair interactions, simulation of particle aggregation times agreed remarkably well with the regression through the dc field test data. The fact that the dipole pair interaction model successfully predicts response times, but grossly underestimates yield stresses, suggests that the electric field intensification and multiple particle interactions found in highly structured ER materials does not play an important role when the particles are not fibrated [159]. Column formation times t_c were related to t^* by a power law on the area fraction, ϕ_a [159],

$$t_c = 3\phi_a^{-3} t^*. \tag{2.15}$$

These response times are somewhat longer than those predicted by Whittle, [297], but were independently confirmed in another simulation study [136].

A normal mode approach was used to model the plurality of time-scales involved in structure formation in a shear field [268]. The stress response to a step in the electric field was modeled as a sum of exponentials, each with its own time scale. Using three modes, this function matched experimental results quite well. For $t \ll t^*$ long-range electro-static interactions dominated. For $t < t^*$ particles joined to form short chains, and when $t \approx t^*$ chains percolated to the electrodes.

In another series of stress response tests, the response time was seen to decrease with shear rate [129]. Again, three time scales were observed. Following a step change in field, the measured stress started to increase after a 0.2 ms delay. The stress then increased rapidly for 2–3 ms, and asymptotically achieved a steady state

level. Response times as well as shear stresses decreased with increasing steady shear rates. The response to ac fields was also investigated. Frequency response measurements were collected for several bias electric fields, shear rates and temperatures. In all the cases, the response was flat up to 100 Hz. The response times decreased with bias voltage, shear rate, and temperature [129]. At higher bias fields, there is more structure, greater field intensification, and therefore stronger and faster interactions. Temperature increases ion mobility, and therefore reduces response times. The decrease of response times with increasing shear rate, however, can not be explained with the structure formation kinetics postulated by other authors.

In a third set of stress response tests, ER fluid was subject to pressure driven flow through a rectangular duct [291]. A square 4 kV voltage signal was applied at 20 Hz and the pressure response was measured. Decreasing the volume fraction of the fluid was found to *shorten* the response times [214, 291]. This is the opposite of what aggregation visualization and simulation methods predict. The increasing pressure asymptotically approached a steady state value, but upon removal of the field, the drop in pressure was practically instantaneous. With some fluids, the maximum pressure increased with each cycle of the electric field. The pressure response of other fluids had a low-pass filtering effect on the applied field. The characteristic time, t^*, for these fluids, was evidently much longer than the period of the electric field. From these studies, it may be concluded that pressure response times are material-specific.

Further studies linked a one milli-second delay in pressure response to the charging of the electrodes, via measurement of the charging current. When the current decreased to a steady value, the pressure response reached its maximum. In general, this electric/hydraulic transient lasted 5 milli-seconds [43].

Incorporating a threshold electric field into a quadratic (non-ohmic) current-voltage relationship for ER materials, Whittle was able to accurately model the current and yield stress transient response to a step increase in the applied voltage. Using a similar approach he was able to precisely model the pressure response to an oscillating flow and an oscillating voltage [298].

2.7 Summary

Electrorheological (ER) materials are suspensions of micron-sized particles in electrical insulating oils. The material properties of ER suspensions respond within milliseconds to strong electric fields. Pre-yield, yielding, and post-yield mechanisms are all influenced by the electric field. Namely, an applied electric field dramatically increases the stiffness and energy dissipation properties of these materials.

The exact mechanisms responsible for the ER effect are not fully understood [93, 97]. The polarization of the suspended particles, their electro-static interactions, and the ensuing formation of a fibrated structure are all trivial consequences of the electric field. The point dipole pair interaction mechanisms only partially describe the behavior observed in these suspensions. Theoretical predictions of optimal material formulations (k_p/k_f, σ_p/σ_f, and ϕ) have not been experimentally verified. Indeed, many materials show an ER effect which is not consistent with the predictions regarding k_p/k_f and σ_p/σ_f [93]. A volume fraction between 0.3 and 0.4 is generally held to give the greatest strength and the fastest response times.

Primitive ER suspensions can be made easily by mixing starch, cellulose, or silica, with cooking oil or mineral oil. Although a strong ER effect is sometimes observed in these materials, they suffer from:

- settling and irreversible sedimentation of the particulates,

- uncontrollable ER activity levels,
- high electrical conductivities, and
- low dielectric break-down strengths.

These deficiencies are mainly due to mobile ions or polar molecules (water) in the dispersed or continuous phase.

Recent discoveries of anhydrous, intrinsically electrorheological, gels addressed many of these draw-backs. These materials feature:

- higher yield stresses (approaching 7 kPa),
- slow settling rates,
- low electrical current densities, and
- higher dielectric strengths.

This breakthrough led to numerous theoretical and experimental investigations into the ER effect. In many computer simulations, an assumed polarization and electrostatic interaction mechanism was included in a micro-mechanical model for the suspension. Simulated stresses could match experimental results if the models included:

- non-zero particle sizes,
- multiple particle interactions, and
- local electric field intensification.

Mechanically, chemically, or electrically modifying the electrode surface properties seems like a promising approach toward increasing ER yield stresses.

The fast response times of ER materials are almost as important as their range of controllable properties. Theoretical and experimental studies indicate that the response time is independent of the local mechanisms governing the magnitude of the ER effect.

The next chapter describes the steady flow of ER materials in dash-pot style damper geometries. A salient aspect of the transient fluid flow is analyzed, and geometries which disallow the use of the Bingham approximation are described.

CHAPTER III

THE FLOW OF ELECTRORHEOLOGICAL FLUIDS

In sealed fluid filled dampers which resist linear motion, fluid is typically forced through thin laminar passageways. Using the Bingham model, an analysis of the steady flow of ER materials through rectangular ducts (Poiseuille flow) leads to simple approximations which are useful in designing ER dampers. The Bingham assumption is central to the development of the equations in this chapter and in subsequent chapters. The stress - strain rate relationship described by the Bingham model is descriptive of ER materials only in the limiting case of steady flow. Experiments described in Chapter VI evaluate the appropriateness of this assumption for oscillating flows and transient electric fields.

3.1 Poiseuille Flow of Electrorheological Fluids

For any incompressible, generalized Newtonian fluid, in quasi-steady, one-dimensional flow, the pressure gradient, $\frac{\partial p}{\partial x}$, along the flow, u, is resisted by fluid shear stresses, τ, which are related to the dissipative mechanisms (viscous or otherwise). The Navier-Stokes equations describe the flow of dissipative media [294], and reduce to

$$\frac{\partial}{\partial y}\left[\tau\left(\frac{\partial u}{\partial y}\right)\right] - \frac{\partial p}{\partial x} = 0 \tag{3.1}$$

for the case at hand (flow through a parallel-walled rectangular duct). Consider the steady shear and pressure-driven flow in a narrow rectangular duct with cross section $b \times h$ ($h \ll b$). See Figure 3.1. One of the walls is moving with a velocity U with respect to the other wall. Integrating (3.1) with respect to y, the fluid shear stress, τ, is a linear function of the coordinate y across the stream-lines,

$$\tau(y) = \tau_w - p'y, \tag{3.2}$$

where τ_w is the shear stress at the wall ($y = 0$), and $p' = -\frac{\partial p}{\partial x}$. Assuming ideal Bingham plastic behavior, if $\tau_w < \tau_y$, there will be no flow anywhere in the duct. For a prescribed flow rate, Q, and independent wall velocity, U, τ_w must therefore be greater than τ_y. The shear rate at the wall, $\dot{\gamma}_w$, follows from the Bingham constitutive equation and the Navier-Stokes relation,

$$\dot{\gamma}_w = \frac{\tau_w - \tau_y}{\eta} = \frac{1}{\eta}\left(\frac{1}{2}p'h - \tau_y \mathrm{sgn}(\dot{\gamma})\right), \tag{3.3}$$

and, naturally, $\dot{\gamma}$ equals 0 when $|\tau| < |\tau_y|$. Under steady flow conditions, there are two coordinates, y_1 and y_2, at which $|\tau(y)| = |\tau_y|$, as is shown in Figure 3.1 [227].

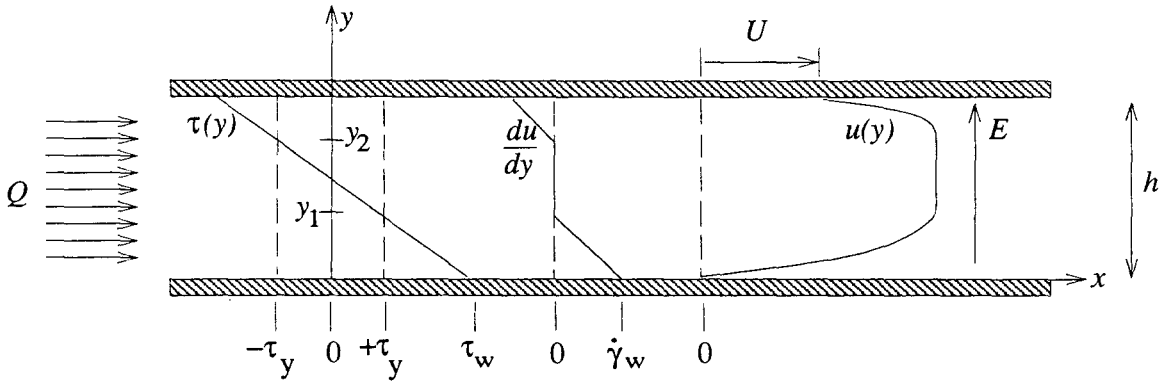

Figure 3.1: Poiseuille flow of Bingham materials.

$$y_1 = \frac{\tau_w - \tau_y}{p'} \tag{3.4}$$

$$y_2 = \frac{\tau_w + \tau_y}{p'} \tag{3.5}$$

In the region $y_1 < y < y_2$, $\dot{\gamma} = 0$, and the ER material will move as an un-sheared "plug". Because $\dot{\gamma}(y) = du/dy$ decreases linearly with y, $u(y)$ is a quadratic function of y, and the flow velocity of the plug is the maximum flow velocity of the ER material $u_{\max}$. Setting $u(0) = 0$, the plug flow velocity is

$$u_{\max} = \frac{1}{2}\dot{\gamma}_w y_1. \tag{3.6}$$

Substituting (3.3) and (3.5) into (3.6), a quadratic form in stress, is obtained,

$$u_{\max} = \frac{1}{2\eta}\left(p'h\tau_w - \tau_w\tau_y - \tau_y p'h + \tau_y^2\right), \tag{3.7}$$

assuming $0 < y_1 < h$. Hence, there are at most three flow regions in a prescribed steady ER Poiseuille flow.

$$\frac{du}{dy} = \begin{cases} \dot{\gamma}_w\,(1 - y/y_1) & \text{if } y < y_1 \\ 0 & \text{if } y_1 \le y \le y_2 \\ \dot{\gamma}_w\,(y_2/y_1 - y/y_1) & \text{if } y_2 < y \end{cases} \tag{3.8}$$

Integrating (3.8) and applying the no-slip boundary condition $u(0) = 0$, three flow velocity profiles are obtained

$$u(y) = \begin{cases} \dot{\gamma}_w\left(y - \frac{y^2}{2y_1}\right) & \text{if } 0 < y < y_1 \\ \frac{1}{2}\dot{\gamma}_w y_1 & \text{if } y_1 < y < y_2 \\ \frac{1}{2}\dot{\gamma}_w\left[y_1 - \frac{1}{y_1}\left(y_2^2 - 2y_2h + h^2\right)\right] & \text{if } y_2 < y \end{cases} \tag{3.9}$$

Each of these three regions may lie partially or entirely in the region $0 < y < h$. Applying the constraint $y_1 < y_2$, six possible flow profile types result. These are summarized graphically in Figure 3.2. The profile types are specified by the relative values of 0, y_1, y_2, and h. Types **III** and **IV** are qualitatively similar, but differ only with respect to the sign of the wall velocity. A distinction is made here, because, in the case of dash-pot style dampers, $QU > 0$ is prescribed by continuity conditions.

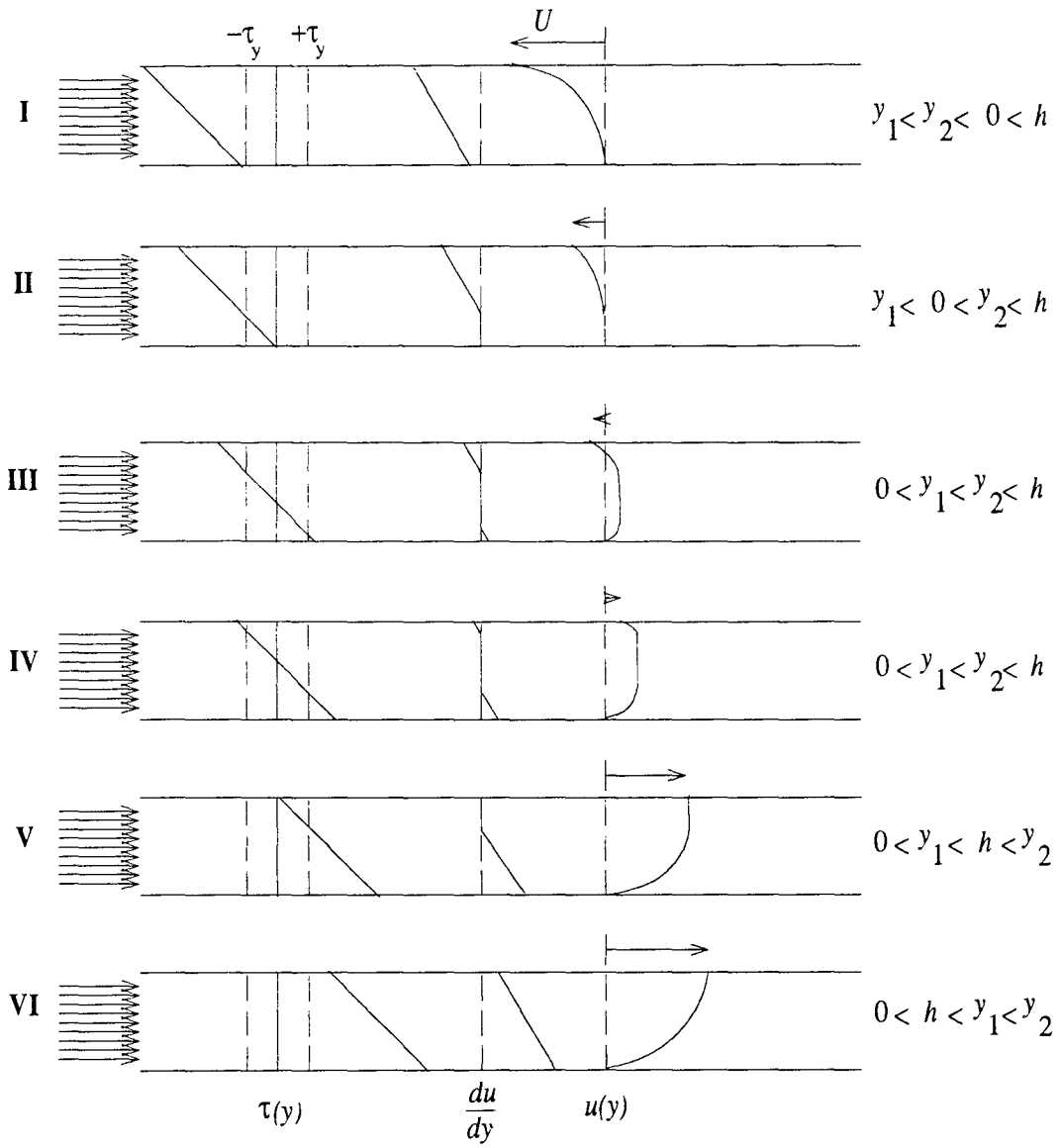

Figure 3.2: Six possible stress conditions and the resulting velocity profiles.

Hence, types **I**, **II**, and **III** are not kinematically permissible, leaving types **IV**, **V**, and **VI**.[1]

For each of the admissible profile types, (**IV**, **V**, and **VI**) continuity and equilibrium conditions lead to expressions for the wall velocity, U, and the flow rate, Q.

$$U = \begin{cases} \frac{1}{2}\dot{\gamma}_w \left(y_1 - \frac{1}{y_1}(h - y_2)^2\right) & \text{if } 0 < y_1 < y_2 < h \\ \frac{1}{2}\dot{\gamma}_w y_1 & \text{if } 0 < y_1 < h < y_2 \\ \dot{\gamma}_w \left(h - \frac{h^2}{2y_1}\right) & \text{if } 0 < h < y_1 < y_2 \end{cases} \tag{3.10}$$

and

$$Q = \begin{cases} \frac{1}{2}b\dot{\gamma}_w \left[-\frac{1}{3}{y_1}^2 + y_1 h - \frac{1}{y_1}\left(y_2^2 h - y_2 h^2 + \frac{1}{3}(h^3 - y_2^3)\right)\right] & \text{if } 0 < y_1 < y_2 < h \\ \frac{1}{2}b\dot{\gamma}_w \left[-\frac{1}{3}y_1^2 + h y_1\right] & \text{if } 0 < y_1 < h < y_2 \\ \frac{1}{2}b\dot{\gamma}_w \left[h^2 - \frac{h^3}{3y_1}\right] & \text{if } 0 < h < y_1 < y_2 \end{cases} \tag{3.11}$$

where b is the width of the rectangular duct ($h/b \ll 1$).

3.1.1 Non-dimensional Forms

In 1969, Phillips [220], cast the Bingham flow equations into dimensionless forms, and combined (3.10) and (3.11) into a single non-dimensional equation. Equations (3.10) and (3.11) can be combined by expressing y_2 as a distance from the moving wall at $y = h$. Analysis of the dimensionless equations resulted in conditions on the pressure gradient, volumetric flow rate, wall velocity, and yield stress, for plug flow formation. One useful set of dimensionless variables is:

$$P = \frac{p'}{p'_N} = \frac{bh^3 p'}{12Q\eta} \tag{3.12}$$

$$T = \frac{\tau_y}{h p'_N} = \frac{bh^2 \tau_y}{12Q\eta} \tag{3.13}$$

[1] In dash-pot style ER devices only Type **IV** profiles can occur. (See Appendix B.)

$$V = \frac{Q_s}{Q} = \frac{bhU}{2Q} \tag{3.14}$$

$$A = P - 2T \tag{3.15}$$

where p'_N is the pressure gradient of a Newtonian fluid ($\tau_y = 0$), and Q_s is the volume flow rate for pure shear flow. The dimensionless pressure gradient, P, has physical significance as the dynamic range of a flowing ER material. It is the ratio of the pressure gradient of a flowing ER material with a yield stress, τ_y, to the pressure gradient of a flowing ER material with no yield stress. The dimensionless yield stress, T, has a normalization similar to P. The dimensionless wall velocity, V, is the ratio of a pure shear flow rate to the total (shear and pressure driven) flow rate. And A is the dimensionless excess pressure gradient required to flow a Bingham fluid. Using these dimensionless variables, the flow equation (3.11) become [220]

$$P^3 - (1+3T)P^2 + 4T^3 + P^2V + \frac{P^2TV^2}{3A^2} = 0 \qquad |V| \le \tfrac{3A^2}{P} \qquad 0 < y_1 < y_2 < h \tag{3.16}$$

$$P = \frac{4V^3}{27(2V-1)^2} \qquad \tfrac{3A^2}{P} \le V \le 3P \qquad 0 < y_1 < h < y_2 \tag{3.17}$$

$$P = -\frac{4}{27}V^3 \qquad -3P \le V \le \tfrac{3A^2}{P} \qquad y_1 < 0 < y_2 < h \tag{3.18}$$

$$P + V = 1 \qquad |V| < 3P \qquad h < y_1 \text{ or } y_2 < 0 \tag{3.19}$$

Equation (3.16) describes the flow in all dash-pot style dampers.[2] This flow condition results in a detatched plug between the plates. Note that the other three equations are independent of the yield stress, T. In these cases, the pressure gradient depends

[2]See Appendix B for a proof.

only on the flow and geometry, and a controllable yield stress can in no way influence the device forces.

3.1.2 Solutions of the Dimensionless Poiseuille Flow Equations

Although (3.16) is 25 years old, general solution methods and accurate closed form approximations have not yet appeared in the literature. If $U = 0$, then $V = 0$, and (3.16) becomes a cubic in P. This cubic has the root

$$P(T) = \frac{2}{3}(1+3T)\left[\cos\left(\frac{1}{3}\arccos\left(1-54\left(\frac{T}{1+3T}\right)^3\right)\right)+\frac{1}{2}\right]. \tag{3.20}$$

Details regarding the solution to (3.16) are elaborated in Appendix B. A uniform approximation to (3.20) was found by trial and error and is accurate to within $\pm$ 2% over most of the interval $0 < T < 1000$.

$$P(T) = 1 + 2.07T + \frac{T}{1+0.4T} \pm 2\% \tag{3.21}$$

A linear approximation, $P \approx 1 + 2.5T$, had been recommended for the range $0.5 < T < 100$ [43, 80] but the relative error of this approximation is 20% over this small range of T. The root (3.20) and its approximation (3.21) are plotted in Figure 3.3. The the relative error of the approximation (3.21) to (3.20) is shown in Figure 3.4. Given material properties, τ_y and η, the duct geometry, b and h, and the flow rate, Q, (3.20) determines the responding pressure gradient. This relation is useful in analytically simulating the behavior of flowing Bingham materials, and in designing devices based on steady flow. Pressure gradient measurements in several Poiseuille flow geometries verified that (3.16) is representative of actual ER flows to within 5% [36, 40, 67, 292]. Experiments described in Chapter VI give further support to (3.21). Hence (3.21) can be used to design ER devices in which the flow is steady.

For flow case **IV**, case $|V| \leq 3A^2/P$, the polynomial is fifth degree, and no general solution exists for the roots. For dash-pot devices, constraints on the possible

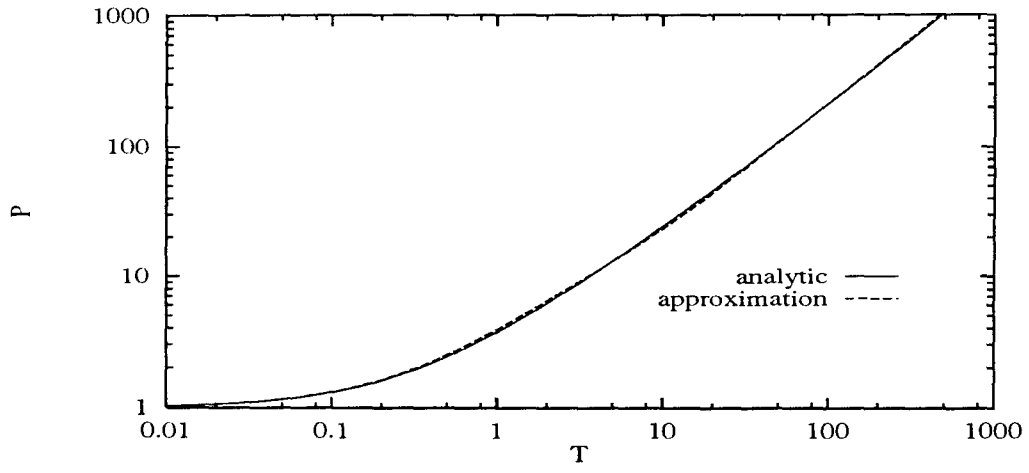

Figure 3.3: Solution to the cubic Bingham flow equation.

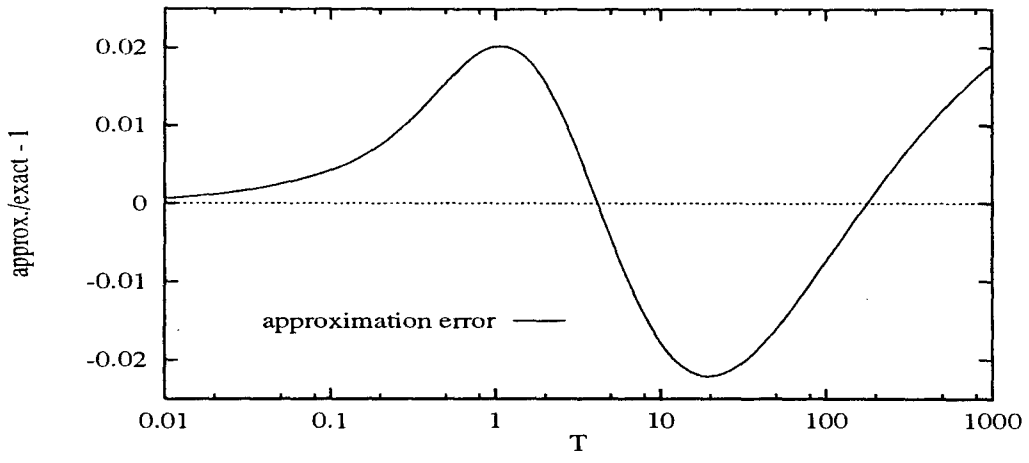

Figure 3.4: Error of the approximation to the exact solution of the cubic Bingham flow equation.

flow conditions ($QU > 0$) simplify the solution to this equation. Numerical and approximate solutions to (3.16) for such devices are described in Appendix B. The expression

$$P(T,V) = 1 + 2.07T - V + \frac{T}{1+0.4T} - \frac{1.5TV^2}{1+0.4T^2} \pm 3\% \qquad (3.22)$$

approximates the desired root of (3.16) in these cases and reduces to (3.21) if $V = 0$. Another application of (3.16) is the determination of material properties from measured flow rates and pressure gradients. Numerical methods for performing estimation of τ_y and η from Poiseuille flow data (b, h, p', Q, and U) are described in Appendix B.

Both P and T depend on the gap size, h, and flow rate, Q. So, given ER material properties, the dynamic range of an ER device is a function of h and Q. This is illustrated in Figure 3.5. Devices with wider gaps and lower flow rates have larger dy-

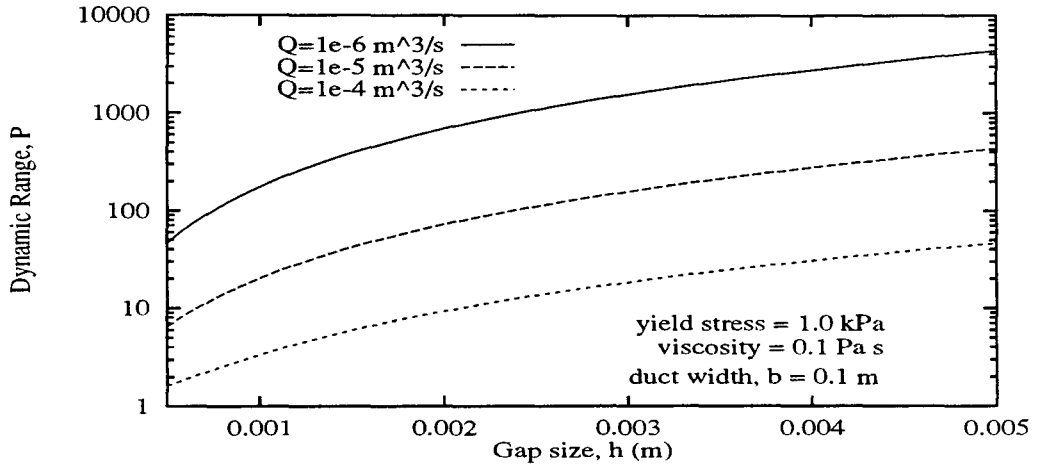

Figure 3.5: Dynamic range, P, as a function of gap size, h, and flow rate, Q.

namic ranges. The dynamic range increases exponentially with a linearly increasing gap.

3.2 ER Flow Transients

The effects of time-varying material properties, sinusoidal wall motions, and flow development at the duct inlet, disturb any fully developed flow profile. The approximation (3.22), which is the basis for the design and analysis of ER fluid dampers, in no way describes the complex behavior of ER materials as the shear rates pass through zero. The Navier-Stokes equations for unsteady flow of a generalized Newtonian fluid are

$$\nabla \cdot \mathbf{T}(\nabla \mathbf{u}) - \nabla p = \rho \frac{D\mathbf{u}}{Dt}, \tag{3.23}$$

where $\frac{D}{Dt}$ is the material derivative and $\mathbf{T}$ is the deviatoric portion of the stress tensor. Considering the case of duct flow, $\mathbf{u} = (u, v)^T$, expanding (3.23) into rectangular coordinates, and including only the shear stress τ, leads to

$$\frac{\partial \tau}{\partial y}\left(\frac{\partial u}{\partial x}, \frac{\partial u}{\partial y}, \frac{\partial v}{\partial x}, \frac{\partial v}{\partial y}\right) - \frac{\partial p}{\partial x} = \rho\left(\frac{\partial u}{\partial t} + \frac{\partial u}{\partial x}\frac{\partial x}{\partial t} + \frac{\partial u}{\partial y}, \frac{\partial y}{\partial t}\right) \tag{3.24}$$

$$\frac{\partial \tau}{\partial x}\left(\frac{\partial u}{\partial x}, \frac{\partial u}{\partial y}, \frac{\partial v}{\partial x}, \frac{\partial v}{\partial y}\right) - \frac{\partial p}{\partial y} = \rho\left(\frac{\partial v}{\partial t} + \frac{\partial v}{\partial x}\frac{\partial x}{\partial t} + \frac{\partial v}{\partial y}, \frac{\partial y}{\partial t}\right) \tag{3.25}$$

Solutions of (3.25) and (3.25) in the $x-y$ plane are commonly carried out numerically.

3.2.1 The Bingham-to-Newtonian Transient

The transient of primary importance (for control applications) that a flowing ER material will experience is the change from a nearly-plugged Bingham flow to a Newtonian flow. The initially rectangular ER flow profile asymptotically approaches a parabolic Newtonian profile when the electric field is instantaneously switched off. The yield stress is assumed to drop to zero much more quickly than the dissipation rate of the ensuing flow transient.[3] Because the yield stress is assumed to vanish

[3]Close range repulsive forces between particulates in the ER suspension contribute significantly to the fast disruption of structure (and the associated drop in yield stress) commonly observed in ER suspensions.

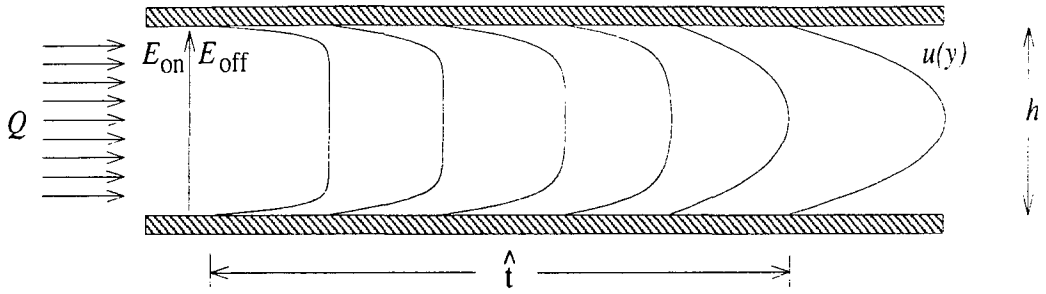

Figure 3.6: Development of a Newtonian flow profile from a Bingham flow profile.

instantaneously, the development of the transient flow profile is governed by Newtonian fluid mechanics. Evaluating the effect of fluid inertia on the flow transient of ER materials is the purpose of this section.

The Bingham to Newtonian flow transient is governed by

$$\rho\frac{\partial u}{\partial t} = \eta\frac{\partial^2 u}{\partial y^2} + p', \tag{3.26}$$

and is subject to no-slip boundary conditions at the walls

$$u\left(\pm\frac{h}{2}, t\right) = 0, \tag{3.27}$$

and an assumed initial flow profile,

$$u(y, t_0) = U_0[1 - (2y/h)^n], \tag{3.28}$$

where the exponent n is much greater than one. Equation (3.26) is a non-homogeneous, parabolic, partial differential equation. The associated homogeneous partial differential equation is

$$\frac{\rho}{\eta}\frac{\partial u}{\partial t} = \frac{\partial^2 u}{\partial y^2}. \tag{3.29}$$

This mixed, boundary value problem - initial value problem can be solved by assuming that the solution, $u(y,t)$, can be separated in the form

$$u(y,t) = \mathcal{Y}(y)\mathcal{T}(t). \tag{3.30}$$

The homogeneous partial differential equation is solved first. Substituting (3.30) into (3.29), leads to two ordinary differential equations:

$$\mathcal{T}' - \lambda\frac{\eta}{\rho}\mathcal{T} = 0, \tag{3.31}$$

and

$$\mathcal{Y}'' - \lambda\mathcal{Y} = 0, \tag{3.32}$$

where λ is the eigenvalue of (3.29). Analyzing these ordinary differential equations leads to trial solutions

$$\mathcal{T}(t) = Ae^{\lambda\eta t/\rho}, \tag{3.33}$$

and

$$\mathcal{Y}(y) = Be^{\sqrt{\lambda}y} + Ce^{-\sqrt{\lambda}y} \tag{3.34}$$

The unknown constant coefficients, A, B, and C will be determined by applying the boundary conditions (3.27). From physical knowledge of the problem, we know that the solution of the homogeneous (transient) partial differential equation remains bounded for all time. Therefore, because $\eta > 0$ and $\rho > 0$, λ must be less than zero. Defining $\beta^2 = -\lambda$, the homogeneous solution becomes

$$u_{\mathrm{h}}(y,t) = Ae^{-\beta^2\eta t/\rho}\left(B\sin\beta y + C\cos\beta y\right). \tag{3.35}$$

Substituting (3.27) into (3.35), and noting that the initial condition (3.28) is an odd function, leads to $B = 0$ and $\beta = (2k-1)\pi/h$, $(k = 1, ..., \infty)$. Therefore, the solution to (3.29) subject to (3.27) is

$$u_{\mathrm{h}}(y,t) = \sum_{k=1}^{\infty} D_k e^{-[(2k-1)\pi/h]^2\eta t/\rho}\cos[(2k-1)\pi y/h]. \tag{3.36}$$

The coefficients D_k will be solved using (3.28).

The (time-invariant) solution to the particular (steady-state) partial differential equation

$$\eta \frac{\partial^2 y}{\partial y^2} = -p' \tag{3.37}$$

is the well-known parabolic, fully-developed, flow profile of a Newtonian fluid through a rectangular duct.

$$u_{\mathrm{p}}(y, \infty) = \frac{3}{2} U_0 (1 - (2y/h)^2). \tag{3.38}$$

The mean flow velocity, U_0, is equal to $p'h^2/(12\eta)$.

Now the homogeneous and particular solutions are combined into:

$$u(y,t) = u_{\mathrm{h}}(y,t) + u_{\mathrm{p}}(y,\infty). \tag{3.39}$$

Substituting (3.36) into (3.39), setting $t = t_0$, and re-arranging, leads to

$$u(y,t_0) - u_{\mathrm{p}}(y,\infty) = \sum_{k=1}^{\infty} D_k \cos[(2k-1)\pi y/h]. \tag{3.40}$$

The coefficients D_k are then obtained using the Fourier Theorem,

$$D_k = \frac{1}{h} \int_{-h/2}^{h/2} [u(y,t_0) - u_{\mathrm{p}}(y,\infty)] \cos[(2k-1)\pi y/h] dy, \tag{3.41}$$

where $u(y,t_0)$ and $u_{\mathrm{p}}(y,\infty)$ are assumed. This completes the solution.

The Fourier integral (3.41) was solved numerically using 100 integration points. One hundred terms were retained in the series expansion (3.36). Then these values for D_k were substituted into (3.39) and flow profiles were calculated at various times. The flow velocity was non-dimensionalized by dividing by U_0, the cross-flow dimension was non-dimensionalized by dividing by h, and time was non-dimensionalized by dividing by a characteristic time, $\hat{t}$, $\hat{t} = \rho h^2/\eta$. The non-dimensional flow transient is shown in Figure 3.7. The maximum flow velocity reaches 0.707 of its final velocity ($1.5U_0$) in $0.019\hat{t}$ and 0.99 of its final velocity in $0.22\hat{t}$. In a simplified analysis,

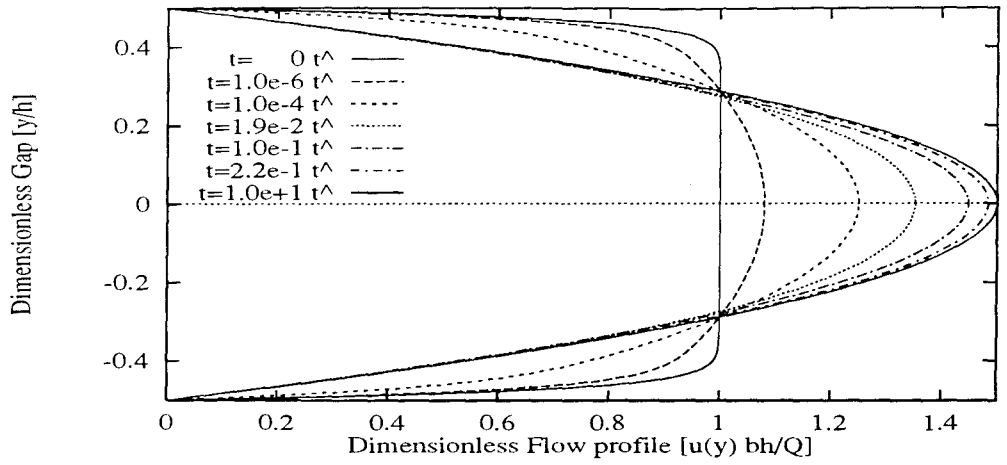

Figure 3.7: Flow transient from Bingham to Newtonian behavior.

Phillips found that the transient time could range from $0.04\hat{t}$ to $0.08\hat{t}$ [220]. For typical materials, $\hat{t}$ can range from 1 ms (h=1 mm) to 10 ms (h=3 mm). Like the dynamic range, P, $\hat{t}$ increases with h^2. So, $\frac{\hat{t}}{\rho}$ can be substituted for $\frac{h^2}{\eta}$ in (3.14). An example of the inter-dependence of P and $\hat{t}$ is illustrated in Figure 3.8 (for devices where $V \approx 0$). The trade-off between dynamic range and response time is controlled

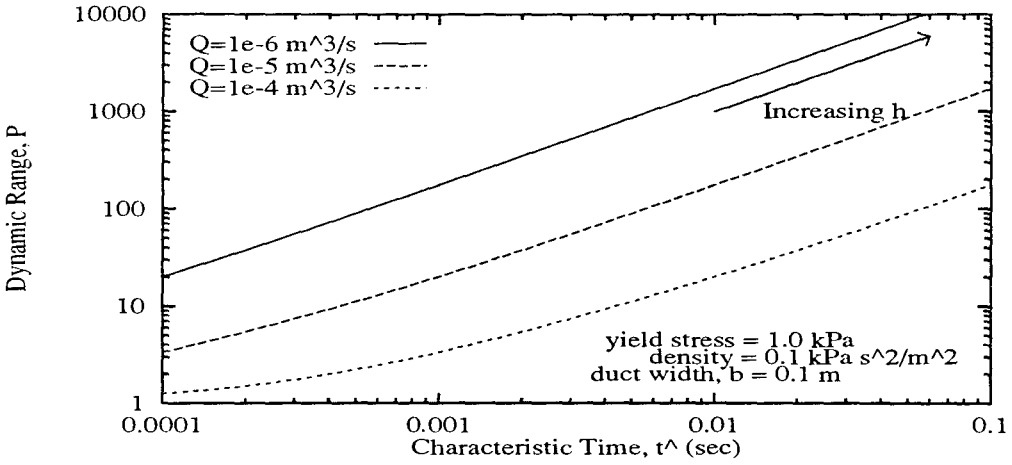

Figure 3.8: Dynamic range, P, as a function of response time, $\hat{t}$, and flow rate, Q.

by the gap size h. Flowing ER materials can not simultaneously have a short response time and a high dynamic range. Increasing h to achieve a larger dynamic range is

done at the expense of slower transients. For gaps less than 1 mm, the speed of the material property transition, not the inertial effects, dominates the total fluid response time.

The response time depends on the nature of the ER effect as well [35]. This analysis is contingent on fast material response times, $t^* = Mn/\dot{\gamma}$. Because the longer time-scales associated with coarsening of fibrils, material response times are longer for anti-thixotropic (thickening) changes than for thixotropic (thinning) changes (high τ_y to low τ_y). ER devices described in the literature commonly have dynamic ranges of 5-15 at frequency band-widths of 100 Hz - 300 Hz [36, 82, 246, 255, 279].

There are limiting factors which control the range of possible gap sizes. Coagulating particles can block small gaps even at $E = 0$. Gap sizes are limited by the voltages required to produce electric fields of 3–7 kV/mm [43]. As the device voltage approaches 20 kV, X-rays are produced. Hence, gaps in ER devices should range from 0.2 to 3.0 mm.

3.2.2 Entrance Effects

Entrance effects in ER devices are most pronounced for Newtonian flow at large Reynolds numbers. The initial flow profile is qualitatively similar to that of a "plugged" Bingham flow profile. So the entrance effects for Bingham flow can be considered small as compared to the entrance effects for Newtonian flow. The dimensionless entrance length (normalized by the gap size), is a small fraction of the Reynolds number for Newtonian flow [294]. Properly designed ER devices operate with small viscous stresses and Reynolds numbers, in order to maximize the dynamic range. In the worst case, the longest entrance length is approximately $5h$, and is negligible compared to the total length, l, in many devices ($h \ll l$).

3.2.3 Measurement and Analysis of ER Flow Transients

In a series of low-level oscillating shear measurements on a suspension of corn-starch in mineral oil [275], Thurston extracted storage and loss moduli of the material from the test measurements. In the transition from no electric field to full electric field (1.8 kV/mm) large changes in the material properties were immediately evident. The stiffness and damping subsequently increased linearly with time over a period of 2 minutes to 150% of the initial field-induced values. After 2 minutes at a high electric field, the field was removed, and the material properties returned quickly to their initial values. Because of the long sample period, (20 seconds/sample) the dynamics of the flow transients were not available from this study. The enhancement of material properties with time were attributed to a coarsening of the fibrated structure over a time-scale much longer than that of the initial ER response. The coarsening of the structure is, in fact, accelerated by the low-level cyclic motion [258]. In this sense, ER materials are anti-thixotropic. At higher shear rates, or upon removal of the electric field, the structure degrades and the ER material becomes thixotropic again [192].

Another synergetic mechanism is attributed to the interaction of the electric field, the shear-rate, and the current density [36]. In the plug-flow region, the fibrated structure can translate without shear. Assuming that conductance in the ER material is primarily along fibrated chains, regions of high shear-rate will drop a larger electric potential. In other words, the electric field (and yield stress) is somewhat higher in fast-shearing regions [256, 258]. If the yield stress increases with shear rate, then the yield stress will diminish in a plug and increase near the walls. The flow profile will be more rounded, and the plug will be less evident. It is therefore likely that the material properties of a flowing ER material are not uniform across the flow. This mechanism, which increases the shear stress at a wall, is compensated for by the

higher fibril destruction rate and decreased yield stress within the plug. The net effect is that ER fluids tend to be stronger in shear than in flow.

In a series of tests aimed at capturing the unsteady flow transients caused by quick changes in material properties, pressure response time histories were captured on a storage oscilloscope [215]. An ER fluid of 20% (volume fraction) polymethacrylite particles in a floridated hydrocarbon dielectric fluid was used. A result similar to that of Figures 3.5 and 3.8 was noted in that the dynamic range decreased with higher flow rates. The pressure gradient response to a step change in the electric field was characterized by an initial, practically instantaneous, jump in the pressure gradient, followed by a slower ramp-like increase of the pressure gradient. In designing ER materials for semi-active damping devices, it is desirable for the pressure response to be dominated by the initial jump, and have negligible contribution from the ramping portion. Particles in materials with a higher volume fraction have a shorter distance to travel to form fibrils. So increasing the volume fraction to 30% or 40% can improve the behavior of ER materials in this regard [215]. It is therefore reasonable that materials with higher volume fractions respond more quickly. A slight delay between the application of the high voltage and the initiation of the jump in the pressure gradient was also observed. This delay has been attributed to the charging time of the capacitor-like device, by measurements of the charging current. The delay is generally less than 5 milli-seconds [43], and depends solely on the available charging current.

3.3 Bingham Flow in Other Geometries

Despite the complexity of (3.16), the analysis of Bingham duct flow is more straight-forward than many other commonly encountered flow configurations. For

example, the shear rate of a power-law fluid in the gap of a Couette rheometer does not vary linearly across the gap, and the shear rate at the wall depends on unknown material properties. Correction factors to account for this non-linearity can be as great as 10% [168]. The correction for Couette rheometers commonly used for studies of ER materials is less than 1% [22, 168].

A paradox arises when applying a plug-flow model to flows with diverging stream lines [177]. Consider the steady flow between diverging plates, illustrated in Figure 3.9. For a steady flow, Q, the mean flow velocity must decrease with x. The Bingham

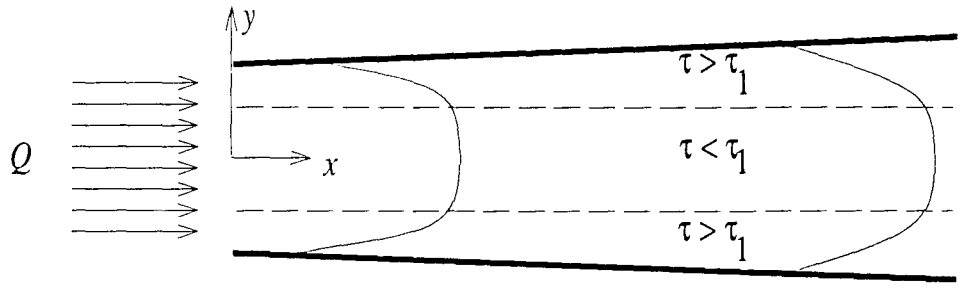

Figure 3.9: Bingham flow between diverging parallel walls.

constitutive law, however, requires that the plug can not deform (its velocity must remain constant). A similar paradox arises in the radial squeeze-film flow between two parallel walls.

To reconcile the continuity and constitutive laws for the flow of yielding materials in such confined geometries, a *bi-viscosity* model has been postulated [177],

$$\tau = \begin{cases} \eta_0 \dot{\gamma} & \text{if } |\tau| \leq \tau_1 \\ \tau_0 + \eta_1 \dot{\gamma} & \text{if } |\tau| > \tau_1 \end{cases}, \tag{3.42}$$

where $\eta_0 \gg \eta_1$ are the viscosities of the bi-viscosity model. The material properties τ_0 and τ_1 are defined in Figure 3.10, and $\tau_0 = \tau_1(1 + \eta_1/\eta_0)$. Finite element analysis of axisymmetric squeeze film flow using a bi-viscosity model was confirmed using an

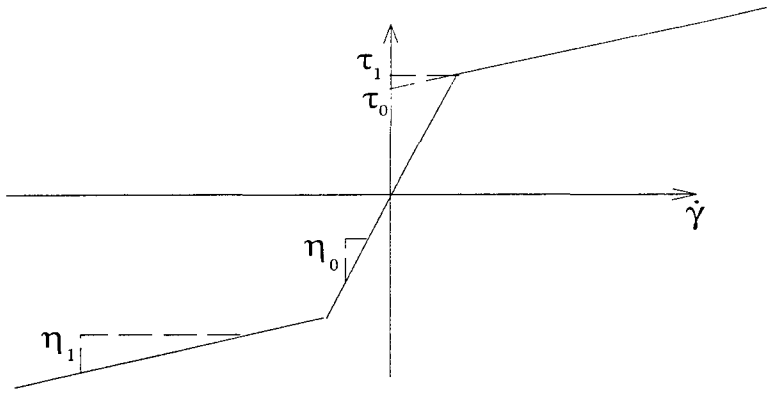

Figure 3.10: The bi-viscosity constitutive model.

analytic bi-viscosity solution [103]. Inclusion of normal stresses in the finite element model did not result in an appreciable difference when compared to the analytic solution (without normal stresses). It was therefore concluded that normal stresses do not play an important role in the flow of bi-viscous materials in confined geometries. If the ratio of the gap size to the radius becomes large, however, normal stresses do become important [302]. A squeeze-film damper using ER fluids was modeled using the bi-viscosity constitutive relations, incorporating normal stresses when relevant [301]. If $\eta_1/\eta_0 < 0.001$ then the modeled behavior was close to Bingham behavior. With a small value of η_1/η_0 and a value of τ_1 derived from material tests, dynamic simulations of the squeeze film damper accurately modeled its observed behavior [262, 302]. ER squeeze film dampers have been used in controlling the lateral (whirling) vibrations of spinning shafts. By adjusting the stiffness and damping of the shaft supports, critical whirling modes can be avoided or moved to much higher frequencies [196, 200].

The flow of Bingham fluids in a variety of other geometries is described in the literature. Atkin [22] analyzed a variety of radial flows. Walton [287] studied the flow of power-law fluids and Bingham fluids along an eccentric annulus. For eccentricities

greater than 0.5, the plug formed only in the wider region of the annulus. Vradis [286] analyzed Bingham flow through a discontinuity in pipe radius for steady flows at low Reynolds numbers. Solutions to the heat conduction problem for a steadily flowing Bingham fluid has been presented as well [139].

The ER effect is not observed when the field is in the same direction as the flow. Hence three-dimensional constitutive relationships are required to describe the generalized behavior of ER materials [227]. In the most general case, the electric field can give rise to asymmetric velocity profiles, as well as shear stresses in the absence of flow [48].

Considering the simpler case of one-dimensional shear flow, (with the electric field perpendicular to the stream lines), the normal stresses, σ_{ii}, and shear stresses, τ_{ij}, can be described by

$$\begin{aligned} \sigma_{11} &= \alpha_1 & & +\tfrac{1}{4}\alpha_4\dot{\gamma}^2 & \\ \sigma_{22} &= \alpha_1 & +\alpha_2 E^2 & +\tfrac{1}{4}\alpha_4\dot{\gamma}^2 & +\tfrac{1}{2}\alpha_6\dot{\gamma}^2 E^2 \\ \sigma_{33} &= \alpha_1 & & & \end{aligned} \tag{3.43}$$

where x_1 and x_2 are the coordinates along and across the flow [227]. The parameter α_1 is a hydro-static pressure; α_2 determines the normal stress parallel to the field; α_4 describes a non-Newtonian effect; and α_6 describes the ER effect. The shear stress, τ_{12} is given by

$$\tau_{12} = \frac{1}{2}(\alpha_3 + \alpha_5 E^2)\dot{\gamma} \tag{3.44}$$

which accounts for field and flow dependent apparent viscosity. In general the parameters α_i are scalar functions of the invariants of the deformation tensor and the electric field vector [227]. The Bingham constitutive model is a special case of these equations.

3.4 Measuring Yield Stresses

Because the yield stress is related to the suspended structure, and because the structure degrades with time (in flowing conditions), the yield stress can be considered a time-dependent quantity [56]. The issue here is the difference between a static yield stress and a dynamic yield stress, as elucidated by Bonnecaze [32]. For thixotropic materials, such as gels, which exhibit only very small dynamic yield stresses, a clear measurement of the (static) yield stress can be difficult to accomplish. In such shear-thinning materials, the yield stress is seen to decrease rapidly with shear rate. Therefore shear stress measurements at very low shear rates ($10^{-2} > \dot{\gamma} > 10^{-6}$) are extrapolated to $\dot{\gamma} = 0$ to determine the static yield stress. For weak colloidal structures, a yield stress can only be observed at shear rates below 10^{-5} [137]. For an ideal Bingham fluid, the extrapolation is linear. For thixotropic materials, the shear stress increases exponentially with decreasing $\dot{\gamma}$. For visco-elastic materials, the shear stress decreases with decreasing shear rate, and shear deformation [56]. ER materials are visco-elastic and thixotropic. Therefore at very low shear rates, other deformation mechanisms (such as visco-elasticity, and creep) can obfuscate the recognition of a static yield stress in ER materials. Indeed, the low shear rate region of ER behavior is the most difficult to model. Thixotropic behavior is often dominant when small shear rates are applied to a quiescent ER fluid [28, 56]. The extrapolated stress at $\dot{\gamma} = 0$ in this case could be considered a static yield stress. Thixotropic effects are absent when a shearing ER fluid is brought to rest. In this case, the extrapolated shear stress is the dynamic yield stress.

Different rheometer geometries aimed at clearly identifying a static yield stress are compared in several reviews [56, 137, 151, 206, 307, 308]. Four basic rheometer

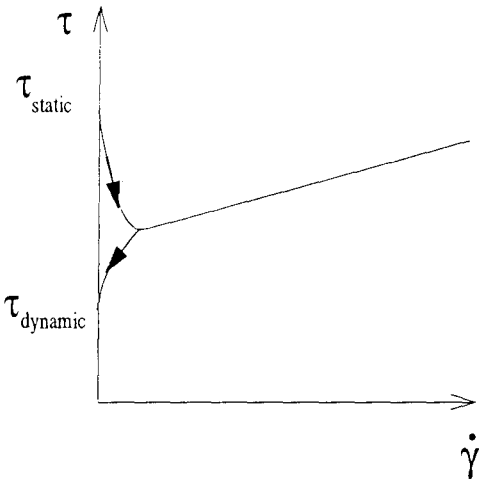

Figure 3.11: Static and dynamic yield stresses in flowing ER materials.

types are described below:

- **Concentric cylinder Couette rheometers** consist of an inner cylinder (*bob*) (which can be rotated by a controlled motor) within the external cylinder (*cup*). Material is sheared in an annular gap between the cylinders, and the torque on the outer cylinder is measured. These rheometers are popular for low shear rate measurements. Intertial effects at higher shear rates can be exploited by modifying the rheometer to directly measure the yield stress. Most rheometers are equipped for shear-rate control experiments. By inserting a compliant, linear spring in series with the motor and the bob, a constant motor speed results in a linearly increasing shear stress when the material is in a pre-yield condition. A static yield stress can be defined as the stress at which the stress history deviates from a linear function of time [56]. A similar analysis can be carried out for linearly increasing shear rates [56, 307]. Oscillating shear strains can be applied in many Couette rheometers. Dynamic yield stresses are observed when the oscillating shear stress history becomes clipped [56, 99].

- **Concentric cone rheometers** are similar to concentric cylinder rheometers, except that the bob and cup are replaced by mating cones. The gap size can be easily adjusted in this rheometer by raising or lowering the bob [307]. Unlike concentric cylinder rheometers, end effects do not present difficulties in data analysis [206].

- **Parallel plate rheometers** carry the modification of the concentric cone rheometer one step further. The mating cones are replaced by parallel circular plates. The pre-yield elasticity of Bingham fluids can also be evaluated using this geometry [308]. But fluid can leave the rheometer cell due to centripetal forces at high shear rates [151].

- **Vane rheometers** are similar to concentric cylinder rheometers except that the bob is replaced with an assembly of vanes. The radius of the outer cylinder is usually about twice the vane diameter. This rheometer is not as susceptible to errors resulting from wall slippage, which are an issue in concentric cylinder rheometers [307]. Similar devices are used in the testing of soils. It is difficult to apply a uniform electric field in these rheometers, and therefore they are not used for studying ER materials.

3.5 Summary

In closing this chapter, it should be reiterated that many important details of ER flow can not be captured by a Bingham model. The Bingham model assumes that the yield stress does not vary within the fluid and that the material is infinitely rigid before it yields. In many flow geometries the Bingham equation is at odds with basic continuity requirements, and a more general, bi-viscosity, equation must be used.

In ER materials, the yield stress is sometimes associated with the degree of particle fibration. Hence, stronger fibrils may be expected to form within an un-sheared plug, whereas particle concentration may be diluted near the walls. On the other hand, the electric current density is also associated with the degree of particle fibration. Stronger electric fields (and higher yield stresses) may be expected near the walls. And electrophoresis of particles may increase the particle concentration at the electrodes. Visco-elastic behavior at low strains is an important characteristic of ER materials. ER fluids tend to be stronger in shear driven flow than in pressure driven flow. There is significant evidence that fibrated particles break and drag along the electrodes. Increasing the adhesion between the particles and the flow surfaces appears to be a promising route toward increased ER yield strengths.

Despite many material complexities, the Bingham constitutive model for ER fluids has been verified experimentally for a number of steady flow configurations [36, 40, 67, 292]. The Bingham model seems to be sufficiently accurate for design purposes.

In this chapter the Navier-Stokes equations were solved for steady flow of a Bingham fluid through rectangular ducts. In general this solution requires finding the roots of a 5^{th} degree polynomial. An approximation to the desired root of this polynomial was presented in this chapter, and is described further in Appendix B.

As well as the steady flow of ER materials, the flow transient due to the changing material properties is addressed. From the analysis in this chapter, is is seen that response times of devices with flowing ER materials increases with the range of available forces of the ER device. Thus the design of ER devices entails the balancing of the dynamic range with the response time. Material response times are longer when the electric field increases than when it decreases.

The next chapter describes devices which utilize ER materials and their applica-

tions.

CHAPTER IV

ER DEVICES

4.1 Applications of ER Materials

ER materials were first applied in the early 1960's in high band-width vibration actuators [23, 254, 255]. Since then, several potential uses for ER materials, ranging from pumps and test equipment to automotive uses and structural vibration control have been recognized [241]. All of the envisioned applications share a common feature. The ER fluid is used to adjust a pressure gradient (*flow mode*) or to provide momentum transfer (*shear mode*). Envisioned flow mode devices include: valves, pumps, flow distributors, brake pushers, fans [241], engine mounts, [79, 81, 83, 217, 262, 279], vehicle suspensions [26, 208, 263, 280], vibration actuators [220], force actuators [178, 179], and structural vibration dampers [198]. Actuator applications require a pump to pressurize or circulate the ER material.[1] Shear mode devices include: vehicle suspensions [36, 65], clutches [47, 122], and brakes [47]. Some devices categorized as shear mode devices actually have a mixture of shear and pressure driven flow [36]. The same ER material will exhibit different response times and yield stresses in flow mode and in shear mode devices. The ER effect has been shown to be repeatable to at least 2,000,000 cycles in these devices [35, 218].

[1] ER materials can not generate forces themselves.

4.1.1 Shear Mode

Shear mode devices require a rotating or circular geometry. They are therefore most efficient when influencing the motion of rotating systems. Designing ER devices to operate in the shear mode has certain advantages. ER dampers for rotational motion can be designed simply and elegantly [36]. Yield stresses tend to be higher in shear mode devices because the ER material properties are roughly uniform in a fluid with uniform shear rates. Response times are faster in shear mode devices because fluid inertia effects are less pronounced. In most shear mode devices, all the fluid in the device can be subject to the electric field; chambers of un-activated fluid are not required. Furthermore, the system seal requirements are more easily satisfied in rotating devices than in reciprocating devices [80]. Dynamic seals have been eliminated entirely from small ER clutches by incorporating a multi-pole magnet assembly to transfer torsion forces through a sealed containment [47]. The small quantity of fluid in shear-mode devices will become hotter than the larger volume of fluid in flow-mode devices, under similar energy dissipation requirements [43]. Rectilinear motion can be translated into rotational motion through the use of a ball screw. ER devices implementing this concept have been designed and tested [65]. To maintain a constant and uniform gap between the electrodes, spacers are sometimes introduced between the plates [236]. These spacers can increase the friction in the device (and decrease the dynamic range) to the point of making them impractical [84]. A conceptual design of a rotational shear-mode device is illustrated in Figure 4.1.

4.1.2 Flow Mode

All flow mode devices are based on the principle of an ER valve. The pressure gradient of ER material flowing through a duct can be controlled by the voltage

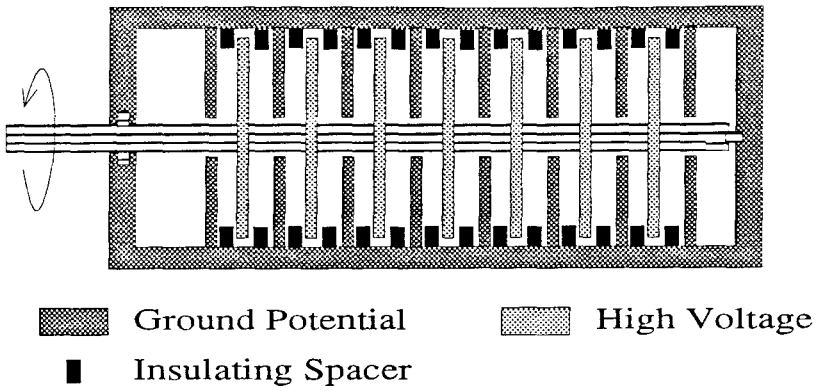

Figure 4.1: A shear-mode ER device.

on the walls of the duct. The walls usually do not move with respect to each other. Therefore precise gap sizes can be achieved by clamping thin (mm) insulating spacers between the walls. The valve can be external to the damper. The fluid flow rate through an external ER valve is independent of the velocity across the damper's terminals. The geometry and size of an external ER valve is not constrained by the requirements of the damper. Because the dynamic range of ER devices depends critically on the fluid flow rate, arbitrarily large dynamic ranges can be achieved with an external ER valve. For rectilinear motions, ER valves are much simpler devices. But such configurations require greater volumes of ER materials, and seal requirements are more difficult to satisfy. Spring energized PTFE seals are suitable in some cases [40]. If the external valve and damper are inter-connected by long or thin tubes, viscous losses in the tubes will diminish the system's dynamic range. A flow mode device with an external ER valve is shown in Figure 4.2. Calculations of the fluid volume required to achieve specified force levels and the associated electrical power requirement show that shear mode and flow mode devices require comparable electrical power, electrode gaps, and geometries [65]. A comparison of a variety of flow mode devices led to the conclusion that parallel wall geometries afford the

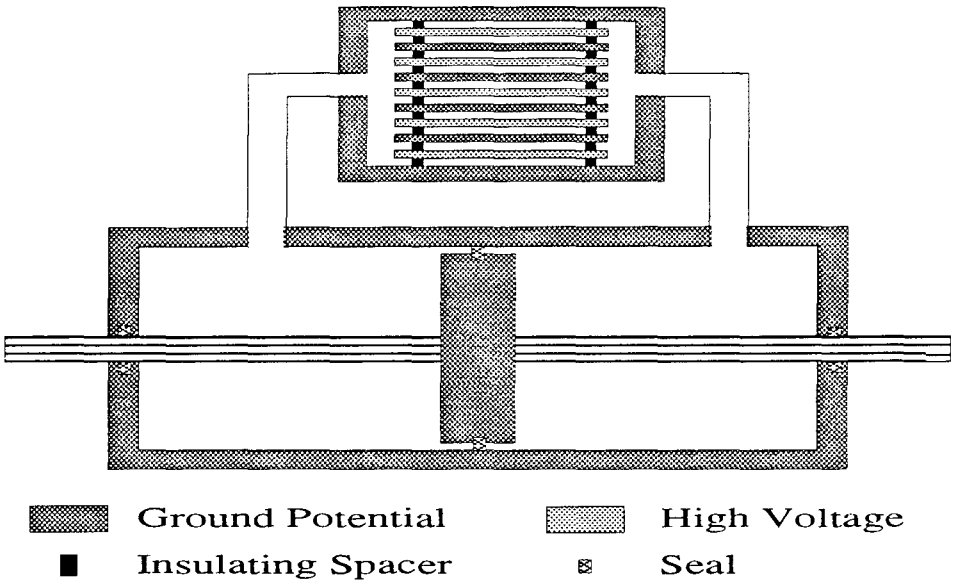

Figure 4.2: A flow-mode ER device.

largest dynamic range. Valves using concentric cylindrical plates have a larger total surface area for a given cross-sectional area [237].

4.1.3 Mixed Mode

By replacing the piston head of the ER damper in Figure 4.2 with the valve itself, the fluid volume requirements are reduced and the losses due to the valve-damper connections are eliminated. (The valve and damper are self-contained.) This type of device is called *mixed mode* because the flow profile between the electrodes and the case of the device is a summation of a shear flow and a pressure flow profile, i.e., Poiseuille flow with a moving wall. The profile is usually dominated by flow rather than shear in these gaps. In a dash-pot configuration (the piston is the valve), the fluid velocity is always greater than the damper velocity, and the valve must be smaller than the damper. Increasing the length of the piston increases the ratio of activated to un-activated ER fluid and increases the force levels. Figure 4.3 shows the configuration of a mixed-mode device.

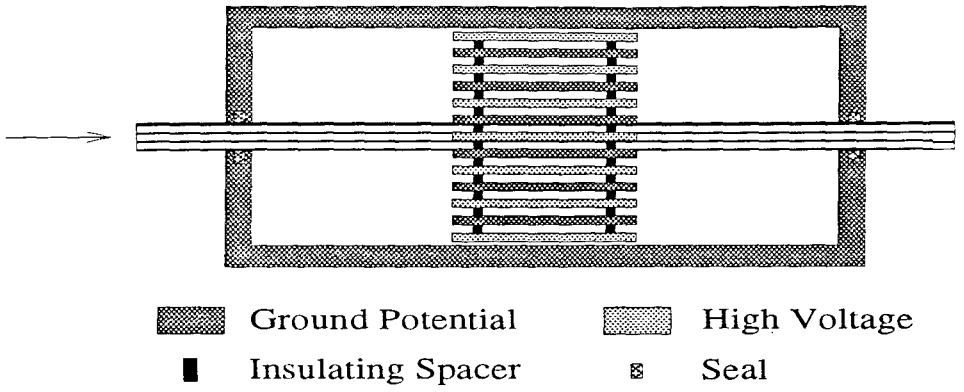

Figure 4.3: A mixed-mode ER device.

4.1.4 Control of Visco-elastic Properties

In another class of applications, ER material is sandwiched between two flexible conducting layers [12, 65, 101, 274]. In this composite beam, the ER material transfers shear stress between the flexible electrodes. The ER material is meant to behave as a visco-elastic solid when a high potential is applied across the electrodes. The ER material exhibits changes in stiffness and damping with very short response times. The natural frequencies of such beams can change by as much as 25% and the damping ratios can change by as much as 45% [101]. Adjustable stiffness and damping distributed throughout a structure can be used for control of low level vibrations in mechanical engineering structures [186]. An experimental, simply supported beam of the described composite sandwich configuration had natural frequencies of 21, 70, and 140 Hz without an electric field and 60, 110, and 190 Hz at 2.5 kV/mm [65]. Damping ratios in the first three modes changed from 0.032, 0.035, and 0.045 to 0.05, 0.09, and 0.11. Peaks of the transfer function at 2.5 kV/mm occurred near the valleys of the transfer function at $E = 0$ [65]. Low electric fields increased the damping only. At higher electric fields, the stiffness (and natural frequencies) increased [242, 243]. Some low-strain experiments have shown that the damping ratio,

$(c/(2\sqrt{km}))$, is maximum at intermediate electric fields [243]. The ability to modify structural behavior to this extent implies that many modes can be simultaneously (but not independently) controlled using ER composite structures. While adjustable material stiffness and damping properties can be exploited in a variety of control applications, the visco-elastic behavior of ER materials is not as well understood as the yielding behavior [43, 45].

4.1.5 Wear and Durability Properties of ER Materials

The abrasiveness of ER suspensions in damping devices is an important issue. Conductive material worn from the surface of ER devices will enter the suspension and can lead to arcing discharges between the electrodes. Some ER fluids are more abrasive than others [256]. A suspension of 12 micron diameter hydrated lithium polymethacrylate salts was compared to a commercial petroleum lubricant [176]. Tests were designed to simulate the wear conditions in hydraulic power devices and pumps. Inspection of the specimens after pin-on-disc and disc-on-disc tests revealed abrasion, extrusion, and delamination of the surfaces. Wear with the ER fluid as a lubricant was 10,000 times greater than the wear with the petroleum lubricants. Surprisingly, removing the particles from the ER fluid gave similar results [176], implying that the wear depended on the base fluid. Wear properties will probably need to be improved before ER materials can be pumped for extensive periods.

Methods for capturing metallic particles in a hydraulic circuit of ER materials (using magnetic sieves) have been proposed [46, 237, 256].

4.2 Vibration Actuators

In principal, ER devices can be used where ever transduction from an electrical signal to a mechanical action is required [43]. Vibration actuation was one of the

earliest applications of ER materials. The ER vibration actuator [220, 254, 255] is illustrated in Figure 4.4. ER fluid is continuously circulated through the vibration

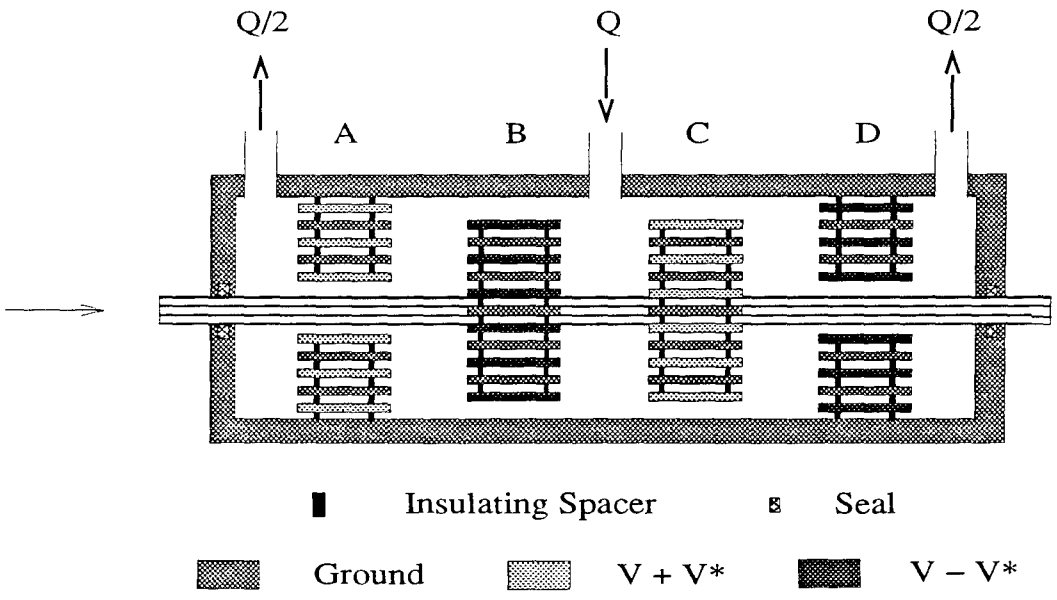

Figure 4.4: A bi-directional ER vibration actuator.

actuator by an external pump, not shown in Figure 4.4. ER fluid flows in through a port in the middle of the actuator and exits through ports at the ends of the actuator, as shown. Valves A and D are connected to the case and valves B and C are connected to the shaft. Valves A and C are at the same voltage potential, $\mathcal{E} + \mathcal{E}^*(t)$, and valves B and D are at another potential $\mathcal{E} - \mathcal{E}^*(t)$, where $\mathcal{E}$ is a bias voltage and $\mathcal{E}^*$ is the variable control voltage. When $\mathcal{E}^* > 0$ flow is restrained in valves A and C. The hydrostatic fluid pressure therefore increases in the space between valves A and C, and the shaft moves to the right. The balanced voltage on the valves compensates for the non-linear relationship between electric field and yield stress [220]. This device was a context for the first analysis of steady ER flow [220]. An actuator/pump system weighing 155 pounds had a dynamic capacity of 2200 pounds at 1000 Hz. The largest forces (pressure drops of 400 psi) were produced

with the smallest flow rates (down to 10 gallons/minute) [255]. The fast response times and lack of moving parts produced devices with a 1 kHz band-width and a dynamic range of 50 or more.

Later versions of this actuator implemented ER valves in a Wheatstone bridge external to the actuator [36, 178, 179, 246]. External valves simplified manufacture of the actuator [246]. Lou analyzed the hydraulics of an ER position control system using a Wheatstone bridge valve configuration [178]. An ER bridge was found to be most efficient when the pump supply pressure was no greater than twice the pressure required to yield the ER material at the full electric field. The ER valves should be designed for operation as close as possible to the yield pressure. Naturally, designing with high yield strength fluids will result in smaller or more powerful actuators. External valves led to external losses of 20% of the pump pressure and a 5% asymmetry in the resistances of the valves. Additional design issues identified in these studies [179] were the need for:

- electrical isolation materials that do not break-down in the presence of prolonged arcing (nylon and teflon were not satisfactory),

- translational dynamic seals that are resistant to fine particulates in the ER fluid, and

- high pressure diaphragm pumps which can supply steady pressure and flow,

High frequency, high force and low displacement applications appear to be the most promising for ER vibration actuators [246].

4.3 Engine Mounts

Tunable isolation interface devices, such as engine mounts, are a promising automotive application of ER materials. ER engine mounts [79, 81, 83, 217, 279, 280] use valves to regulate the flow of ER material between two compliant chambers. Because the volume flow rate through the valves is low, ER engine mounts have controllable damping and stiffness properties. The valves in these mounts can be operated in unison [217, 280] or independently [79, 83]. Independent operation of the valves allows for a more continuous range of adjustable stiffness, damping, and especially, fluid-inertia [82, 79].

Some mount designs take advantage of variable fluid inertia properties. Closing valves reduces the dynamic mass flowing between the compliant chambers. The valves in these mount designs are intended to stop any flow through associated fluid pathways, thereby eliminating the mass of the fluid in those pathways from the total fluid inertia. The valves in other mount designs are meant to act as variable dampers to supply damping forces proportional to the absolute velocity of one terminal of the mount (when possible). In a fluid inertia mount, as illustrated in figure 4.5, a dynamic

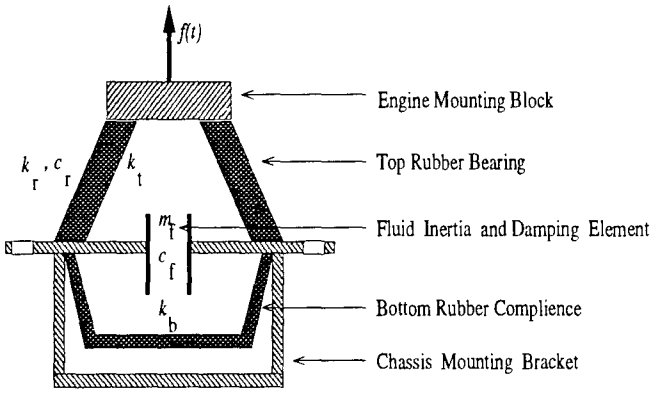

Figure 4.5: An ER fluid-inertia engine mount.

force, $f(t)$, from the engine is transferred to the chassis

1. directly, through the deformation and the deformation rate of the rubber bearing, k_r and c_r,

2. through fluid inertia, m_f, forces transferred through the mount to the bottom rubber compliance, k_b, and

3. through viscous stresses in the fluid, c_f.

The dynamic stiffness can be selected to be about 50% of the static stiffness, thereby attenuating the transmission of sinusoidal forces from the engine to the auto frame. The free body diagram of this mount is illustrated in Figure 4.6.

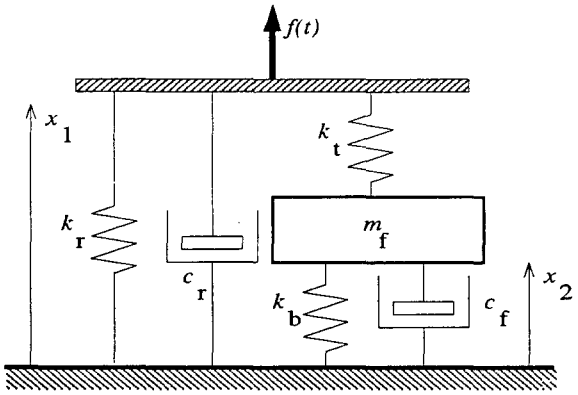

Figure 4.6: Free body digram of an ER fluid-inertia engine mount.

Duclos [79] determined the complex dynamic stiffness, f/x_1, of the system illustrated in Figure 4.6

$$\frac{f}{x_1} = k_r + c_r j\omega + \frac{k_t(-m_f\omega^2 + c_f j\omega + k_b)}{-m_f\omega^2 + c_f j\omega + k_b + k_t}, \tag{4.1}$$

where the variables are defined in Figure 4.6, and $j = \sqrt{-1}$. The magnitude of the dynamic stiffness equation (4.1) has a global minimum at [79]

$$\omega^2 \approx \frac{1}{m_f}\left(k_b + \frac{k_r}{1 + k_r/k_t}\right). \tag{4.2}$$

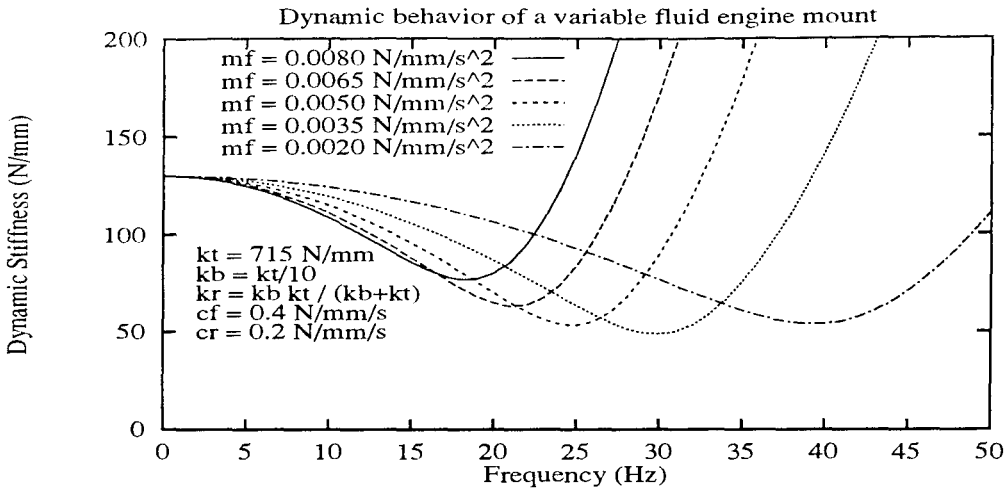

Figure 4.7: Adjustable dynamic stiffness of a fluid inertia engine mount.

The variation of the dynamic stiffness with frequency and dynamic mass is illustrated in Figure 4.7. By finely tuning the dynamic mass, the mount's response to sinusoidal forces, such as an engine unbalance, can be reduced by roughly 50% [79] or more [217] over typical engine operating ranges (1000 rpm – 3000 rpm). Patented designs for fluid-inertia engine mounts [81, 83] describe long inertia passageways communicating between two compliant, ER fluid-filled chambers. The dynamic stiffness is decreased over relatively narrow frequency *notches* and increases significantly at frequencies higher than the notch frequency (4.2) [65]. The passageways have different diameters, allowing for fine-tuning of the notch frequency. Miniature parallel wall ER valves at one end of each passage can independently block the flow in its passage, and eliminate the associated fluid from the dynamic inertia. To reduce the zero-voltage resistance of the valves, the flow area of the valves is greater than the flow area of the passageways [65]. A pre-programmed table maps a measured excitation frequency to the the valve configuration which maximizes the mount's compliance at that frequency [79].

If the excitation contains higher frequencies, the behavior of adaptable fluid inertia mounts is less than ideal [279]. Fluid-inertia engine mounts can amplify vibrations

by a factor of 30 at frequencies higher than the notch frequency. Adding a compliant membrane between the fluid chambers can broaden the notch [279].

Other implementations of ER fluids in semi-active engine mounts call for adjustable damping forces [199, 217, 280]. Because inertia pathways are eliminated, these mounts can be smaller than variable fluid-inertia mounts. In variable damping mounts, the electric field is varied continuously to produce a force in phase with the absolute velocity of one of the terminals of the mount [199, 279] (when possible). This control method is called *pseudo sky-hook damping* [143]. The transmissibility of engine mounts implementing the pseudo-skyhook damping rule is uniformly less than the transmissibility of a mount with high static damping [280].

When the ER valves stop flow entirely, the mount becomes much stiffer, and the fundamental frequency of the isolated system can change by a factor of 2 [199]. ER-filled engine mounts have been shown to be effective in lowering the transmissibility over a temperature range of 0 °C to 100 °C and perform as well as a tuned liquid mount without transmitting high frequencies [217]. Given constraints on the size and geometry of ER engine mounts, they are feasible with currently available fluids (τ_y = 1.5 kPa at 4 kV/mm and η = 0.2 Pa-s) [122].

4.4 Vehicle Suspensions

Because the damping rate of oil-filled shock absorbers decreases with temperature and use, they become ineffective in periods of high demand. In this context, a controllable shock absorber can provide the required damping in a variety of operating conditions [120].

In a comparison of flow mode, shear mode, and mixed mode dampers, Lou and Duclos independently determined that mixed mode dampers are more compact than

flow mode or shear mode dampers with comparable performance specifications [80, 180]. The zero-field forces are larger in a mixed mode damper than in a shear mode damper [180].

Bridgestone Corp. holds a patent on a variety of ER vehicle suspension devices [208]. These devices have a telescoping geometry. The two telescoping parts are connected by a compliant rubber membrane, which also contains the ER fluid. ER fluid commutes between the telescoping sections through an ER valve. Different versions of the damper include mechanisms which can confine the ER fluid to the valve region and isolate it from less expensive hydraulic fluid in the rest of the damper. The control decision is based on the pseudo-sky hook damping rule. The design of these dampers is much simpler than the mechanical hardware specified in other patented designs [78]. ER-based vehicle suspensions can be programmed to have arbitrary force-velocity profiles and respond much faster than variable orifice dampers [218, 219, 238]. The velocity-force relationship can be tailored to the road or driving conditions [8].

Linear motion can be translated into rotational motion if ball screws and thrust bearings are incorporated into the damper design. Damping of rotational motion is easier to accomplish using ER devices. The fluid will shear, but not flow, between the electrodes. In shear mode devices, the zero-field damping forces are lower, less ER fluid is required, sealing requirements are less demanding, no fluid accumulators are required, and observed yield stresses are higher. The penalties to the ball-screw approach are the additional friction of the ball-screw and thrust bearing. Existing ball screws and thrust bearings are, nevertheless, highly developed and efficient. A damper based on this approach has recently been built and tested [66]. The dynamic range of the tested device was 4. Forces were larger than a theoretical

approach would predict. These larger forces were attributable to friction in the thrust-bearings. While the dynamic range of this device was not exceptionally large, other mechanical features make it a promising design.

A semi-active automobile suspension system using magneto-rheological (MR) fluids has been implemented in full scale [223, 224]. Magneto-rheological fluids require larger currents and therefore more power than ER fluids, albeit at lower voltages. Yield stresses of MR fluids are considerably higher than those of ER fluids, but their response times are much slower. Furthermore, the electro-magnets required for their activation are much larger than the electrodes of an ER device. Nevertheless, the performance of this full-scale implementation was notable. The vehicle response to low-frequency disturbances, such as evasive maneuvers, was attenuated by 50 percent. High frequency disturbances, such as wheel-hop resonances were not significantly attenuated [223, 224]. A similar system using ER materials has been tested in simulation [197].

Given constraints on the size and geometry of ER suspension shock absorbers for automobiles, fluids with $\tau_y = 4$ kPa at 4 kV/mm and $\eta = 0.1$ Pa s are required [122].

In addition to automotive applications, fast-acting ER shock absorbers can be used to cushion the initial shock of a landing aircraft and provide vibration isolation during taxi and take-off operations [26]. A proposed damping control method attempts to achieve a constant, and uniformly minimum, deceleration during the impact of landing. Near-term ER fluids should be able to satisfy the requirements for a semi-active aircraft landing strut [26].

ER materials are also under consideration for the secondary suspension of high-speed magnetically levitated trains [120, 216]. Such a high performance suspension will allow these trains to use several existing rail right-of-ways without the need to

reduce speeds when rounding sharp turns.

4.5 Clutches

ER clutches can be used in the speed control of air conditioners, alternators, brakes, pumps [122], and automated manufacturing machines [238]. Fluid flow in a clutch is pure shear flow, and device types can be of the parallel plate or concentric cylinder geometry. The flow of Bingham fluids in a rotating parallel plate geometry has been described by Yoshimura and Prud'homme [308]. Increasing the dynamic range of clutches requires increasing the gap size and the volume of fluid [47]. However, the volume of ER material in a clutch is far less than the volume required for other types of devices. As in flow-mode devices, the maximum gap size is limited by the maximum available voltage (usually 15 kV). Carlson showed that the gap to radius ratio (shape) is governed by η/τ_y and the volume of fluid is governed by η/τ_y^2. A 10-plate clutch for a precision motorized screw-driver was designed to have a dynamic range of 50 at 60 rpm [47]. The dynamic range decreases with the rotational speed of the screw-driver.

Given constraints on the size, geometry, and torque levels of automotive clutches, fluids with τ_y=15 kPa at 4 kV/mm are required [122]. ER clutches for smaller, high-precision instruments are closer at hand [47] and a clutch to control wire-tension to within 0.5 percent has been built and tested [46, 165]. Precision control of wire tension during spool winding operations is essential for the very fine wires used in integrated circuit applications [120].

4.6 High Voltage Control

Fast acting ER devices require fast-acting high voltage control electronics. High power MOSFETs[2] can switch 1 kV at 100 kHz [49, 256]. Thus, power MOSFETs can be applied only to ER devices with relatively narrow gaps. ER materials which require 3 kV/mm in devices which have gaps of 1 mm or greater can not be controlled by these transistors. They may, however, have applications in some automotive applications. The voltage required to operate an ER engine mount (6 kV at 1.2 mA) can be supplied by a 12 volt battery at 800 mA and a dc to dc converter [79]. Arcing discharges in ER materials can lead to the electrical break-down of the fluid and failure of the power supply. In applications where the supply of electrical power is limited, switching the voltage off at 50 Hz or more can reduce the electrical power with little effect on the average yield stress. Arcing discharges are also less likely to occur when the electric field is pulsed [264].

4.7 Summary

ER devices can be categorized as shear mode, flow mode, or mixed mode according to the flow velocity profile within the device. The behavior of these different configurations is qualitatively different. For damping rectilinear motions, mixed mode devices, with a rectangular cross section, are most efficient.

ER devices have been designed for use as vibration actuators, tunable engine mounts, controllable vehicle shock absorbers, and machinery clutches. Many of these devices have been built and tested. ER devices feature large dynamic range, fast response times, and minimal power requirements for operation.

[2] A MOSFET is a type of transistor which can regulate larger amounts of power than bi-polar or JFET transistors.

Table 4.1: A comparison of ER devices and properties.

Device Type	Capacity	Dynamic Range/ Band-width	τ_y (kPa)	η (Pa-s)	Ref.
Actuator	35 kN	/ 3 Hz	5.0	0.30	[36]
Actuator	10 kN	17 / 1 kHz			[255]
Actuator	0.17 MPa	4 / 100 Hz	0.6	0.04	[179]
Shear	9 N	9 /		0.10	[265]
Engine Mount	2 kN/mm	30 / 100 Hz			[79]
Engine Mount		14 / 300 Hz		0.13	[279]
Engine Mount		11 / 3 Hz			[217]
Damper	400 N	6	1.3	0.10	[66]
Damper	14 N			0.10	[263]
Damping Strut	2 kN	4 / 150 Hz	5.0	0.30	[36]
Valves	5 MPa	33 / 300 Hz	5.0	0.30	[40]
Torsion Damper	1.5 kN m	4 / 2 Hz	5.0	0.30	[36]
Valve	0.18 MPa	11/350 Hz	0.4	0.14	[246]
Valve		12 / 20 Hz	3.0	0.06	[35]

An overview of the wide range of published performance specifications of a variety of ER devices is given in Table 4.1.

CHAPTER V

MODELING OF ER FLUID DAMPERS

An accurate model for the behavior of ER dampers is useful for simulation studies of the damper behavior as well as for structural control simulations. By modeling their behavior, one can also gain insight into the nature of ER devices. The solution of the Bingham flow equations, as outlined in Appendix B, provides an approximate model which is sufficiently accurate for design purposes [40, 41, 67, 292]. Some control applications require known input-output relations for the actuators providing the control forces. In this case, an accurate model for the device can be derived from experiments on the device itself. Bingham model parameters (yield stress and viscosity, or friction force and damping rate) can be estimated by fitting a model of the actuator system to the experimental data. One attempt at estimating τ_y and η from pressure response records measured from sinusoidally actuated damper motions is outlined in Appendix B. This method had mixed success. Another method, employing a recursive least squares approach, converged on model parameters, but has other draw-backs, as described in the following sections.

The objective of the modeling effort should be linked to the experiments conducted to obtain the model. For instance, Couette flow data is much easier to analyze than Poiseuille flow data, by virtue of the constant stress profile in pure shear flow.

So for obtaining ER material properties, Couette or other shear flow experiments are commonly performed. If the complexity of the damper's behavior can be satisfactorily modeled by the Bingham flow equations, then the yield stress and viscosity from Couette flow measurements can be inserted into (3.22). Certain important aspects of ER behavior are not described by the Bingham equations alone: the response to transient electric fields, and the response to un-steady flow. Analytic models have succeeded in capturing the behavior in such transients only under very controlled experimental conditions [298]. Behavior during general operating conditions can be significantly more complex. Modeling of such behavior can be more accurate if a more generalized (non-parametric or polynomial) description of the damper is employed. The distinction between parametric and non-parametric models pertains to the physical significance of the parameters in the model. As used in this study, *parametric* models denote models whose parameters are physically meaningful quantities, such as τ_y and η. *Non-parametric* models are models in which the parameters (such as polynomial coefficients) have little or no bearing on any physically meaningful quantity.

5.1 Parametric Models

Stanway [259, 260] fit an ER damper model based on Bingham-like parameters (Coulomb friction and damping rate) to data obtained from an ER dampened SDOF system. The damper was of the mixed-mode design. Stanway cast the equations of motion, including the ER damper, into a state-space form and included the two unknown parameters as part of the state vector. A recursive least squares method was used to estimate the parameters. Data sets were collected at different, constant values of E. The performance of the method using data with time-varying E was not

assessed. Recursive least squares estimation methods are more successful when estimating constant, or slowly varying, parameters. Estimating time-varying parameters is significantly more difficult.

The estimated Coulomb friction coefficient did not demonstrate its expected quadratic relation with E, but remained relatively constant with increasing E [259, 260]. The damping coefficient, on the other hand, increased dramatically with E. Parameters estimated from data collected under high electric fields were not considered reliable [260].

A similar approach was applied to the estimation of n^{th} power damping coefficients, in which the damping force is $c|\dot{x}|^n \text{sgn}\dot{x}$ [203, 261]. The unknown parameters are the coefficient c and the exponent n. In simulation studies, a recursive least squares approach converged quickly to the known parameter values. When applied to experimental data, this method was again more successful at low electric fields in estimating parameters which could accurately model the data. The n^{th} power damping rule cannot simulate the friction-like stick slip behavior evident in the data at higher electric fields [260].

5.2 Non-Parametric Models

A scalar function of many variables can be approximated, in a least-squares sense, by a series expansion of orthogonal polynomials. The coefficients of the expansion can be evaluated explicitly, by virtue of the orthogonality properties of the polynomials. Many orthogonal polynomials arise from the solutions to ordinary differential equations. Their orthogonality properties are specified over infinite, semi-infinite, or closed domains, and with respect to particular weighting functions. Of the set polynomials mutually orthogonal in a closed domain, Chebyshev, Legendre, and

Forsythe [98, 147] polynomials were considered for curve-fitting applications in this study.[1] Chebyshev approximation of non-linear dynamical systems, including ER devices, was first carried out by Masri *et al.* [87, 189]. Masri formulated an approach in which the system non-linearities were a function of displacement and velocity. This method is extended in the next sections to describe the non-linearities as a function of displacement, velocity, and electric field. An inverse model is also presented.

5.2.1 Chebyshev Polynomial Approximation

Chebyshev polynomials,

$$T_n(x) = \cos(n \arccos(x)), \tag{5.1}$$

illustrated in Figure 5.1, can be evaluated recursively:

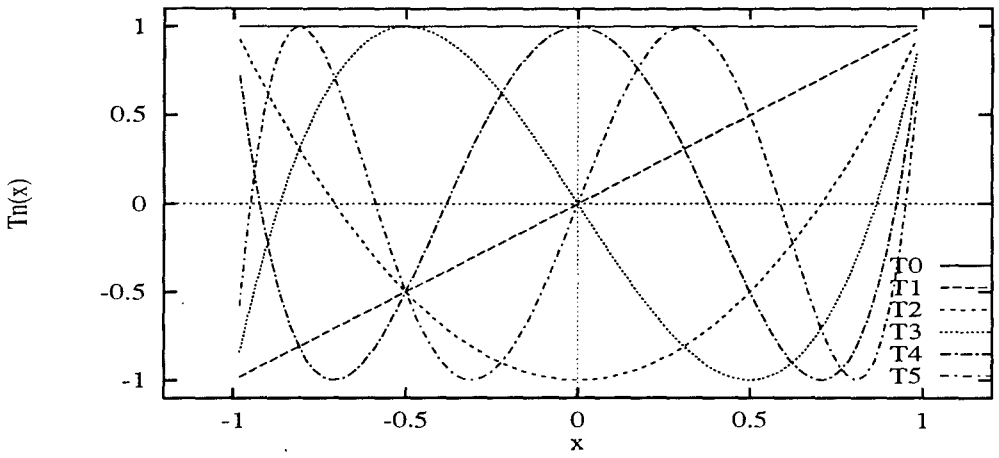

Figure 5.1: The first six Chebyshev polynomials $T_n(x) = \cos(n \arccos(x))$

[1] Other non-parametric identification methods, such as Padé approximation and artificial neural networks were also considered.

$$\begin{aligned} T_0(x) &= 1 \\ T_1(x) &= x \\ &\vdots \\ T_{n+1}(x) &= 2xT_n(x) - T_{n-1}(x) \quad n \geq 1 \end{aligned} \tag{5.2}$$

Chebyshev polynomials are mutually orthogonal with respect to the weight $1/\sqrt{1-x^2}$ in the interval [-1,1].

$$\int_{-1}^{1} \frac{T_i(x)T_j(x)}{\sqrt{1-x^2}}dx = \begin{cases} 0 & i \neq j \\ \pi/2 & i = j \neq 0 \\ \pi & i = j = 0 \end{cases} \tag{5.3}$$

The numerical evaluation of this integral suffers from inaccuracies when x is close to -1 or 1. The orthogonality condition for discrete Chebyshev polynomials is given by the expression

$$\sum_{k=1}^{M} T_i(x_k)T_j(x_k) = \begin{cases} 0 & i \neq j \\ M/2 & i = j \neq 0 \\ M & i = j = 0 \end{cases} \tag{5.4}$$

where x_k $(k = 1, \ldots, M)$ are the zeros of $T_M(x)$ and lie in the interval [-1,1]. The degree of $T_M(x)$ must be greater than or equal to i and j. The roots of $T_M(x)$ are

$$x_k = \cos\left(\frac{\pi}{M}\left(k - \frac{1}{2}\right)\right) \qquad k = 1, 2, ..., M \tag{5.5}$$

Figure 5.2 illustrates the zeros of a two-dimensional Chebyshev polynomial. Because the zeros of $T_M(x)$ are concentrated at the boundary of the domain, the curve-fit is often more accurate there. To take advantage of the orthogonality properties of the Chebyshev polynomials, in least-squares approximation of data, the data needs to be interpolated to the zeros of a high-order Chebyshev polynomial. Interpolating the data to the roots of $T_M(x)$ has the same effect as applying the weight $1/\sqrt{1-x^2}$ to uniformly distributed data.

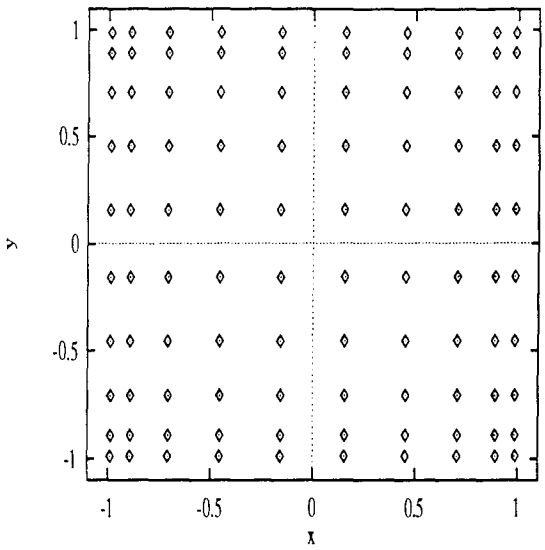

Figure 5.2: Zeros of the product of two 10th degree Chebyshev polynomials, $T_{10}(x)T_{10}(y)$.

In three dimensions, the Chebyshev approximation to $f(x, y, z)$ is given by

$$\hat{f}(x, y, z) = \sum_{i,j,k=0}^{I,J,K} C_{ijk} T_i(x') T_j(y') T_k(z') \tag{5.6}$$

where x' and y' z' indicate a mapping of x, y, and z to interval [-1,1]. For example, $x' = (2x - x_{\max} - x_{\min})/(x_{\max} - x_{\min})$. The evaluation of the coefficients C_{ijk} follows directly from Fourier expansions,

$$C_{ijk} = \frac{1}{||T_i||^2 ||T_j||^2 ||T_k||^2} \sum_{p,q,r=1}^{P,Q,R} f(x''_p, y''_q, z''_r) T_i(x_p) T_j(y_q) T_k(z_r), \tag{5.7}$$

where $i, j, k = 0, \ldots, I, J, K$; $P, Q, R \geq I, J, K$; and x_p, y_q, z_r are the roots of T_P, T_Q, and T_R. The coefficients C_{ijk} are conveniently expressed as a third order matrix. The variables x''_p, y''_q and z''_r represent a mapping of x_p, y_q and z_r from [-1,1] to $[x_{\min}, x_{\max}]$, $[y_{\min}, y_{\max}]$, and $[z_{\min}, z_{\max}]$. For example, $x''_p = [x_p(x_{\max} - x_{\min}) + (x_{\max} + x_{\min})]/2$. Combining (5.1),(5.4),(5.5), and (5.7) results in simple equations for the coefficients

C_{ijk} [226]

$$C_{ijk} = \frac{1}{||T_i||^2||T_j||^2||T_k||^2} \sum_{p,q,r=1}^{P,Q,R} f(x''_p, y''_q, z''_r) \times \cos\left(\frac{i\pi}{P}\left(p-\frac{1}{2}\right)\right)\cos\left(\frac{j\pi}{Q}\left(q-\frac{1}{2}\right)\right)\cos\left(\frac{k\pi}{R}\left(r-\frac{1}{2}\right)\right) \quad (5.8)$$

If $f(x,y,z)$ is a continuously evaluable function, (5.8) is a closed form solution for the Chebyshev coefficients. If, on the other hand, $f(x,y,z)$ is available only at discrete values of the independent variables, an interpolation method is required to obtain $f(x''_p, y''_q, z''_r)$. The interpolation routine used in the current study is a three-dimensional low-pass filter that computes a weighted sum of all the data points based on the L_n norm. Given a parametrically tabulated function, $f_t(x_t, y_t, z_t)$,$(t = 1,\ldots,T)$, an interpolated value of f at (x^*, y^*, z^*), can be calculated using

$$f(x^*,y^*,z^*) = \frac{\sum_{t=1}^{T} f_t(x_t,y_t,z_t)[(x^*-x_t)^n + (y^*-y_t)^n + (z^*-z_t)^n]^{-1}}{\sum_{t=1}^{T}[(x^*-x_t)^n + (y^*-y_t)^n + (z^*-z_t)^n]^{-1}} \quad (5.9)$$

The exponent n must be a positive even number. Smaller values of n result in smoother interpolated functions. A value of n=8 was chosen for the current study. Only a cursory study of the effect of n on the goodness of fit was undertaken. The value of 8 was chosen to give the best resolution with the least computational effort.

An attraction of Chebyshev approximation can be appreciated by noting that all the extreme values of $T_M(x)$ are either +1 or -1, and that adjacent extrema are of opposite sign. If the coefficients C_j of a Chebyshev approximation decrease rapidly with increasing j, then the error associated with an J^{th} degree approximation is dominated by $T_{J+1}(x)$, which also has equal extrema. The faster the C_j's decrease with j, the closer the Chebyshev approximation approaches a *minimax* approximation, in which the approximation is equally accurate over all regions of the domain. This minimax property of Chebyshev curve-fits is noted in Appendix C.

5.2.2 Modeling ER Devices for Simulation and Control

In modeling and controlling ER dampers, two non-parametric models are useful. In performing characterization experiments on an ER device, the motion of the device (displacement, x, and velocity, $\dot{x}$) the voltage or electric field, E, and the fluid pressure gradient or force, f, can be measured easily. Given these measurements, a function relating the force to the other three measurements,

$$\hat{f}(x, \dot{x}, E) = \sum_{i,j,k=0}^{N} C_{ijk} T_i(x') T_j(\dot{x}') T_k(E'), \tag{5.10}$$

can be used to simulate the behavior of the member. If experimental results are repeatable, then a model of the form (5.10) describes the behavior of the device in a variety of operating conditions.

Another useful relation can be deduced from experimental measurements. Given the motion of the device and the desired force, the voltage or electric field required to produce the force can be evaluated from an expression of the form

$$\hat{E}(x, \dot{x}, |f|) = \sum_{i,j,k=0}^{N} C_{ijk} T_i(x') T_j(\dot{x}') T_k(f'). \tag{5.11}$$

Equation (5.11) can be used to linearize the damper behavior for control purposes. Two complications arise in finding the coefficients C_{ijk} in (5.11). First, the independent variables $(x, \dot{x}, f)$ do not fill the three-dimensional domain. The unconditional dissipation of the damper requires that the force and the velocity have the same sign. So there is no data in regions of the domain where $\dot{x}f < 0$. Curve-fitting methods require data over the entire domain of the curve-fit. Because the sign of the force is determined by the sign of the velocity, only the absolute value of the force need be specified as an independent variable. So doing, $|f|_{\min} = 0$ maps to $f' = -1$, which is on the edge of the domain. A second complication arises in evaluating (5.11) when

the requested force, $|f|$, is out of range. The absolute value of the available forces is bounded and depends on the device motion. To over-come this difficulty, if the requested force, $|f|$, is less than its minimum value, then $E = 0$ is specified, and if $|f|$ is greater than its largest possible value then a maximum E is specified. The limiting values of $|f|$ at any device motion can be evaluated from (5.10). In this sense, a model for control (5.11) requires a model for simulation (5.10).

5.2.3 Other Polynomial Bases

Similar approximations can be derived with other polynomial bases. Legendre polynomials are mutually orthogonal in the interval [-1,1] with respect to the unit weighting function. Forsythe polynomials can be recursively defined to be orthogonal with respect to any arbitrary weighting function [98, 147]. This property is especially useful in fitting complex data (such as frequency response functions) with complex rational polynomials [228, 229]. The benefit of using an arbitrary weight is that any region of the domain may be emphasized in evaluating the overall accuracy of the curve-fit. The cost of using data-specific weighting functions is that the recursive definition of the polynomials is then also data-specific. The polynomial coefficients as well as the weighting data are required to specify the non-parametric model. Calculation of the polynomials is also somewhat slower in this case. However, it is intuitive to try polynomials which are orthogonal with respect to the unit weighting function, such as the Legendre polynomials. A true minimax approximation using Forsythe polynomials may be found recursively by specifying the error function of one curve-fit to be the weight function of the next curve-fit.

5.3 Summary

Fitting Bingham-like parameters to simulated and experimental data from an ER fluid damper have not resulted in parameters representative of the device behavior, especially for large values of the electric field [259, 260, 261].

Curve-fitting force as a function of displacement and velocity has successfully modeled a number of non-linear elements, including ER dampers [87, 189]. This chapter presents an extension and analysis of a method to curve-fitting in a three-dimensional domain, which includes the electric field.

Using the experimental data described in the next chapter, curve-fitting data with Chebyshev polynomials results in good approximations to the device's behavior.

CHAPTER VI

DESIGN, TESTING, AND MODELING OF MIXED-MODE ER FLUID DAMPERS

Two series of tests were conducted. One series focused on evaluating the approximations described in Chapter III and Appendix B, and were conducted on a small scale. The purpose of the other series of tests was to gain experience with the design, construction, and behavior of ER dampers for very large scale structures. Supplemental damping was identified as an economical and efficient retrofit method for the Golden Gate Bridge [149, 150]. Parameter studies for dampers to be placed between the roadway truss and the towers led to a desired device damping rate of 12.5 kip/in/sec (4.4 kN/cm/sec). It was hoped that a convincing demonstration of the benefits of using an ER damper in a semi-active control strategy would make them an attractive alternative to using passive friction or viscous dampers.

Most ER devices have multiple parallel ducts, through which the ER fluid flows, and across which an electric field is applied. This chapter begins by extending the analysis of steady Bingham flow through a single gap, to an analysis of Bingham flow through multiple gaps, not necessarily of the same size.

The subsequent two sections describe the small-scale and large-scale experiments. The device design, materials used, sensors, testing procedure, experimental data and

data analysis are presented in these sections.

6.1 Device Design and Analysis

The rectangular duct, mixed-mode, device type was chosen as the the design configuration for both test series. Although sealing requirements are easier to satisfy in cylindrical devices, rectangular devices are easier to analyze and construct. As described in Chapter IV, as the fixed plates of a mixed-mode damper translate rectilinearly through the fluid, they pump fluid from one side of the ER damper, through the gaps between the plates, to the chamber on the other side of the plates. Refer to Figure 4.3. The mean flow rate of the fluid through the gaps can be calculated from continuity conditions and the device geometry. Assuming incompressible flow, the mean flow velocity, V_f, through the $N+1$ gaps between N plates and the case is

$$V_f = \left(1 + \frac{N}{N+1}\frac{t}{h}\right) U, \tag{6.1}$$

where h is the thickness of the gap, t is the thickness of the plates, and U is the device velocity. The velocity of the outer-most plates with respect to the case is the same as the velocity across the terminals of the device. Balancing shear and pressure forces on the plates in the device leads to the force, f, as a function of the pressure difference between the two chambers, $p'l$,

$$f = Np'l(t+h)b, \tag{6.2}$$

where l and b are the length and the width of the plates, respectively. This expression assumes equal flow profiles in *all* the gaps. As will be shown shortly, this assumption does not lead to large errors in most cases. The pressure gradient, p', can be calculated by substituting $V_f bh$ for Q in (3.21).

Relaxing the equal flow assumption requires significantly more complicated calculations, and requires an assumption regarding material behavior, such as the Bingham assumption. An example of a procedure for calculating the member force, in this case, can be summarized as follows:

1. Assume that all the gaps between the plates are of equal size h_i, and that the gaps between the plates and the case have a gap h_o, not necessarily the same as h_i. Furthermore, assume that the volumetric flow rate, Q_i, through each gap h_i is the same, and the volumetric flow rate through each gap h_o is the same, Q_o. Wider outer gaps often result from requiring adequate clearance with a margin of safety for alignment errors.

2. The pressure gradient, p', is the same along each of the gaps h_i and h_o. Insert Q_i and h_i into (3.21) and insert Q_o and h_o into (3.22).[1] Solve (3.21) and (3.22) for p' individually. These two equations for p' are a system of two nonlinear equations for Q_i, Q_o, and p'. The pressure gradient, p', can be eliminated by setting the two equations for p' equal to each other and solving for Q_i as a function of Q_o. The third required relation is the volume conservation equation, and is a generalization of (6.1).

$$(N-1)Q_\mathrm{i} + 2Q_\mathrm{o} = b[Nt + (N-1)h_\mathrm{i} + 2h_\mathrm{o}]U. \tag{6.3}$$

A closed form solution to this non-linear system of equations may not exist, and numerical methods may be necessary. For Newtonian fluids, closed form expressions for Q_i and Q_o are:

$$Q_\mathrm{i} = V_\mathrm{f} b\,[(N-1)h_\mathrm{i} + 2h_\mathrm{o}] \left[N - 1 + 2\left(\frac{h_\mathrm{o}}{h_\mathrm{i}}\right)^3 \right]^{-1} \tag{6.4}$$

[1]The Bingham assumption is implicit in these equations.

and

$$Q_o = \left(\frac{h_o}{h_i}\right)^3 Q_i \tag{6.5}$$

3. With a solution for Q_o or Q_i in hand, the pressure gradient, p', is also calculated.

4. The next step is to calculate the fluid shear stress on the case, τ_w. A dimensionless wall stress,

$$T_w = \frac{bh_o^2\tau_w}{12Q_o\eta} \tag{6.6}$$

can be calculated from the dimensionless pressure gradient and the dimensionless yield stress in the outer gap

$$T_w = P\left(\frac{1}{2} - \frac{V}{6A}\right). \tag{6.7}$$

This relation is the non-dimensional expression for the linear variation of shear stress in the gap and follows from the definitions of the non-dimensional variables, P, T, V, and A. Figure 6.1 illustrates the importance of the correction $\frac{V}{6A}$ in (6.7). For dimensionless yield stresses greater than 10 or dimensionless wall velocities less than 0.1, the correction to the wall stress due to an asymmetric flow profile is insignificant. Variations in gap size will influence p' and f much more than the effects of a moving wall since the flow in the outer gap depends roughly on $(h_o/h_i)^3$.

5. Given τ_w from (6.7) and p' from the equations for Q_i and Q_o, the member force can finally be calculated.

$$F = p'l(Nt + (N-1)h_i + 2h_o)b - 2\tau_w lb. \tag{6.8}$$

Note that for values of T and V for which $\frac{V}{6A}$ is small, and $h_i/h_o \approx 1$, (6.8) is closely approximated by (6.2). Since (6.2) does not depend on assumed material

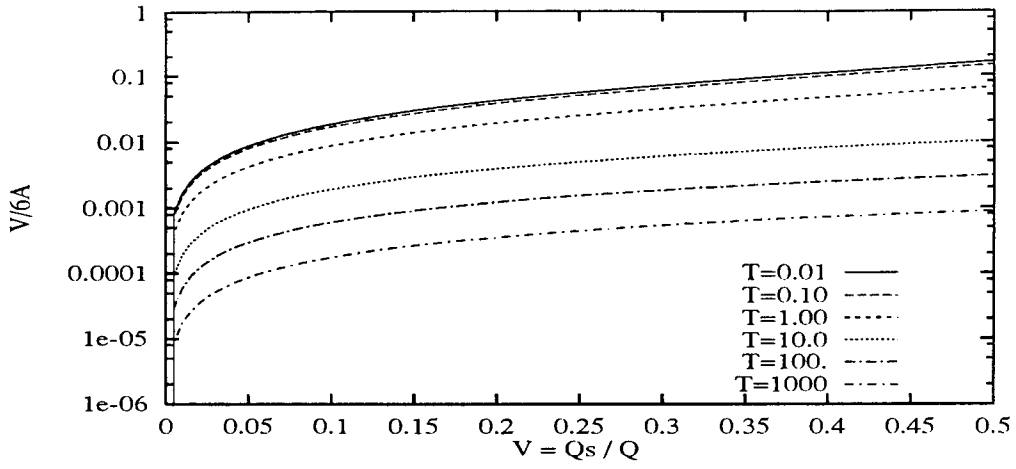

Figure 6.1: Variation of $\frac{V}{6A}$ with T and V.

behavior, the device force can be calculated directly from pressure gradient measurements. Pressure measurements and (6.2) are used to calculate device forces in the experiments which follow. Calculating the force in this fashion eliminates the friction caused by seals and other sliding mechanisms within the device; this force is therefore representative of the ER fluid behavior.

6.2 Small Scale Device

The purpose of this series of experiments was to evaluate the applicability of the analytical models presented in Chapter III.

6.2.1 Dimensions, Materials, and Test Configuration

The ER behavior of the material used in this series of tests (100 micron aluminosilicate particles in light mineral oil) is reported in Figure 6.2. These material properties were obtained using a Couette rheometer. The bob diameter of this rheometer was 25.4 mm and the gap was 1 mm. Note that the value of the yield stress for (shear-thinning) ER gels depends strongly on the value of the shear rate at which yielding

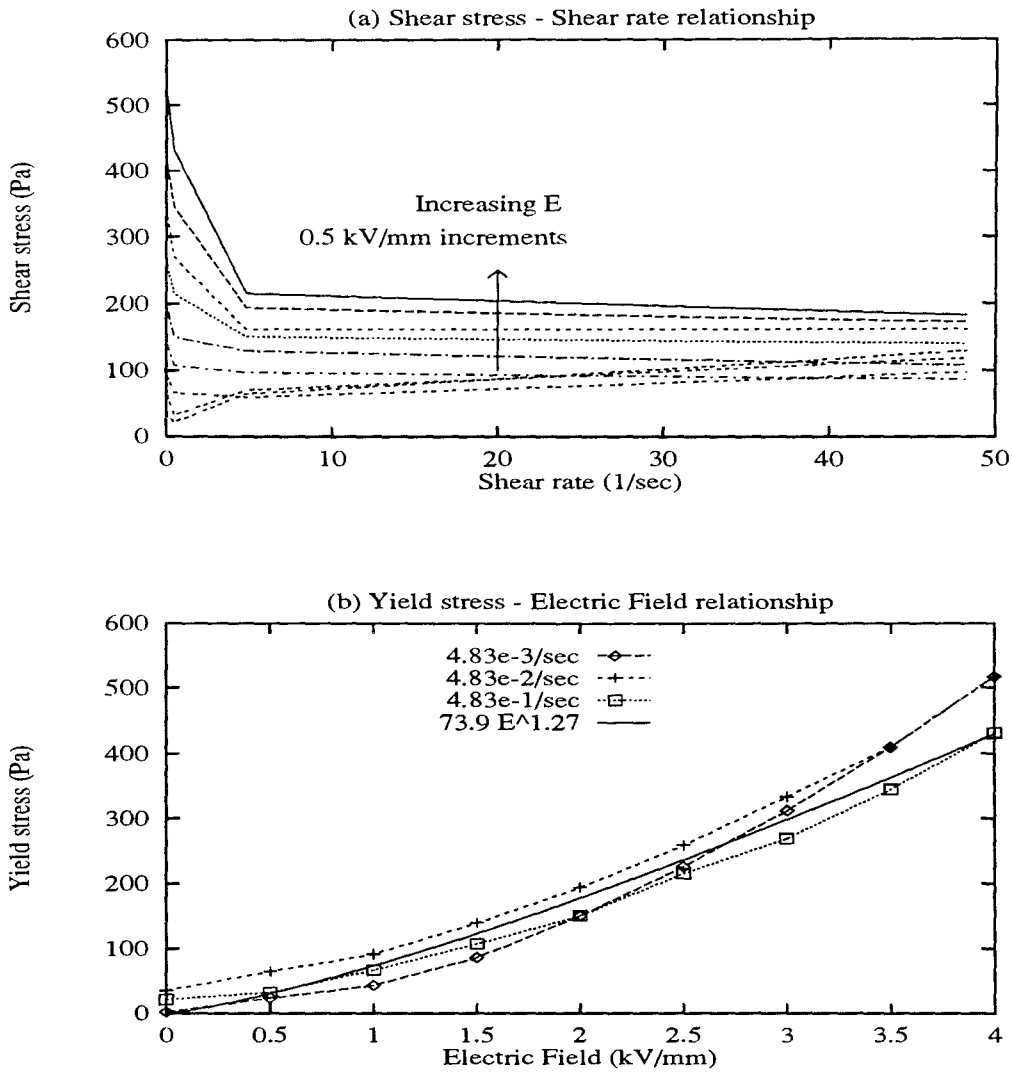

Figure 6.2: Shear thinning behavior of the ER materials used in the small device: (a) τ v. $\dot{\gamma}$ for 0 kV/mm $< E <$ 4 kV/mm, (b) τ_y v. E for 0.0048/sec $< \dot{\gamma} <$ 0.48/sec.

is defined. The definition of the yield shear-rate should be application-specific, to accurately model the flow of these materials. In this study, the yield stress is defined as an average of the electric field dependent shear stresses between shear rates of 0.0048/sec and 0.48/sec. With this definition, the yield stress is related to the electric field by the power law:

$$\tau_y(E) = 73.9E^{1.27}, \tag{6.9}$$

where τ_y is in Pa and E is in kV/mm. The exponent in (6.9) commonly ranges from 1.2 to 2.5 in ER materials. Also note that η decreases with E at low values of E and that behavior at 0.0 kV/mm is qualitatively the same as the behavior at 0.5 kV/mm. Couette rheometer test data is illustrated in Figure 6.2.

To test the behavior of this ER material in Poiseuille flow, a small scale test device was designed and constructed. The test device is described in Figure 6.3. It consists of a single prismatic plunger (t=12.7 mm, l=50.4 mm, b=150 mm) which was actuated vertically through ER fluid in an open box. The plunger is made of 6061-T6 aluminum and has a clear anodized surface, which sealed the metal and prevented fine aluminum particles from entering the ER material. Corners of the plunger were rounded to reduce local charge concentrations, and to provide a more stream-lined duct entrance. The plunger was guided between the anodized aluminum walls of the box by Plexiglas guides. The clearance between the plunger and the box, h, can be set between 1 mm and 3 mm. Gaps much larger than 3 mm require X-ray level voltages (20 kV) for fields capable of producing a strong ER effect. As the plunger moved through the ER fluid, fluid was displaced and flowed through the gap h. Figure 3.1 describes this flow condition.

Figure 6.4 illustrates the test configuration. Signal conditioning electronics were

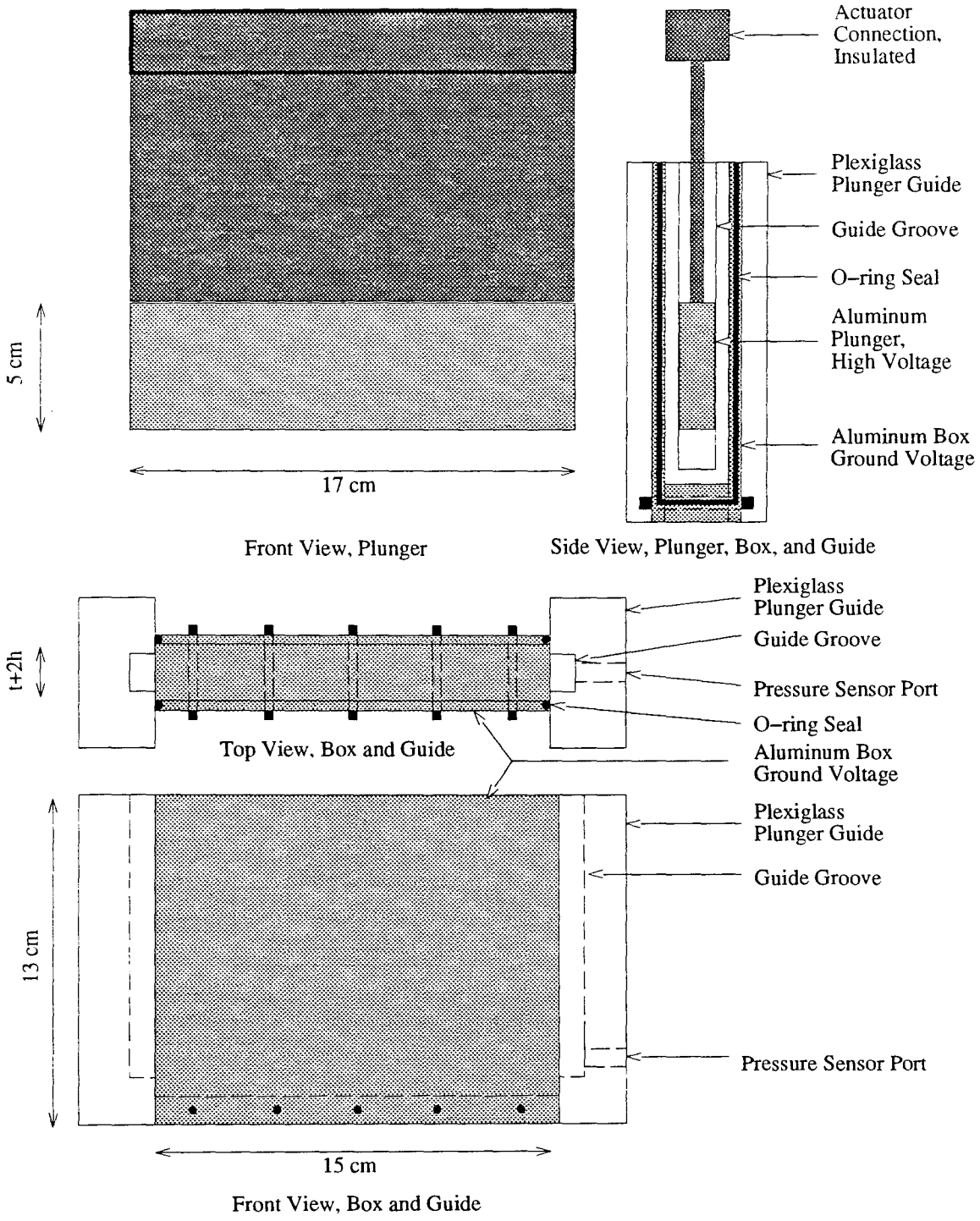

Figure 6.3: Configuration of the small-scale ER test device.

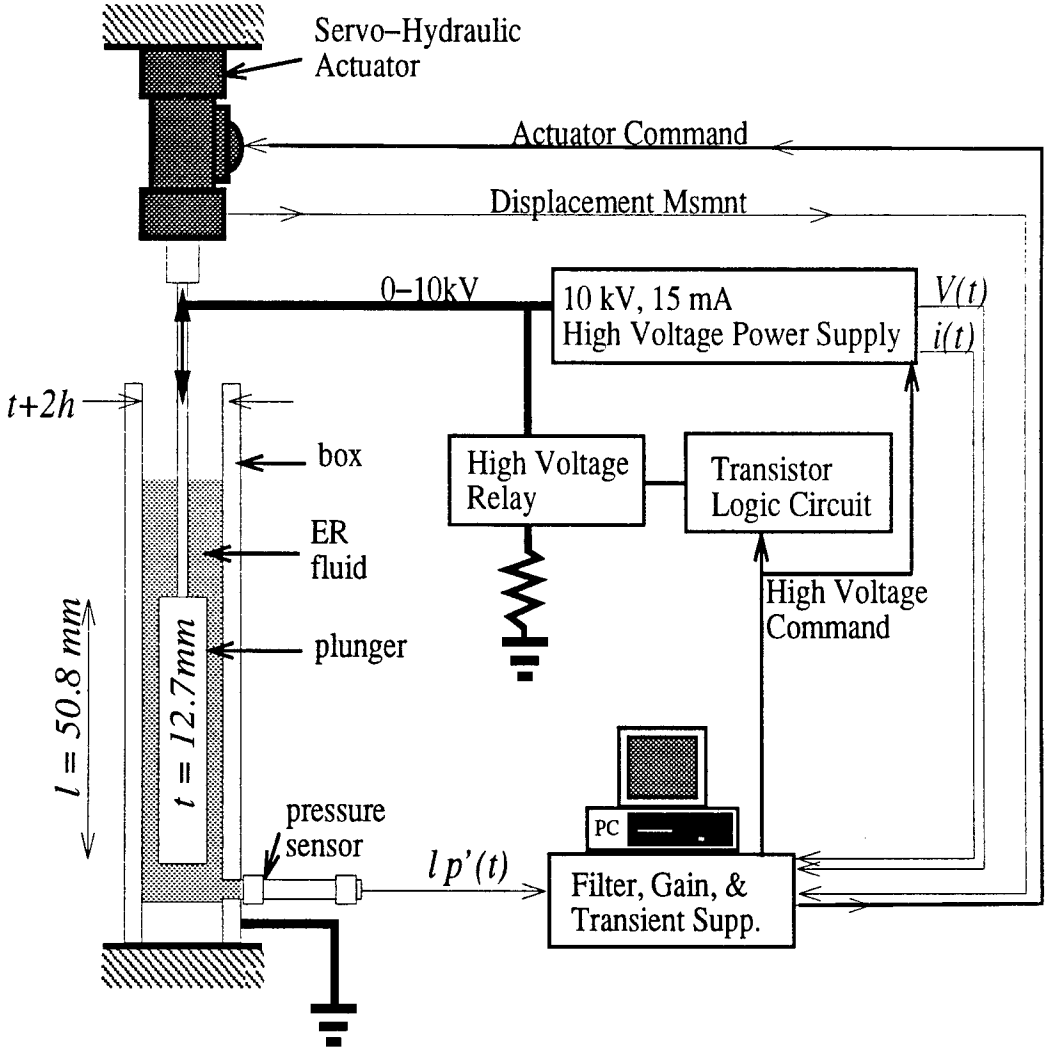

Figure 6.4: Configuration of the small test device, hydraulic actuator, high voltage supply, data acquisition, and control.

designed and fabricated on a custom printed circuit board. The signal conditioning provided low-pass filtering, gain, and most importantly, high-voltage transient suppression. High voltage metal-oxide varistors (MOV)'s are two terminal passive devices which behave like bi-directional zener diodes. When a threshold voltage is reached, they become conducting. Otherwise, they offer very high impedance. MOVs between signals from sensors in high voltage environments and ground quench high-voltage transients in the signals or the ground. Data was collected on an IBM PC/XT with a MetraByte DAS16F data acquisition card. The data acquisition and control card was programmed in C to carry out the control and measurement functions required by these tests. The PC delivered a displacement command signal which was smoothed by a custom filter prior to being sent to a servo-hydraulic actuator, and a high-voltage command to a regulated high-voltage power supply. The device, actuator, and PC were operated during high-voltage arcing with no discernible effect on the actuator performance or the collected data. As the plunger was cycled through the ER fluid, measurements of ER fluid pressure response, actuated plunger displacement, applied high voltage, and electrical current were collected. Tests were conducted with constant and fast-slewing electric fields. The ER test device never drew more than 5 Watts, and could have been operated from a battery.

6.2.2 Constant Voltage Tests

In the constant E tests, ten sinusoidal cycles at 6, 3, and 1.2 second periods were actuated with steadily increasing amplitudes. An example of the applied test motions is shown in Figure 6.5. Tests were conducted at several electric field strengths. Only the zero and full electric fields are shown for illustrative purposes. Hysteresis loops for the intermediate field strengths fall between these illustrated loops. Figures 6.6,

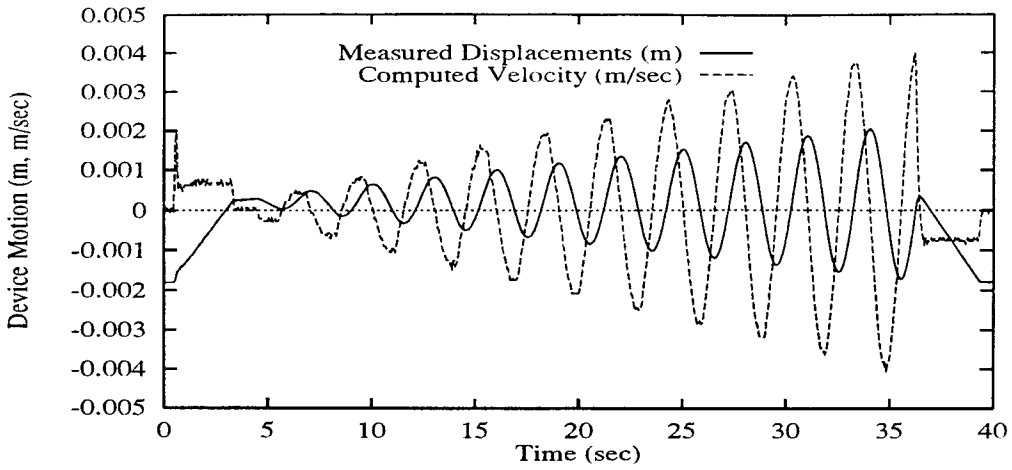

Figure 6.5: Applied test motions for the small ER device at a constant electric field. The period of the sinusoidal motion in this test is 3 seconds.

6.8, and 6.10, illustrate the repeatability and range of the hysteresis loops obtained from constant E tests of 0 kV/mm and 3.34 kV/mm, and a gap of $h = 2.38$ mm. Figures 6.7, 6.9, and 6.11, illustrate the repeatability and range of the hysteresis loops obtained from constant E tests of 0 kV/mm and 2.5 kV/mm, and a gap of $h = 0.96$ mm. Figures 6.6 and 6.7 correspond to the 1.2 second period motion, Figures 6.8 and 6.9 correspond to the 3.0 second period motion, and Figures 6.10 and 6.11 correspond to the 6.0 second period motion. A static yield stress, in excess of the dynamic yield stress, can be inferred from these figures.

The more rounded hysteresis loops at higher frequencies are due to an increase in viscous stresses. In the long period motions, the deformation rates are much lower and the effects of shear thinning and pre-yield behavior become important. As the viscous stresses increase (smaller gap h or higher velocity) the ratio of maximum to minimum forces decreases.

Using the measurements described above, coordinates (T, P) can be calculated

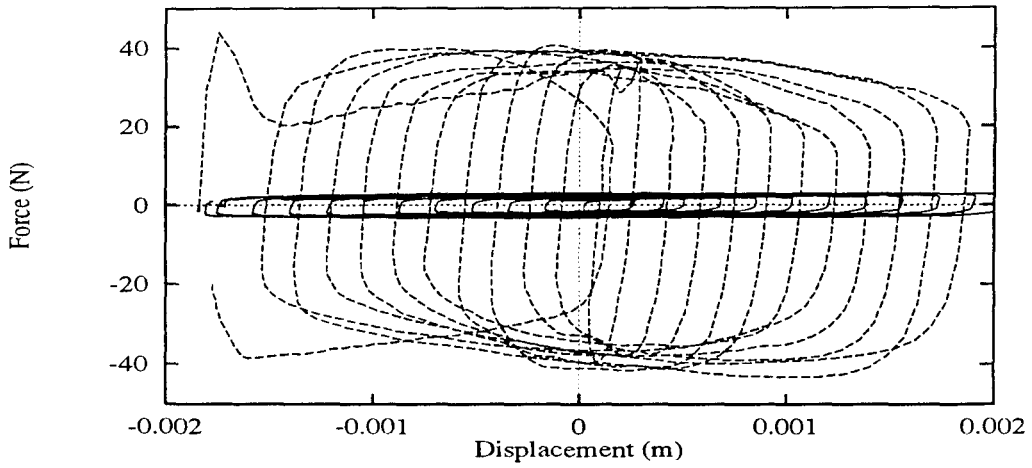

Figure 6.6: Experimental ER hysteresis loops at constant voltages ($E = 0.0$ kV/mm and $E = 3.34$ kV/mm) and increasing sinusoidal amplitudes (1.2 sec. sinusoidal period, $h = 2.38$ mm).

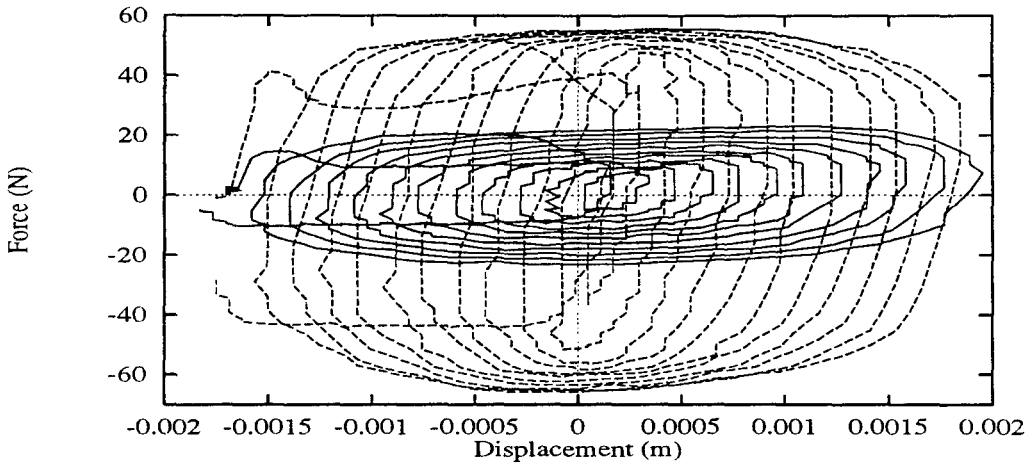

Figure 6.7: Experimental ER hysteresis loops at constant voltages ($E = 0.0$ kV/mm and $E = 2.50$ kV/mm) and increasing sinusoidal amplitudes (1.2 sec. sinusoidal period, $h = 0.96$ mm).

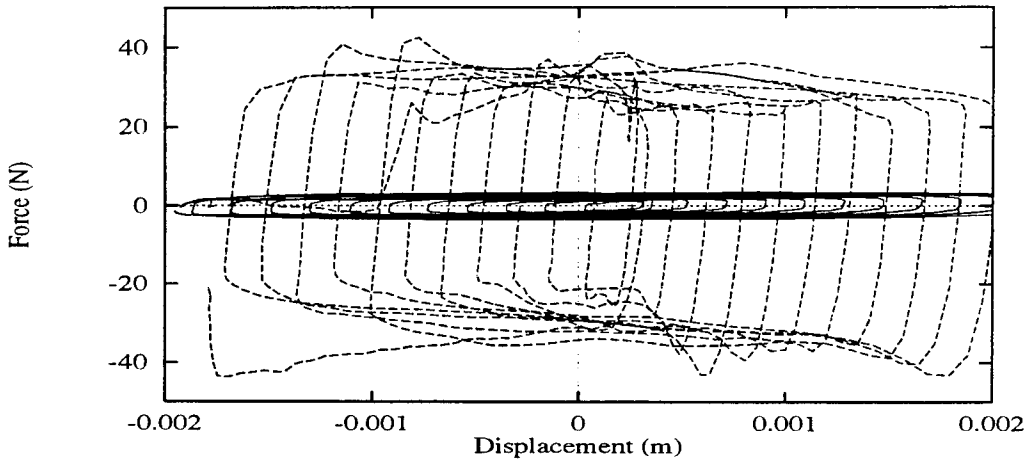

Figure 6.8: Experimental ER hysteresis loops at constant voltages ($E = 0.0$ kV/mm and $E = 3.34$ kV/mm) and increasing sinusoidal amplitudes (3.0 sec. sinusoidal period, $h = 2.38$ mm).

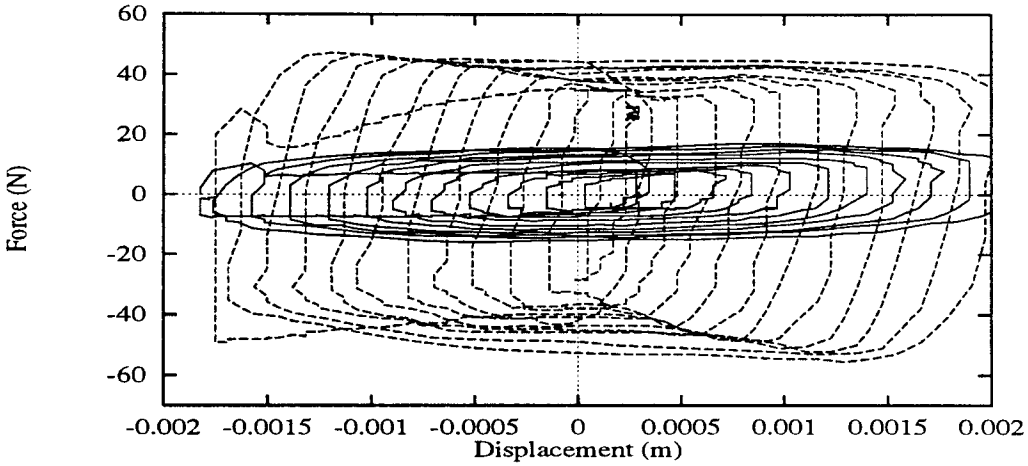

Figure 6.9: Experimental ER hysteresis loops at constant voltages ($E = 0.0$ kV/mm and $E = 2.50$ kV/mm) and increasing sinusoidal amplitudes (3.0 sec. sinusoidal period, $h = 0.96$ mm).

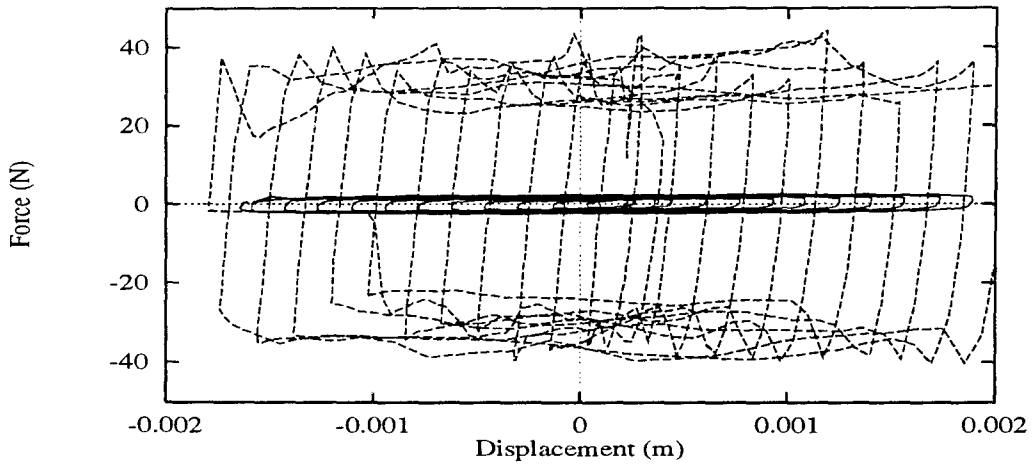

Figure 6.10: Experimental ER hysteresis loops at constant voltages ($E = 0.0$ kV/mm and $E = 3.34$ kV/mm) and increasing sinusoidal amplitudes (6.0 sec. sinusoidal period, $h = 2.38$ mm).

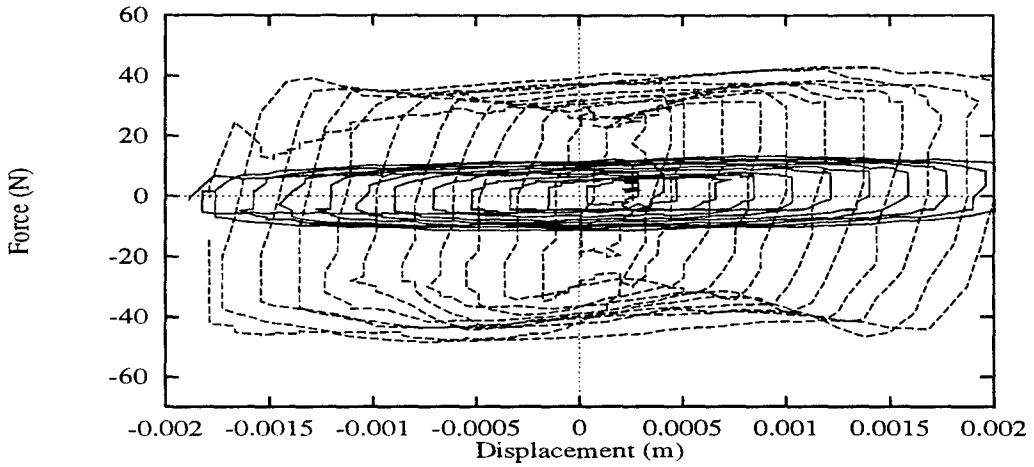

Figure 6.11: Experimental ER hysteresis loops at constant voltages (E =0.0 kV/mm and $E = 2.50$ kV/mm) and increasing sinusoidal amplitudes (6.0 sec. sinusoidal period, $h = 0.96$ mm).

from the test data, and equations (6.9), (3.13) and (3.14).[2] These data points are plotted along with the approximate solution (3.22) in Figures 6.12a and 6.12b. Most

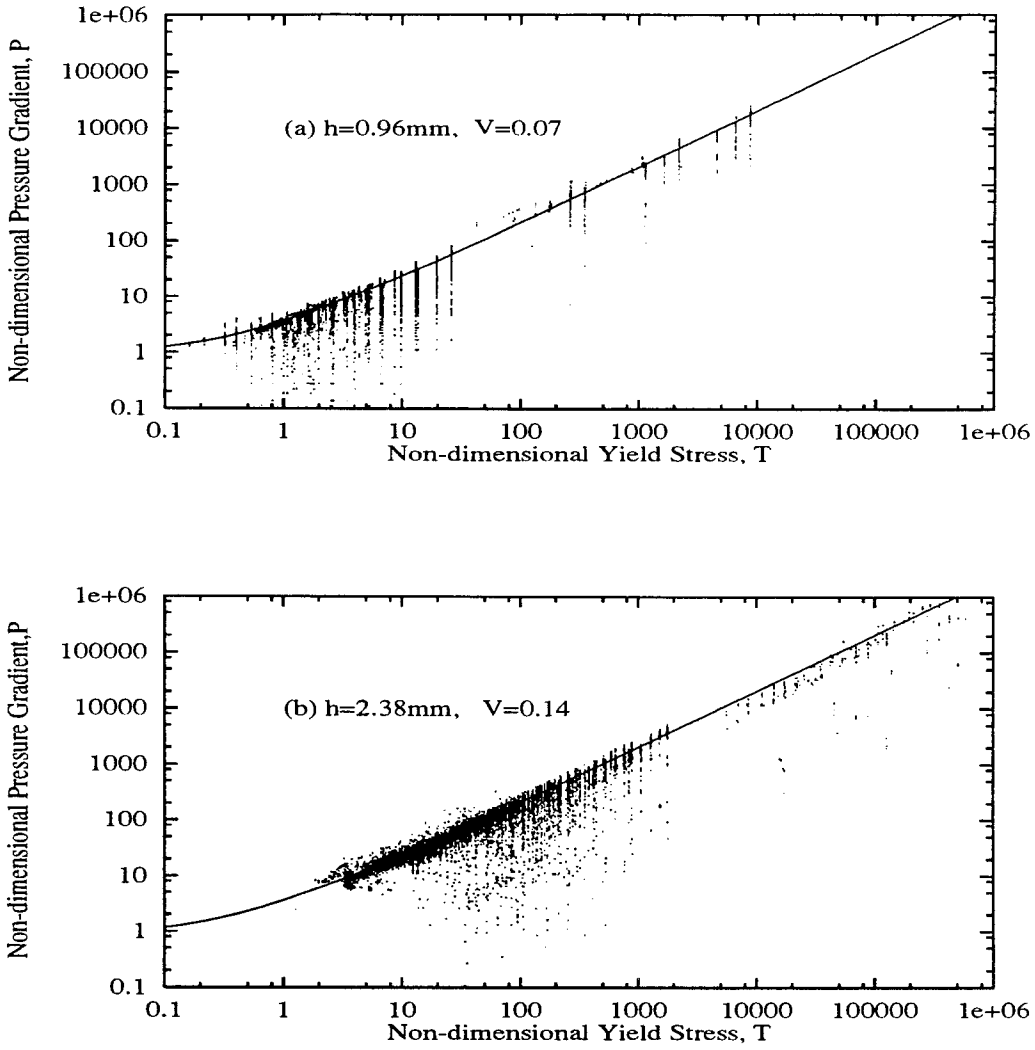

Figure 6.12: Quantitative evaluation of the Bingham flow equations for ER materials: (a) h=0.96 mm (b) h=2.38 mm.

of the data agrees with the Bingham model. Note that in the tests with $h = 2.38$ mm, the data points lie in a region of greater dynamic range, P, than do the data points for the tests with $h = 0.96$ mm. Out-lying data points below the analytical curve correspond to the low shear-rate, transition visco-elastic region, which is not mod-

[2]A value for η equal to 0.35 Pa s was chosen based on the test results at $E = 0$.

eled by (2.3). The presence of non-uniform properties could be another source of scatter in this data. These figures illustrate that Bingham behavior is indeed a limiting behavior for ER materials in steady flow and large deformations. However, at small deformations, mechanisms not modeled by the Bingham equation dominate the behavior. In this region, the visco-elastic and shear-thinning properties of the ER material are important.

Figure 6.12 may not be the most compelling support for the Bingham equation as a model for ER behavior. Comparing measured pressure responses to those predicted from the Bingham model is another means of assessing the accuracy of the Bingham model. Figure 6.13 illustrates this comparison. The high frequency oscillations can

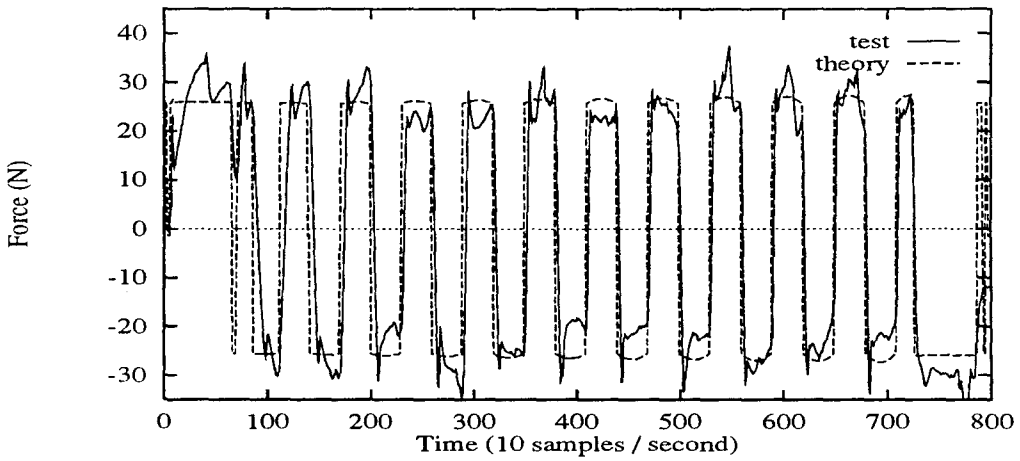

Figure 6.13: Experimental ER pressure response and the pressure response of a corresponding Bingham material. ($E = 2.92$ kV/mm) and increasing sinusoidal amplitudes (6.0 sec. sinusoidal period, $h = 2.38$ mm).

not be described by the Bingham model. The Bingham equation is, nevertheless, successful in capturing the average force level in these oscillations. Note that the measured pressure response lags the theoretical response of an inertia-less Bingham fluid.

6.2.3 Variable Voltage Tests

To test the response of p' to step-like changes in E, periodic motions of constant velocity (triangle-wave displacements) were actuated in conjunction with the high voltage on the ER test device. These signals were coordinated so that pressure transients at mid-stroke would be due to changes in material properties alone. Each time the displacements passed through zero, several kV were delivered to the ER test device. An example of the applied test motions is shown in Figure 6.14. Figure 6.15 illustrates the applied electric field corresponding to Figure 6.14. The

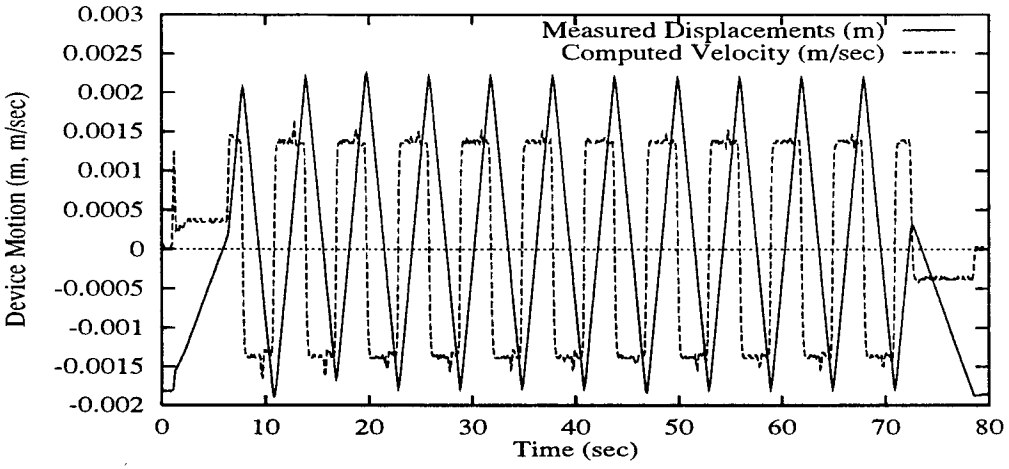

Figure 6.14: Applied test motions for the small ER device at variable electric fields. The period of the constant velocity motion in this test is 6 seconds.

electrical current is also shown in this figure. The RC time constant of the device depends on the (non-ohmic) conductivity of the ER fluid and can range from 1 to 3 seconds. Better ER materials conduct lower currents, and therefore have longer RC time constants. Nevertheless, electric fields can be discharged in micro-seconds by closing a high voltage relay whenever the high voltage command signal drops to zero. This control decision is implemented in an analog circuit. Figures 6.16 and 6.17 demonstrate the importance of the relay in achieving fast-slewing pressure responses.

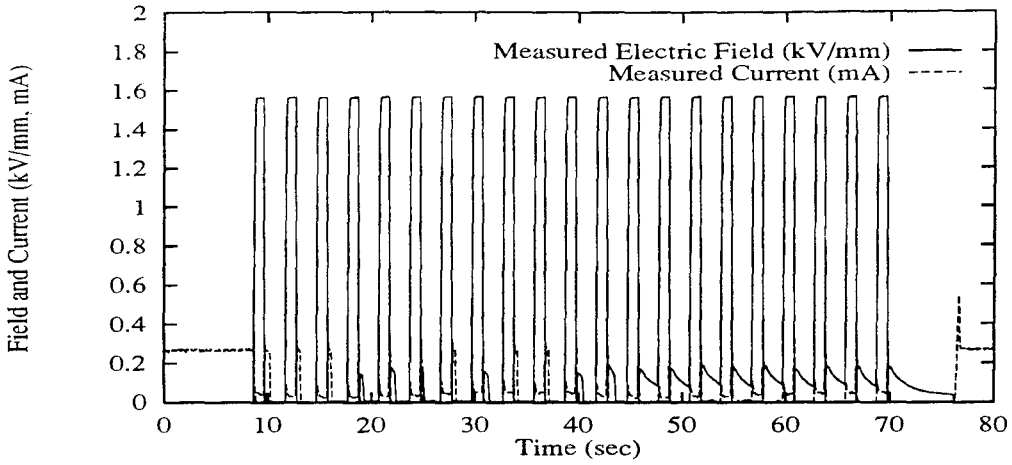

Figure 6.15: Applied electric field for the small ER device at variable electric fields. The period of the electric field application in this test is 3 seconds.

In Figures 6.18a and 6.18b, two sets of pressure response data (h = 0.96 mm and

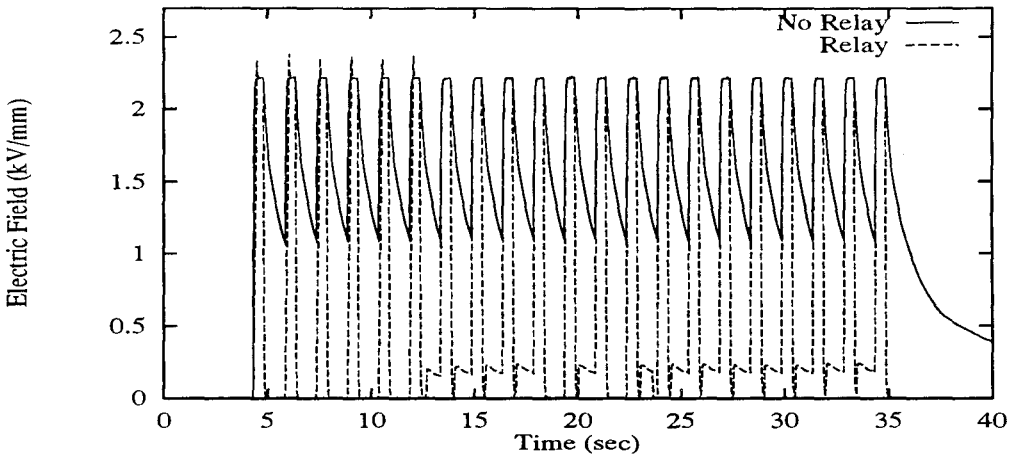

Figure 6.16: Effect of the high voltage relay on transient electric fields.

h = 2.38 mm) are compared to the model of (3.22) (which assumes that the fluid can respond arbitrarily fast). Equation (3.21) compares favorably to the test results for the h=0.96 mm case, indicating that inertia effects are not important for gap sizes less than 1 mm. For the h=2.38 mm case, Figure 6.18b shows that the measured pressure response is somewhat slower than the response of a fluid with zero inertia.

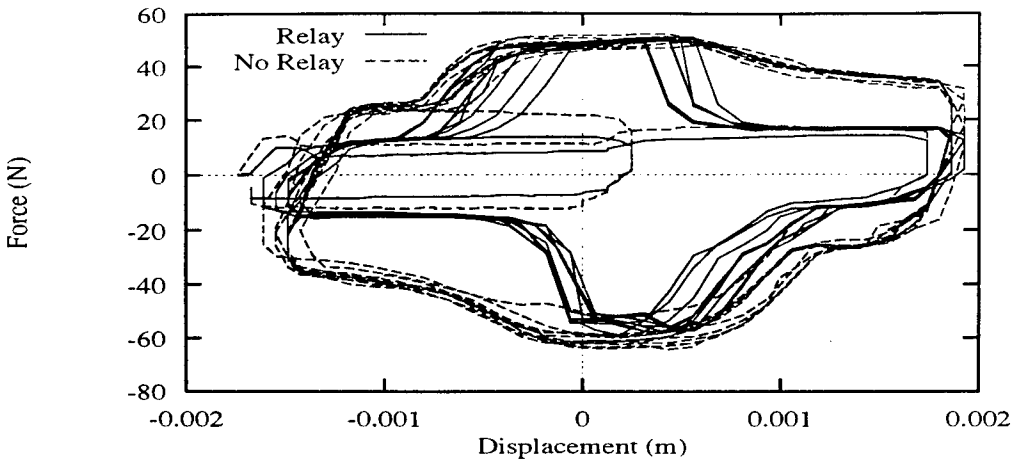

Figure 6.17: Effect of the high voltage relay on ER pressure transients.

Also, the pressure gradient responds more slowly to increasing electric fields than to decreasing electric fields in both cases.

These small scale tests showed that the equations of Bingham flow describe actual ER materials in the limiting case of steady, fully developed flow. At low shear rates the shear thinning of the ER material becomes increasingly important, and at low shear strains, the pre-yield (linear visco-elastic) behavior dominates. Nevertheless, most of the data points collected in these experiments agree with the Bingham model. The effect of fluid inertia on the pressure response of the fluid undergoing material property changes agrees qualitatively with the relations presented in Chapter III. ER fluids flowing in gaps larger than 1 mm respond more slowly to changes in the yield stress, due to inertial effects. Two definitive conclusions which can be drawn from this study are:

- wider gaps produce larger dynamic ranges, and
- wider gaps produce slower response times.

Data presented in this section shows that the behavior of even simple ER devices

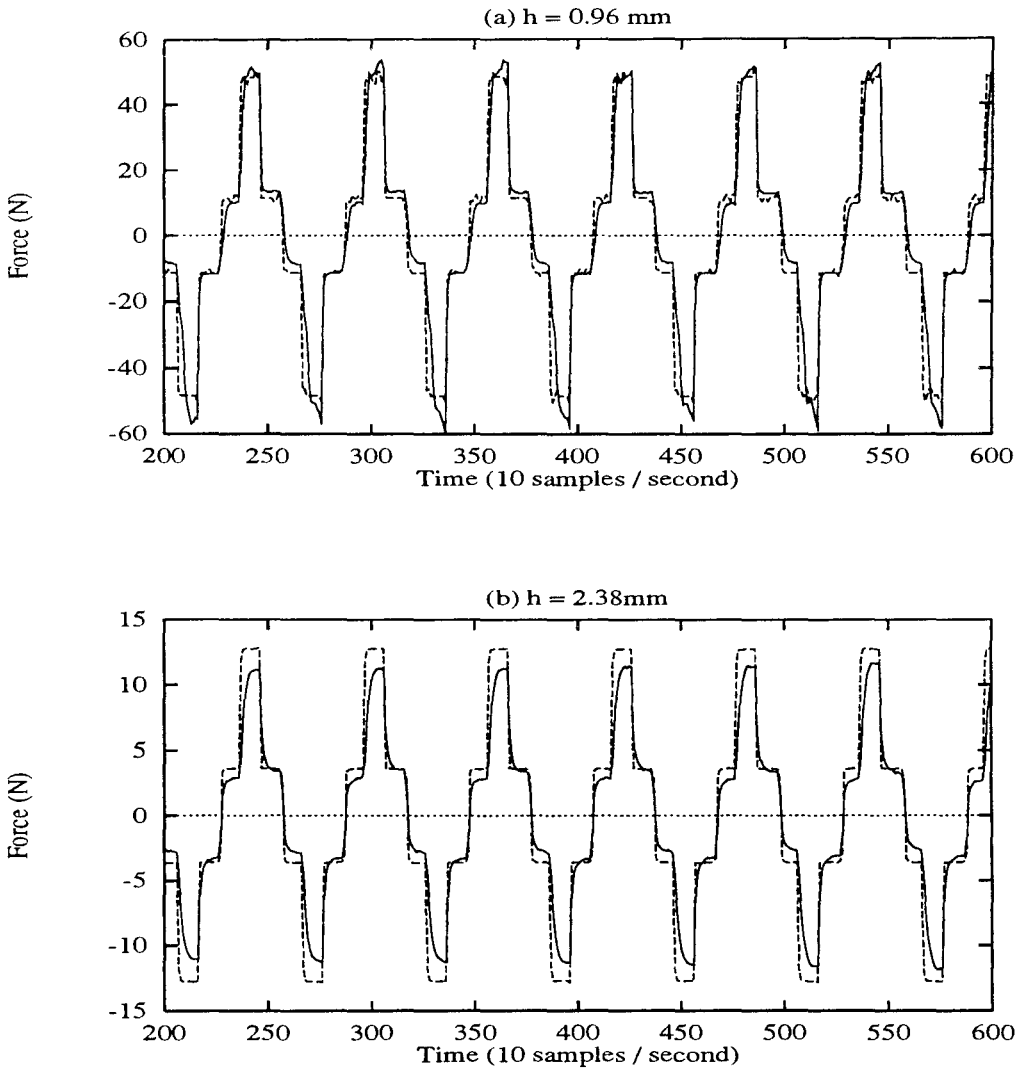

Figure 6.18: Transient pressure responses for an actual ER fluid: — and an ideal inertialess Bingham fluid: - - - -. (a) $h = 0.96$ mm, $E = 2.21$ kV/mm (b) $h = 2.38$ mm, $E = 1.57$ kV/mm.

can be quite complex. As device geometries increase in size and complexity, it is reasonable to assume that their behavior will as well. The next section describes a large scale ER device and presents data from cyclic testing of the device.[3] Test data is compared to the Bingham model, and is used to evaluate the non-parametric model described in Chapter V.

6.3 Large Scale Device

The purpose of the large device tests was:

- to gain experience in the use of ER dampers for large-scale structural applications,
- to evaluate the design equations presented in Chapter III, and
- to generate a data base for evaluating ER device modeling methods.

6.3.1 Dimensions, Materials, and Test Configuration

The ease of manufacture, assembly, and disassembly were important design criteria for this experimental device. The device was comprised of an array of $N = 9$ rectangular plates, all bolted together. The outer and alternate plates were connected to a high voltage potential. In mixed-mode ER devices, using parallel rectangular plates, the number of plates must be odd. A $h_i = 0.78$ mm gap was provided by over-sized washers around the screws connecting the plates. These screws provided electrical contact between the high-voltage plates. They were isolated from the ground potential plates using small non-conducting washers. The washers and spacers were made of Nomex, a DuPont product. Nomex has excellent properties in terms of

[3] In the course of the research, results from the large scale tests motivated the small scale experiments.

dielectric strength, stiffness, and durability. PTFE insulation was too compliant to be used as a washer. The plates were fabricated from $t = 4.76$ mm thick 6061-T6 aluminum. The area of each plate surface was 254 mm by 356 mm = 0.090 m^2. The edges of the plates were rounded to reduce electric charge concentrations, cavitation, and the possibility of arcing. It was found during early testing stages that the open grain of the 6061-T6 aluminum was difficult to clean. Even after repeated sanding, polishing, and washing, minute grains of aluminum became suspended in mineral oil. These metallic particles significantly reduced the dielectric break-down voltage of the device/fluid combination. Therefore, in an attempt to seal the aluminum, all surfaces exposed to ER material were anodized. Figure 6.19 illustrates the device and its actuator connection.

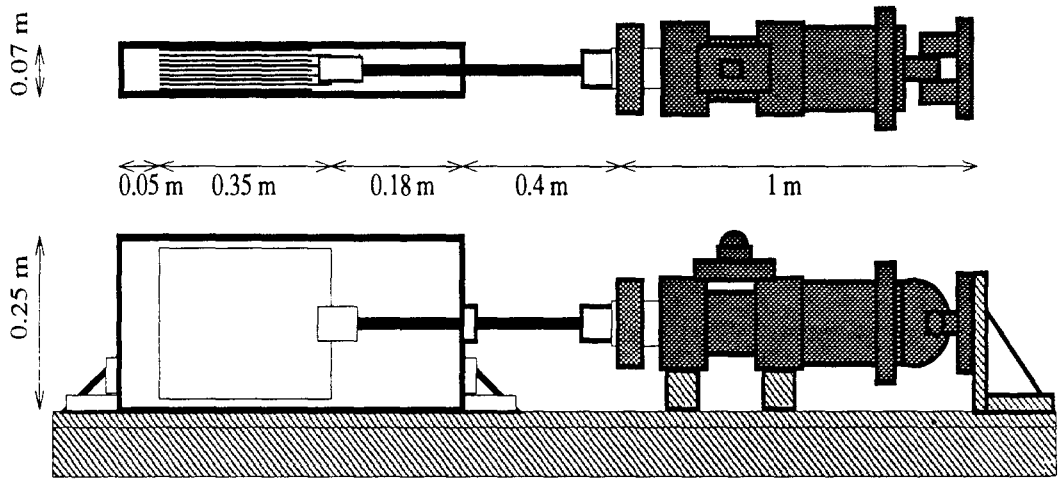

Figure 6.19: Configuration of the large test device and hydraulic actuator.

The plates moved rectilinearly within a snug-fitting case. The outer gaps, h_o, were roughly 1.5 times the inner gaps h_i. A minimum outer gap of h_i was guaranteed by extending Nomex sheets into the box, parallel to the plates, at the corners of the box. During testing, the plates moved horizontally and were oriented so that the gaps were perpendicular to the floor. The edges of the plates rested on, and slid along,

the bottom surface of the box. To prevent short-circuits of the high voltage and to reduce friction, the plate-bearing faces of the box were laminated with polyester.

A 1 inch diameter hardened steel tubular shaft, connected to the plates, passed through the case. An O-ring energized PTFE wiper seal performed satisfactorily in sealing the device with minimum friction. The box was sealed with cork, rubber, and Nomex gaskets. The over-all outer dimensions of the box were 80 cm by 5 cm by 30 cm. The device was designed such that the plates could move with a stroke of 20 cm. A 22 gauge wire passing through the steel shaft connected the high-voltage plates to the power supply. The ground potential plates were physically and electrically connected to the shaft, which provided the (low impedance) ground connection. Plates adjacent to the case were at high voltage, thereby creating an electric field in the outer gaps.

The dimensionless wall velocity, V, for this device is 0.08, as calculated from (B.32). So the pressure drop along the outer gaps is almost the same as the pressure drop along the inner gaps, and (6.2) is sufficiently accurate, especially in light of the unmodeled complexities of ER material behavior.

6.3.2 Experimental Data

A 100 kN, 15 cm, capacity MTS hydraulic actuator was fixed horizontally to a W10 section beam. The ER device was carefully shimmed and aligned with the actuator and securely clamped to the beam as well. Electrical isolation between the high-voltage ground and the actuator was considered important due to the possibility of high-voltage transients on the device ground during arcing within the device. The connection between the actuator and the device was made via a G-10 spun glass coupler.

Sinusoidal motions were actuated to obtain data for characterization studies. The periods were long, reflecting the large-scale nature of the device and the envisioned application. These periods ranged from 2 to 10 seconds. The period did not change during the test.

Initial evaluation tests were carried out using a mineral oil based ER fluid and a kerosene based ER fluid. The mineral oil based fluid produced force levels 6 times as great as the force levels achieved with the kerosene based fluid. The dynamic range with the mineral oil fluid was half that of the kerosene based fluid. Displacement based hysteresis loops for tests using the mineral oil fluid are illustrated in Figure 6.20. The nearly elliptical shape, and the small dynamic range (2.5), indicate that (uncontrollable) viscous stresses dominated the behavior in these tests, despite the low velocities. Figures 6.21 and 6.22 illustrate displacement and velocity hysteresis loops from tests using a kerosene-based ER fluid. The lower base-viscosity of this material resulted in smaller viscous stresses and a greater dynamic range, even at higher velocities. The velocity based hysteresis figure demonstrates the Bingham-like

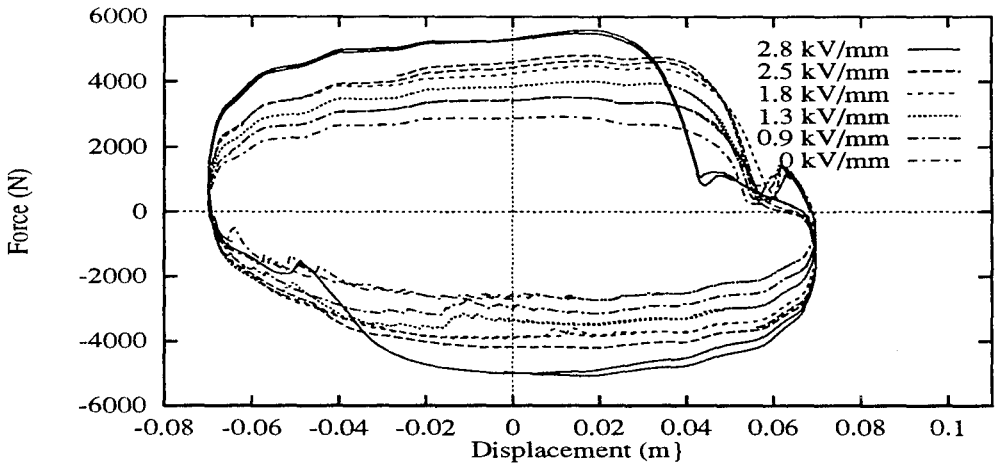

Figure 6.20: Hysteresis loops from initial tests using a mineral oil based ER fluid. The period of the sinusoidal motion in this test was 14.3 seconds.

behavior of the device.

Device characterization tests were conducted with a kerosene-diluted sample of the kerosene based ER fluid used in the initial test series. The ER behavior of the material used in this series of tests (1 micron alumino-silicate particles in kerosene) are reported in Figure 6.23. These material properties were obtained from Couette rheometer tests. The bob diameter of this rheometer was 2.54 cm and the gap was 1 mm. In these tests higher shear rates were anticipated than in the earlier tests. So the yield stress is defined as the electric field dependent shear stress at a rates of 1.42/sec. The yield stress is related to the electric field by the power law:

$$\tau_y(E) = 15.5E^{1.86}, \tag{6.10}$$

where τ_y is in Pa and E is in kV/mm. Also note that η decreases only slightly with E at low values of E.

To obtain device data over a large portion of the phase-plane, the sinusoidal amplitudes increased linearly with time. An example of the applied test motions is illustrated in Figure 6.24.

The signal conditioning, transient suppression, and data acquisition were the same as those described in the previous section. Fluid pressures across the device, actuator displacements, actuator forces, voltage levels, and electric currents were measured.

Equivalent damping ratios c_{eq} were calculated from the measured hysteresis loops, the known sinusoidal period, and the amplitude of motion:

$$c_{eq} = \frac{W_D T}{2\pi^2 A^2}, \tag{6.11}$$

where W_D is the energy dissipated per cycle, T is the period of the excitation and A is the amplitude of the response. The dependence of c_{eq} on A is illustrated in

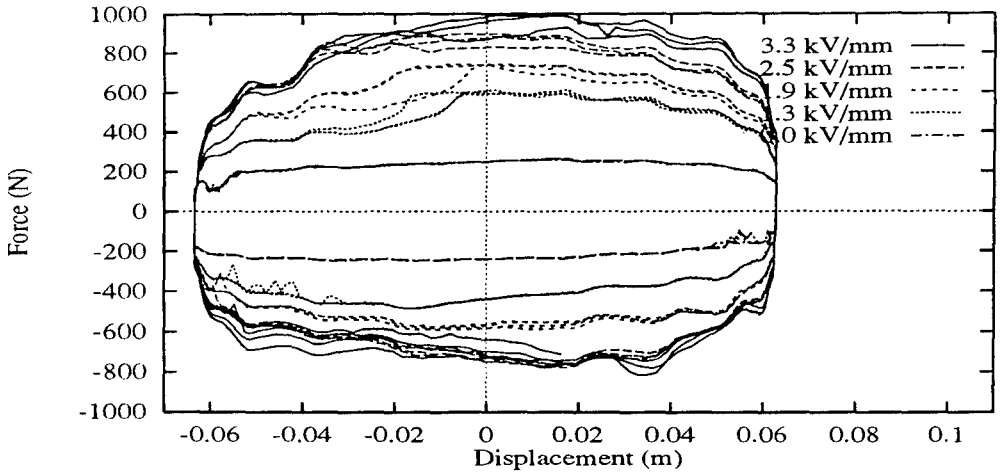

Figure 6.21: Displacement based hysteresis loops from initial tests using a kerosene based fluid. The period of the sinusoidal motion in this test was 9.1 seconds.

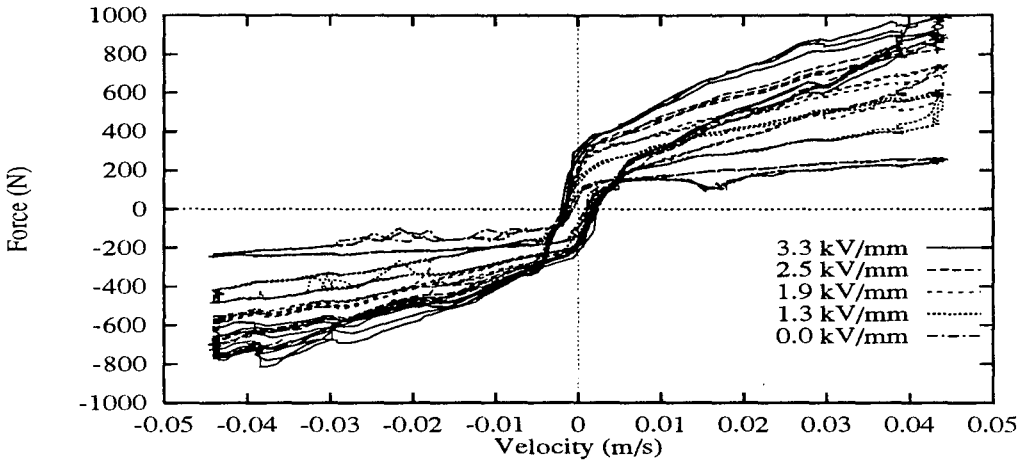

Figure 6.22: Velocity based hysteresis loops from initial tests using a kerosene based fluid. The period of the sinusoidal motion in this test was 9.1 seconds.

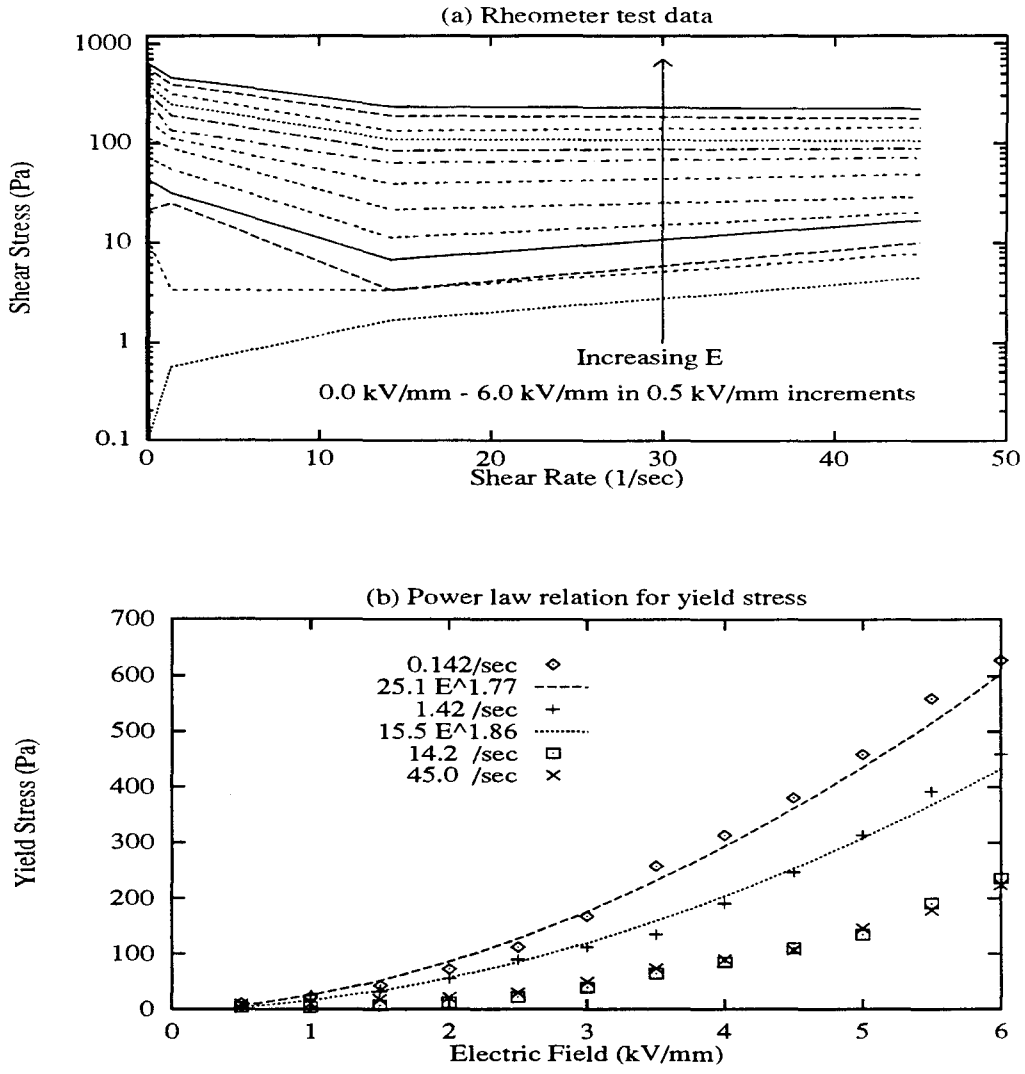

Figure 6.23: Shear thinning behavior of the ER materials used in the large device: (a) τ v. $\dot{\gamma}$ for 0 kV/mm $< E <$ 6 kV/mm (b) τ_y v. E for 0.142/sec $< \dot{\gamma} <$ 45/sec.

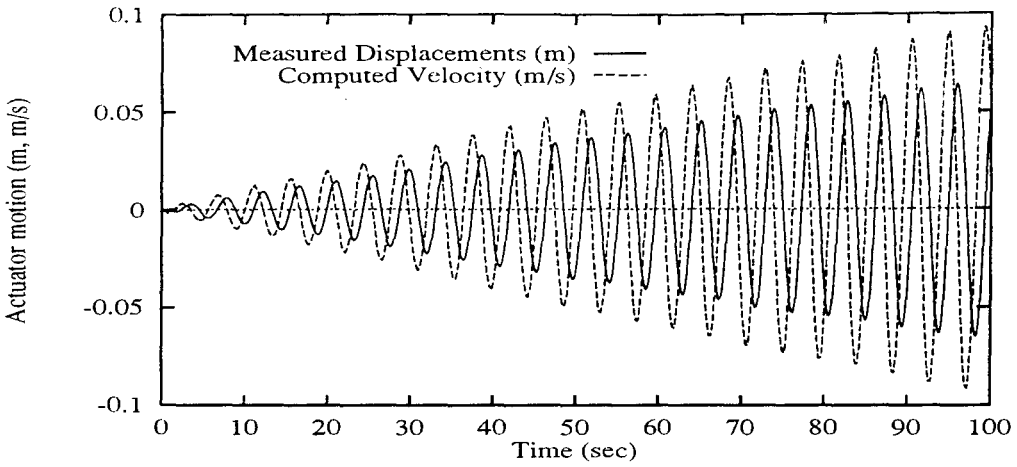

Figure 6.24: Applied test motions for the large ER device at a constant electric field. The period of the sinusoidal motion in this test was 4.3 seconds.

Figure 6.25. Decreasing equivalent damping with increasing amplitude is an artifact of the Coulomb-type damping of ER devices.

Using the test data and (6.2), experimental hysteresis loops were plotted and compared to the hysteresis of a comparable Bingham fluid (see Figure 6.26). Rheometer studies of the ER fluid (Figure 6.23) give a value of 0.5 Pa-sec for η and 100 Pa for τ_y at 3.2 kV/mm and high shear rates. The Bingham equation was useful for a rough description of the force levels in an ER device. It can not capture the details of hysteretic behavior under cyclic loading conditions.

6.3.3 Non-Parametric Modeling

Test data (displacements, x, velocity $\dot{x}$, electric field, E, and force, f time histories) can be curve-fit with Chebyshev polynomials in multiple dimensions. The resulting model can capture significant features of the non-linear behavior of the device. Although the form of this non-parametric model has no physical meaning, it is general enough to allow arbitrary non-linearities. The domain of the curve-fit is a three dimensional space with coordinates corresponding to $(x, \dot{x}, E)$.

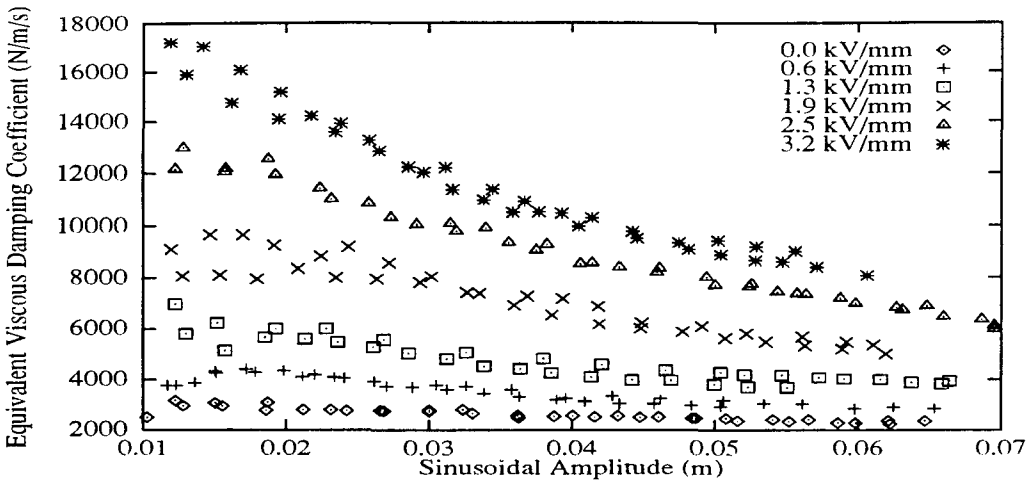

Figure 6.25: Effect of amplitude of motion and electric field on the equivalent damping ratio, c_{eq}. The period of the sinusoidal motion in this test was 4.3 seconds.

Two series of tests were conducted to evaluate the predictive capabilities of the Chebyshev curve-fit (5.6), (5.8) and (5.9). Data from the first series of tests were used to calculate the curve-fit coefficients. Data from the second series of tests were used to evaluate the ability of the curve-fit to predict the device behavior.

In the first series of tests, smooth prescribed motions, illustrated in Figure 6.24, and constant electric fields were applied to the device. The electric field values were: 0.0, 0.6, 1.3, 1.9, 2.5, and 3.2 kV/mm. The accuracy of the curve-fit depends strongly on the degree,(I, J, K) of the polynomials used for curve-fitting. By evaluating the average relative root mean square (RMS) error of the curve-fit, e,

$$e = \frac{\left[\frac{1}{T}\sum_{t=1}^{T}(f_t - \hat{f}_t)^2\right]^{1/2}}{\left[\frac{1}{T}\sum_{t=1}^{T}(f_t)^2\right]^{1/2}}, \tag{6.12}$$

as a function of the polynomial degree, I, J, K, an intelligent choice can be made for the degree of the polynomial. As well as the polynomial degree, the number of interpolation points, (P, Q, R) for the evaluating the interpolated function affects the error of the resulting curve-fit. The influence of I, J, K and P, Q, R on e is

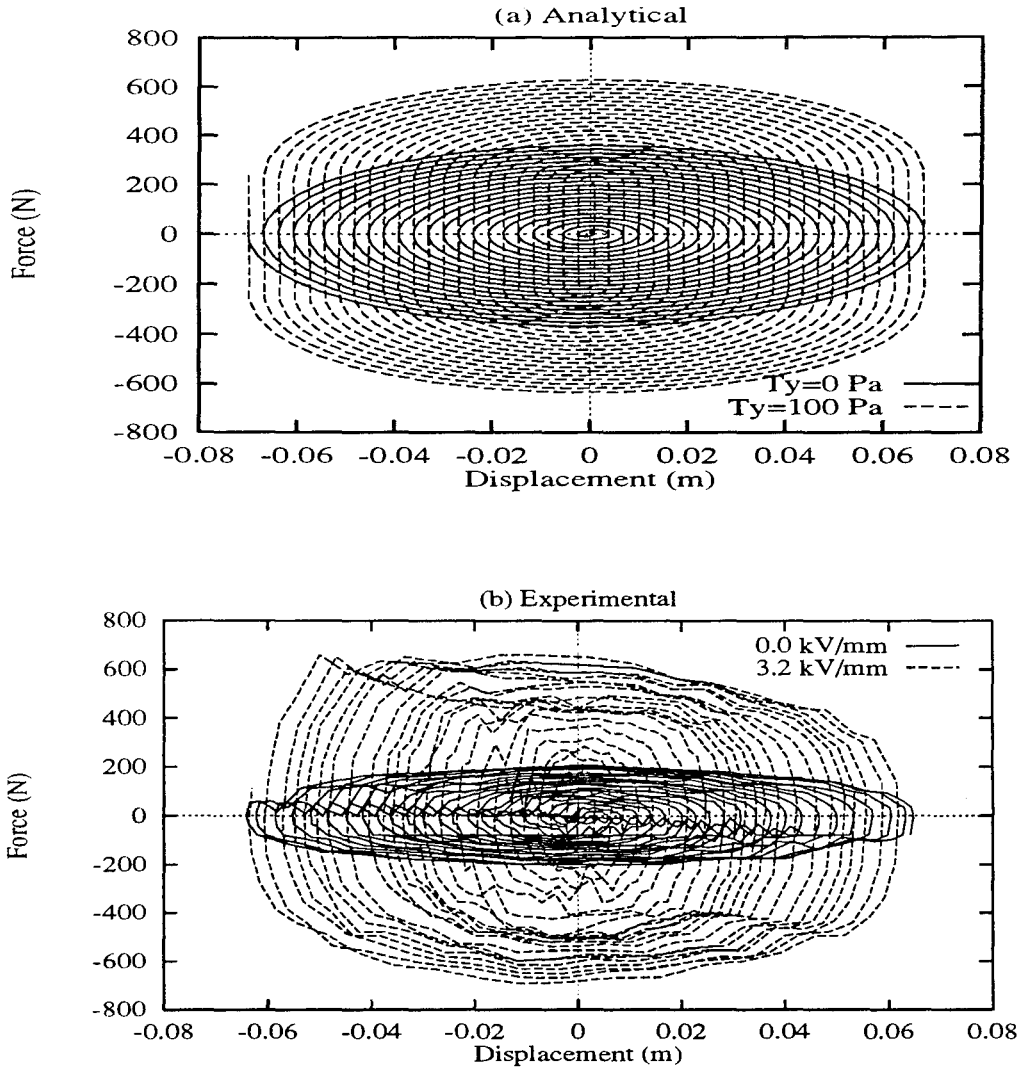

Figure 6.26: (a) Analytical and (b) experimental hysteresis loops for an electro-rheological damper at low and high electric fields.

illustrated in Figure 6.27. For this error analysis $I = J = K$ and $P = Q = R$.

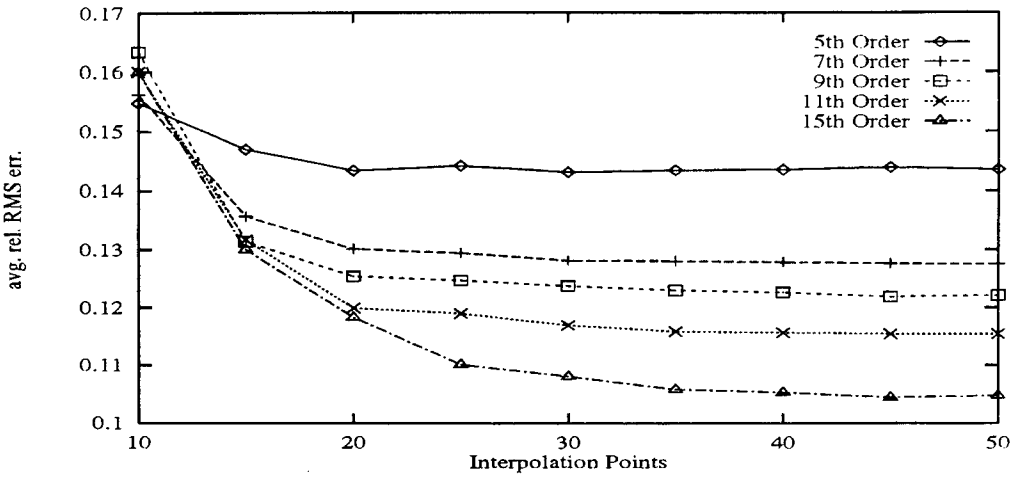

Figure 6.27: Convergence of $\hat{f}$ to f with increasing I, J, K and P, Q, R.

The error decreases monotonically with increasing I, J, K and increasing P, Q, R. Based on these results and the computation time required to evaluate higher degree polynomials, 50 interpolation points were used to curve-fit an 11^{th} degree polynomial in the x and $\dot{x}$ dimensions.

To visualize these functions of three variables, surfaces can be plotted for constant values for E. Figures 6.28 and 6.29 illustrate examples in the $x - \dot{x}$ plane of the data used for curve-fitting. Interpolated data $f(x, \dot{x})$ is shown as solid lines. The associated 11^{th} degree Chebyshev curve-fit is shown as dashed lines. Elevation conturs of the interpolated data and the curve-fit function are shown below the surfaces. These functions were fit using a zero degree polynomial in the E direction, and no data concerning E. Excellent agreement is achieved along the border of the $x - \dot{x}$ domain, but the error is greater near the origin of the domain. This non-uniform error is an artifact of the distribution of the zeros of $T_n(x)$ along x.[4] The behavior

[4]This demonstrates a case in which Chebyshev approximation is not a minimax approximation. This point is further developed in Appendix C.

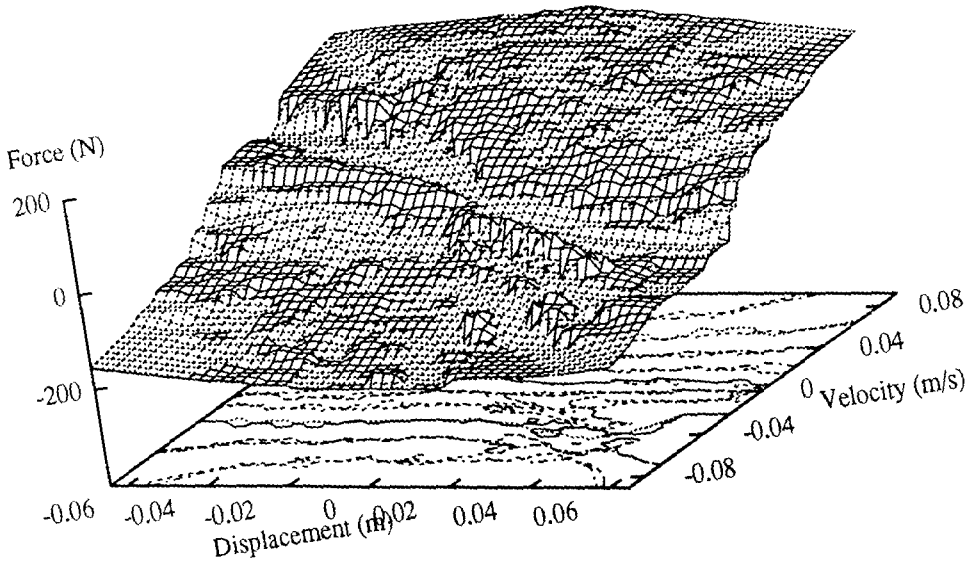

Figure 6.28: Non-parametric estimation of ER damper force (data—, curve-fit– –) 0.0 kV/mm

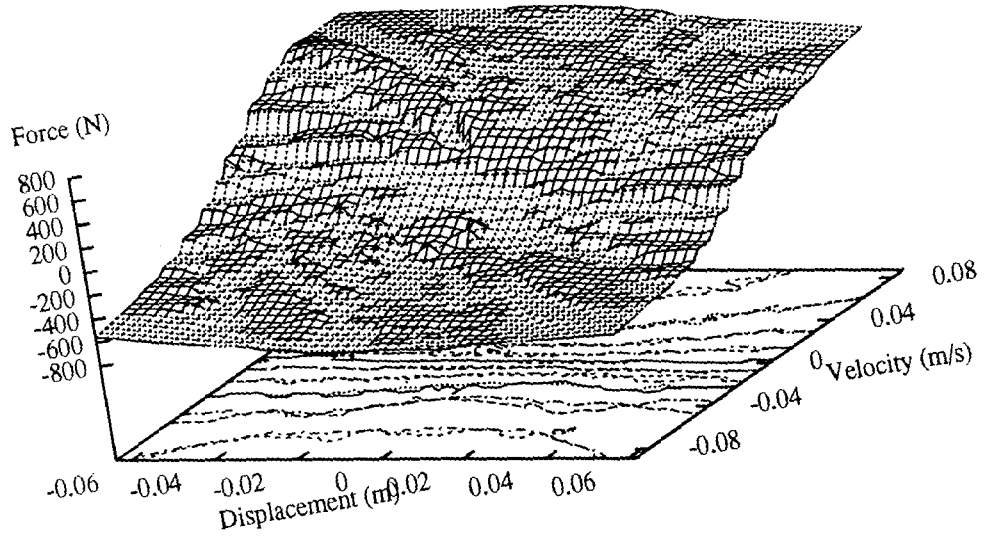

Figure 6.29: Non-parametric estimation of ER damper force (data—, curve-fit– –) 3.2 kV/mm

of the actual data between the zeroes is not accurately captured by a Chebyshev approximation. The slope $\partial f/\partial \dot{x}$ actually becomes quite steep near the origin of the $x - \dot{x}$ domain, but this feature is not captured by the Chebyshev curve-fit of 11^{th} degree. Figure 6.30 illustrates the error $(f - \hat{f})$ for the data at $E = 3.2$ kV/mm. In cases in which the function's behavior near the origin is relatively uninteresting

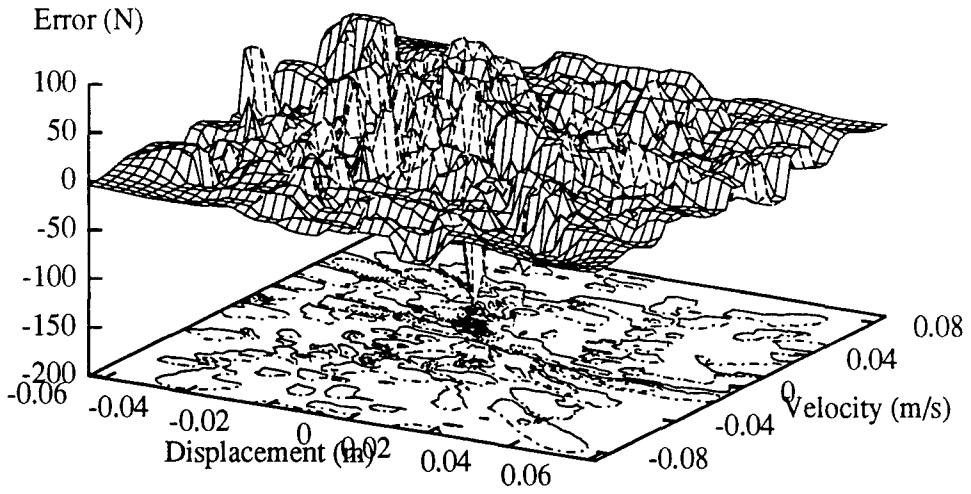

Figure 6.30: Error surface of $f(x, \dot{x}) - \hat{f}(x, \dot{x})$ at $E = 3.2$ kV/mm.

or unimportant, this is a desirable characteristic. In other cases, however, it may be more desirable to emphasize different regions of the domain. Approximation errors at larger displacements and velocities are less desirable than errors where the force levels are low $((x, \dot{x}) \approx (0, 0))$. Hence curve-fits using a Chebyshev polynomial basis accurately model the damper force as a function of the damper motion and the electric field.

In the second series of tests, data was collected at the same constant electric fields as in the first series, but the device motion was more irregular. Figure 6.31 illustrates

an example of these more irregular motions. The non-parametric model was then

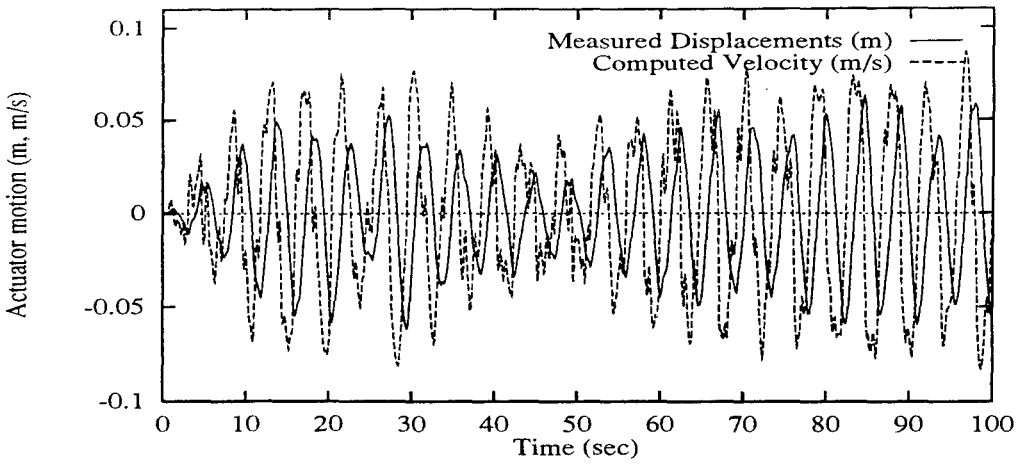

Figure 6.31: Irregular applied test motions for the large ER device at a constant electric field.

verified by comparing the curve-fit force, $\hat{f}$, (calculated using (5.6), the coefficients, C_{ijk} from the first set of data, and the coordinates $(x, \dot{x}, E)$ of the second set of data) to the measured force in the second set of data.

The 144 curve fit coefficients from each electric field data record were used to simulate the force measured in the second, less orderly, data set. The predicted ER force response is plotted with the measured data in Figures 6.32 and 6.33 for 0.0 kV/mm and 3.2 kV/mm. These figures illustrate the smoothing effects of interpolation and curve-fitting. Figure 6.34 illustrates the predicted and measured displacement hysteresis at 3.2 kV/mm. Again, the models shown in these figures were fit using a zero degree polynomial in the E direction, and no data concerning E.

As a final test of the modeling capabilities of the Chebyshev polynomial curve-fit, coefficients were calculated from the entire first data set except the data from the $E = 1.3$ kV/mm test. These coefficients were then used to simulate the force response from the $E = 1.3$ kV/mm test in the second data set. These results are

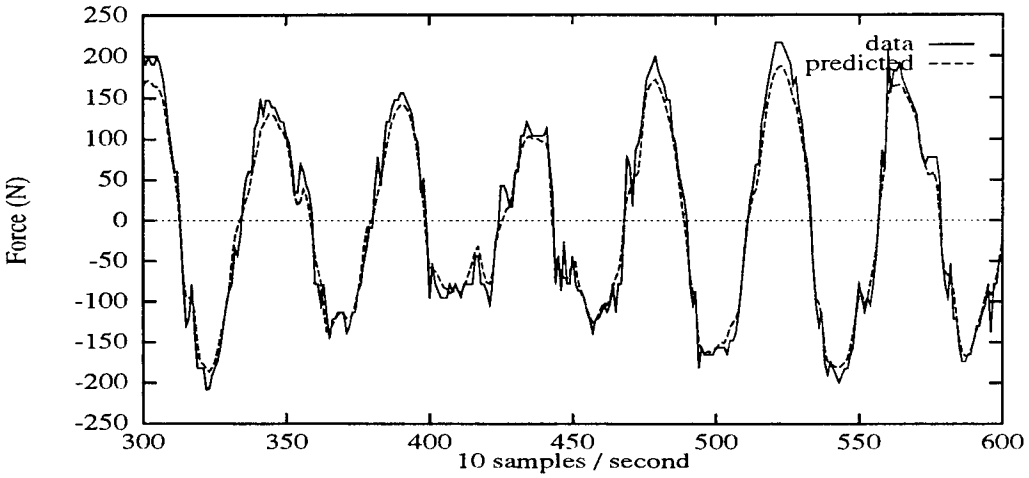

Figure 6.32: Prediction of ER forces based on a previous test at 0.0 kV/mm

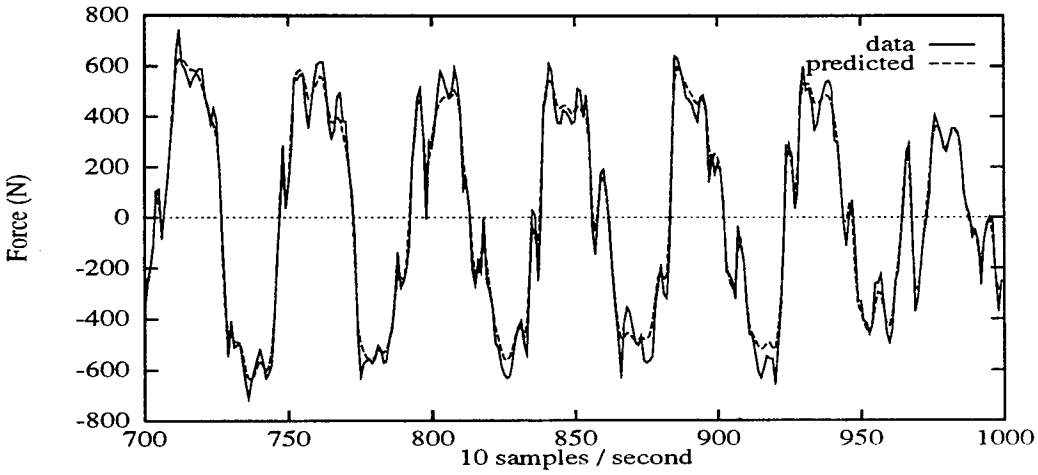

Figure 6.33: Prediction of ER forces based on a previous test at 3.2 kV/mm

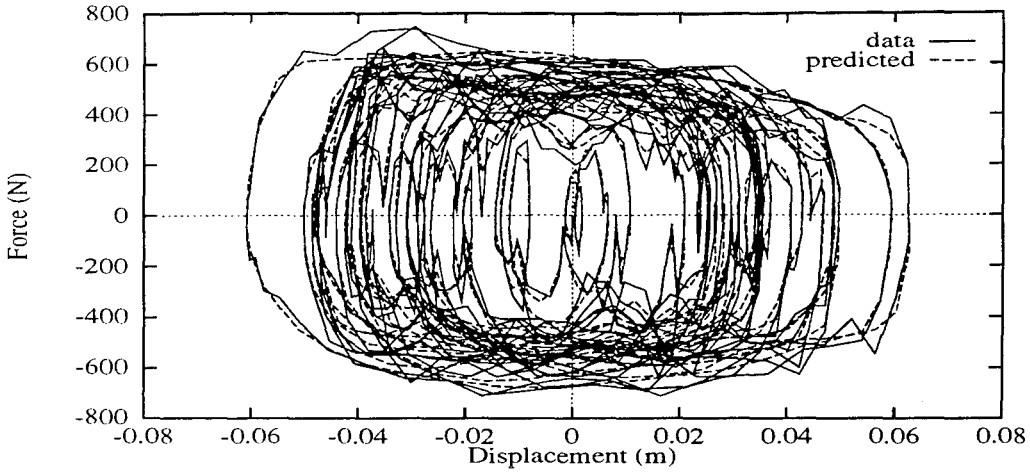

Figure 6.34: Prediction of ER displacement hysteresis based on a previous test at 3.2 kV/mm

shown in Figure 6.35. This last figure shows the ability of the model to accurately

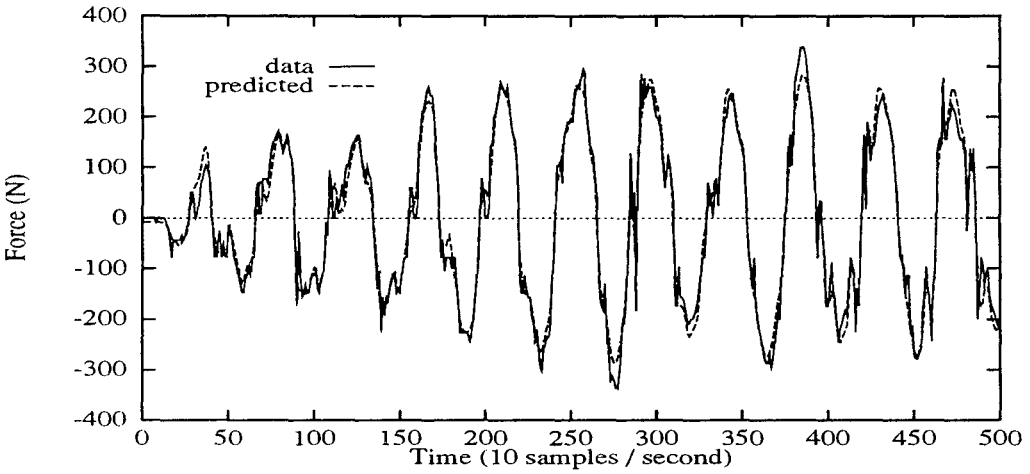

Figure 6.35: Prediction of ER damper forces at $E = 1.3$ kV/mm, based on tests at 0.0, 0.6, 1.9, 2.4, and 3.2 kV/mm.

interpolate data in the E direction. Because the nonlinear behavior of ER devices can not be accurately modeled using the Bingham-type relations, this non-dimensional approach is useful. A closed form approximation of the ER damper force, f, as a function of x, $\dot{x}$ and E can be used in simulation studies of the ER damper in a

structural control context.

6.4 Summary

Because the viscous stresses can not be controlled, it is desirable to minimize the viscous forces in an ER device in order to achieve the greatest dynamic range. Smaller viscous forces, however, lead to longer device response times in dash-pot style dampers. Data from an experimental study support the main features of these analytical results.

At low strains and strain rates, the visco-elastic and shear-thinning properties of ER material are more dominant than the yielding properties. For force level predictions, the Bingham model provides a simple and sufficiently accurate estimate for design purposes.

A multi-variable curve-fit results in a model which can accurately describe device-specific non-linearities, even though the calculated error does not exhibit minimax properties. This non-parametric model is intended for use in simulation of over-all device behavior.

ER devices capable of the force levels required for semi-active control of civil engineering structures can be constructed in reasonably-sized packages. The main attractions of these devices are their fast response times, low power requirements, lack of moving parts, and direct transduction of an electrical command signal to a mechanical force.

CHAPTER VII

SUMMARY AND CONCLUSIONS

7.1 ER Materials

Electrorheological (ER) materials exhibit remarkable changes in material properties when subjected to strong electric fields (kV/mm). However, ER behavior is complex. Primitive ER materials suffer from low levels of controllable stress (0–10 kPa), high current densities (kW of electrical power for kN of mechanical force), arcing, and irreversible sedimentation of the particulates over time. The effect of constitutive material properties such as: particle size, morphology, stoichiometry, ion concentration, permittivity, and dielectric loss need further study in order to develop better models for the ER effect and processing procedures for strong and reliable ER materials.

Many deficiencies of primitive ER materials have been addressed and mitigated by advances in the particulates and in processing. Anhydrous zeolite ER materials draw negligible currents (10^{-12} Amp/cm^2). Better mechanical properties accompany these improved electrical properties. Recently developed anhydrous ER gels settle slowly and can not pack into sedimentary layers. Mechanical, chemical, and electrical treatment of device surfaces may be a promising method toward improving yield stresses by an order of magnitude.

A Voigt linear visco-elastic model qualitatively describes the behavior of ER materials at pre-yield strains. Shear thinning behavior is observed in colloidal ER gels at higher strains and at shear rates up to 50/sec; and a yielding mechanism dominates ER behavior at shear rates greater than ≈500/sec. In steady, fully developed flow, the behavior of ER materials approaches that of a Bingham fluid, in which an applied shear stress, τ, is resisted by a yielding component, τ_y, and a viscous component, $\eta\dot{\gamma}$,

$$\tau(E,\theta) = \tau_y(E,\theta)\mathrm{sgn}\dot{\gamma} + \eta(E,\theta)\dot{\gamma}, \tag{7.1}$$

where E and θ indicate an electric field and temperature dependence. Assumptions implicit in the Bingham approximation are:

- The material does not deform in the pre-yield region.
- In the post-yield region, the flow of the material is fully developed.

While oscillating flows contradict these assumptions, the Bingham model's simplicity makes it attractive for rough calculations of the force capacity of ER devices.

7.2 Semi-Active Damping Devices

In order to take full advantage of ER materials in vibration control devices, their strengths (as well as their limitations) must be understood. Many independent geometric and kinematic design parameters can be adjusted to optimize the behavior of these devices in terms of dynamic range, response time, force level, volume of ER fluid, and voltage level. Balancing these performance metrics with respect to the available design variables is the basis of ER device designs.

7.2.1 Design

Most ER damping devices dissipate energy by forcing fluid through narrow (0.5 mm< h <3 mm) ducts, energized with high electric fields (1 kV/mm< E <6 kV/mm). The

analysis of such devices requires a relationship between the pressure gradient along the flow, $\frac{\partial p}{\partial x}$, and the volumetric flow rate Q, the duct wall velocity U, and material properties, τ_y and η. In fully developed flow, the fluid shear stress varies linearly across the duct. If $\tau < \tau_y$, the deformation rate, $\dot{\gamma}$, is zero, assuming ideal Bingham plastic behavior. For a prescribed flow rate, Q, and wall velocity, U, there exists a pair of coordinates, y_1 and y_2, at which $\tau(y) = \pm\tau_y$, as is shown in Figure 3.1. Between these coordinates, the ER material does not shear, but moves as a 'plug'. Note that a continuous range of shear rates and stresses are present in Poiseuille flows. For flow in dash-pot style devices, U/Q is a positive constant related only to the geometry of the device.

Continuity and equilibrium conditions for steady Bingham duct flow were cast into the form of a non-dimensional fifth order polynomial by Phillips in 1969 [220].

$$P^3 - (1+3T)P^2 + 4T^3 + P^2V + \frac{P^2TV^2}{3(P-2T)^2} = 0. \tag{7.2}$$

The dimensionless variables in (7.2) are described in Chapter III. Analytical, numerical, and approximate solutions to (7.2) for dash-pot style devices ($0 < V < 1/2$) are presented in Appendix B. The expression

$$P(T,V) = 1 + 2.07T - V + \frac{T}{1+0.4T} - \frac{1.5TV^2}{1+0.4T^2} \pm 3\% \tag{7.3}$$

uniformly approximates the desired root of (7.2) in these cases. Also, the flow transient resulting from an instantaneous and entire loss of yield stress is analyzed. These solutions are used in Chapter III to develop performance functions relating the dynamic range of an ER device and its response time to the dimensions of the device. These analyses predict that the dynamic force range of dash-pot devices increases exponentially with the ratio of the gap width to plunger width. The increase in dynamic range is afforded at the expense of the device's response times.

Small scale experiments, discussed in Chapter VI, were used to evaluate these design equations. The dynamic range predicted by the design equations were quantitatively confirmed by the tests. The response times of the small scale devices qualitatively followed the trends predicted by the design equation. The slow sample rates of the current data acquisition (200 samples/second) system precluded a quantitative analysis of response times. As expected, the non-Newtonian (shear-thinning) and colloidal nature of ER gels with $E = 0$ led to poor agreement between the theory of Chapter III and the test results at low shear rates. While the predicted force magnitudes were confirmed by the small scale tests, these tests also showed that at low strains and low strain rates mechanisms not modeled by the Bingham equation were dominant.

7.2.2 Modeling

Pre-yield, visco-elastic, and shear thinning material behavior complicate the behavior of ER devices. While the Bingham model results in simplified design equations for ER devices, it is inadequate for modeling them. Given a table of simultaneously measured forces f, device displacements, x, velocities $\dot{x}$, and electric fields, E, closed form polynomial approximations of the form $\hat{f}(x, \dot{x}, E)$ and $\hat{E}(x, \dot{x}, f)$ can be derived. This non-parametric modeling technique results in device-level, predictive models for

- the damper force as a function of the damper motion and voltage and
- the voltage required to produce a desired force as a function of the damper motion.

These models are useful for

- device simulation, and

- feed-back linearization.

Chebyshev polynomial basis functions were used. Using an orthogonal basis simplifies the calculation of the polynomial coefficients of a least squares approximation. Under certain conditions described in Appendix C, least squares approximation using Chebyshev polynomials approaches a minimax (uniform) approximation.

To gain experience in using ER devices for large scale applications, and to develop a data base for evaluating the non-parametric modeling technique, a large scale (2 gallon capacity) ER device was designed, constructed and tested. Cyclic test motions and constant electric fields were applied to the device. Force levels compared favorably with the analytical model. The non-parametric model succeeded in capturing the details of the hysteretic response, and was used to verify the repeatability of the experiments. The non-parametric model did not appear to provide a minimax approximation to the data.

7.2.3 Control

Using members with variable stiffness and damping to control structures is a parametric control problem. The applied electric field and device motions are nonlinearly related to the resisting forces in ER devices. To take advantage of the inherent simplicity of ER devices (no moving parts), simple control algorithms should be implemented. A number of bang-bang control rules, i.e., clipped pseudo-skyhook, are under consideration.

Because ER devices require only nominal amounts of power for operation, device forces are not included in the controller performance function. A decentralized, bang-bang control strategy has been derived to minimize the structural vibrational energy entering from measured ground motions [190]. To control randomly excited

vibration, the voltage must be applied and discharged at high duty-cycle rates. To take advantage of the fast (10^{-3} sec) material response times, control calculation time-delays should be as small as possible. Analog circuitry can implement this and other bang-bang control rules, and can apply high electric fields as required.

7.3 Future Work

7.3.1 ER Flow in a Concentric Annulus

The work to date has focused on flows in a rectangular gap. Flow through a concentric annulus is significantly harder to analyze (due to the lack of symmetry across the gap) but significantly more important. Sealing requirements in cylindrical devices are easily satisfied with O-rings. Rectangular devices require at least a few gasket seals, which are not as reliable as O-rings. If the device is made of several concentric annuli, the flow rate through each annulus will vary according to the fluid resistances in the annuli. These two issues probably preclude a closed form solution of the Navier-Stokes equations of the Bingham flow. The solution to this problem is under-way.

7.3.2 Horizontal Flow with a Free Surface

Another important device configuration entails a free-surface. In this configuration, a prismatic plunger translates *horizontally* through an open box. Fluid will be pumped between the plunger and the box wall, resulting in Poiseuille flow. These *viscous shear walls* have been implemented in full scale building damping applications [193]. The advantages of these device are:

- They can be constructed with no seals.

- The large surface areas can produce large forces, even if the stresses in the fluid are small.

However, sloshing effects significantly complicate this problem. Using viscous or dense fluids could mitigate this problem. The no-seal and large force design of such a device warrants an analysis of its behavior.

Because of the importance of the pre-yield, small deformation, region of ER materials, (as illustrated in the small scale experiments of Chapter VI) the effects of the pre-yield, visco-elastic behavior will be included in these analytical models.

7.3.3 Structural Control Experiments

The purpose of using ER devices in civil engineering structures is to improve structural safety and performance by controlling the response to dynamic loads. To evaluate the use of ER devices in semi-active vibration control, small scale shaking table tests are proposed.

A single-axis, servo-hydraulic shaking table is being constructed. ER devices for controlling a SDOF and a 3DOF shear building structure model are in design. Due to its simplicity of design and fabrication, an ER shear wall device will be implemented first. The simplicity of the ER shear wall allows for modifications of the device as the knowledge base generated by the shaking table tests grows. A self-contained implementation of the ER device, sensors, controller hardware, and power supply is envisioned. The building vibration control system will not require: external power, accumulators, valves, hoses, seals, digital signal processing, or centralized decisions.

Initially the device will be placed at the first floor level. The control strategy under consideration allows for distributed devices, along the height of the structure. Distributed semi-active actuation is envisioned in these experiments. The electronic

hardware developed to date allows for several direct state feed-back bang-bang control rules to be assessed.

Issues of controller-structure interaction (due to fluid inertia), high-voltage grounding techniques, and eventual battery-supply implementation, will be addressed in this phase of the work.

Many variable damping control rules have been suggested in the literature [4, 50, 65, 89, 90, 107, 121, 130, 131, 133, 143, 145, 146, 152, 155, 163, 169, 171, 184, 186, 190, 198, 201, 217, 289, 305]. Whether these controllers improve the performance of an *optimally* passively dampened system is, however, an unresolved issue. This project will rigorously assess the performance of the controlled structure as compared to the performance of a structure with optimal constant passive damping.

APPENDICES

APPENDIX A

Point Dipole Interactions and Dielectric Polarization of Spheres

A.1 Interaction Energy of Two Aligned Point Dipoles of Identical Strength

Consider two charge concentrations of opposite polarity, $\pm q$, separated by a distance a. By definition, the dipole moment, p, equals aq, and is oriented from $-q$ to $+q$. A polar coordinate system is centered at the midpoint of a line segment connecting these charges. The position angle, φ, is taken with respect to the line through the charges. The electrostatic potential, $\Phi(r, \varphi)$, at a point (r, φ), follows from Coulomb's law [283], as the sum of the potentials from each charge, $+q$ and $-q$. The independent variable r is the distance from the origin to a point.

$$\Phi = \frac{1}{4\pi\epsilon_0}\left(\frac{q}{r_+} - \frac{q}{r_-}\right), \tag{A.1}$$

where r_+ and r_- are the distances to $+q$ and $-q$, and ϵ_0 is the permittivity of free space ($8.854 \times 10^{-12}\mathrm{C}^2/\mathrm{Nm}^2$).[1] Figure A.1 illustrates this configuration. In the limit as $(a/r) \to 0$, $(r_+ r_-) \to r^2$ and $(r_- - r_+) \to a\cos\varphi$. In charge configurations in which $a/r \sim 1$, the electrostatic potential is commonly expanded in terms of

[1] The following units are equivalent: $[\mathrm{C}^2/\mathrm{Nm}^2]$= [F/m]=[C/V/m].

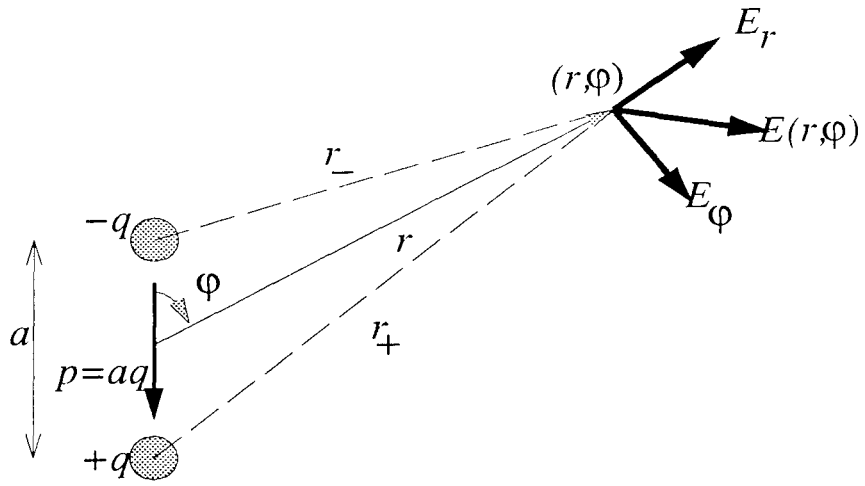

Figure A.1: The electric field, $E(r,\varphi)$, due to a point dipole, $p = aq$.

Legendre polynomials, $P_n(\cos\varphi)$ [59]. These polynomials are closely related to the law of cosines, required to solve for Φ when $a/r \approx 1$. Each term in this expansion corresponds to a higher order multi-pole. Since ER materials in a pre-yield condition have $a/r \approx 1$, neglecting these higher order multi-pole terms has led to order of magnitude under-estimates of the stresses in many studies. Indeed, a starting point for modeling ER behavior should include both the higher order multipoles of each particle and the combined field interaction effects of adjacent particles.

Proceeding with the point-dipole approximation ($a \ll r$), the potential at a point (r,φ) is

$$\Phi(r,\varphi) = \frac{aq}{4\pi\epsilon_0}\frac{\cos\varphi}{r^2}. \tag{A.2}$$

The electric field is the negative gradient of the electrostatic potential. In polar coordinates,

$$E(r,\varphi) = -\frac{\partial}{\partial r}\Phi(r,\varphi)\hat{r} - \frac{\partial}{\partial\varphi}\Phi(r,\varphi)\hat{\varphi} \tag{A.3}$$

where $\hat{r}$ and $\hat{\varphi}$ are unit normal vectors. Substituting (A.2) into (A.3) leads to

$$E(r,\varphi) = -\frac{p}{4\pi\epsilon_0 r^3}\left(2\cos\varphi\hat{r} + sin\varphi\hat{\varphi}\right). \tag{A.4}$$

This expression for the field has two components, perpendicular and parallel to the position vector (r, φ).

To obtain the point dipole pair interaction energy, place another dipole at the point (r, φ), aligned with the first point dipole, as illustrated in Figure A.2. The

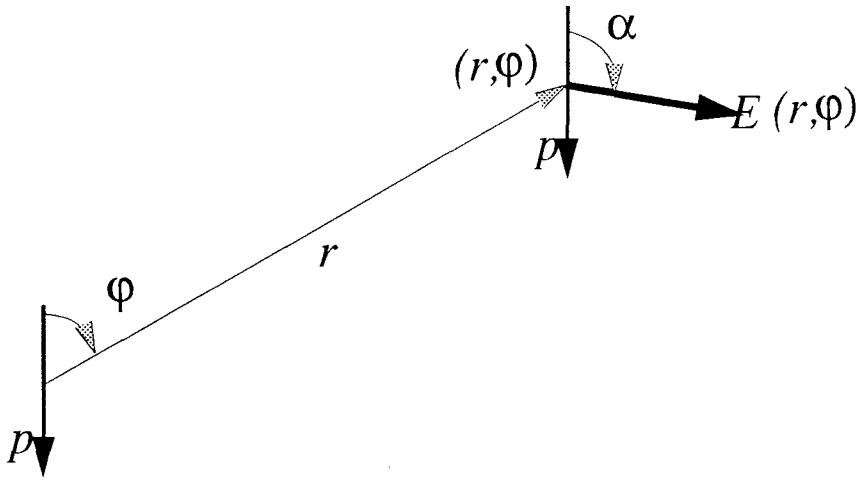

Figure A.2: Two aligned point dipoles.

interaction energy of two aligned point dipoles is the potential energy of one point dipole in the electrostatic field caused by the other [59]. Since a is assumed negligible with respect to r, the field is assumed uniform across the dipole charges. Again, this is not a good assumption for fibrated ER materials. For the condition $(a \ll r)$, however, the potential energies of $+q$ and $-q$ with respect to the coordinate r cancel identically. The remaining potential energy is associated with the torque, Γ, on the point dipole. The electric field is defined by $F = qE$, where F is the force on a charge q in a field E. If α is the angle between the electric field $E(r, \varphi)$ and a dipole p at (r, φ), then the torque on the dipole is

$$\Gamma = pE \sin \alpha, \tag{A.5}$$

and the potential energy, u, of the dipole is defined by $\int \Gamma d\alpha$ and simplifies to

$$u = -|p||E| \cos \alpha, \tag{A.6}$$

Substituting (A.4) into (A.6) leads to the desired relation

$$u(r, \varphi) = -\frac{p^2}{4\pi\epsilon_0 r^3} \left(3\cos^2 \varphi - 1\right). \tag{A.7}$$

The theoretical variation of the interparticle forces with φ is illustrated in Figure 2.1

The same result can be quickly obtained using coordinate independent vector notation.

$$\Phi = \frac{\vec{p} \cdot \vec{r}}{|r|^3}, \tag{A.8}$$

$$\vec{E} = -\nabla\Phi = -\left[\frac{\vec{p}}{|\vec{r}|^3} - \frac{3(\vec{p} \cdot \vec{r})}{|\vec{r}|^4}\hat{r}\right], \tag{A.9}$$

$$u = -\vec{p} \cdot \vec{E} = \frac{\vec{p} \cdot \vec{p}}{|\vec{r}|^3} - \frac{3(\vec{p} \cdot \vec{r})(\vec{p} \cdot \vec{r})}{|\vec{r}|^4}\hat{r}. \tag{A.10}$$

This expression reduces to (A.7) in the case of polar coordinates.

A.2 Dielectric Polarization of Spheres

The polarization of a sphere in a mis-matched dielectric continuum requires the solution of Laplace's equation with the appropriate boundary conditions. The solution outlined by von Hippel [283] is summarized here.

Laplace's equation for the potential is $\nabla^2\Phi = 0$. Trial functions for the potential outside the sphere, Φ_o, and inside the sphere, Φ_i follow the form

$$\Phi_o = \left(\frac{A}{r^2} + Br\right) \cos \varphi, \tag{A.11}$$

and

$$\Phi_i = \left(\frac{C}{r^2} + Dr\right) \cos \varphi. \tag{A.12}$$

The potential at the sphere's surface ($r = a/2$) is C^1 (continuous to the first derivative),

$$\Phi_o(a/2) = \Phi_i(a/2), \tag{A.13}$$

and

$$k_f \frac{\partial \Phi_o}{\partial r}(a/2) = k_p \frac{\partial \Phi_i}{\partial r}(a/2), \tag{A.14}$$

where k_f and k_p are the dielectric constants of the continuum and the sphere. The potential infinitely far from the sphere is un-perturbed and it is finite within the sphere. The coefficients determined from these boundary conditions result in a uniform electric field within the sphere, and a perturbation to the field outside the sphere which decays with r^{-3}. The electric field inside the sphere, E_i, is related by a factor β to the field infinitely far from the sphere, E_o.

$$E_o - E_i = \left(\frac{k_p - k_f}{k_p + 2k_f} \right) \epsilon_0 E_o, \tag{A.15}$$

where β is the term in parenthesis. The dipole moment per unit volume is $(k_p - k_f)E_i$ and the dipole moment for the entire sphere is

$$p = \frac{1}{2} \pi a^3 k_f \epsilon_0 \beta E_o. \tag{A.16}$$

The boundary conditions discussed above, however, do not accurately describe the conditions in fibrated ER materials. The field near the particle surface is concentrated by a factor of 10–20, due to the presence of neighboring particles [54]. If water, salts, or other ionic impurities exist in the dispersant, the field-induced dipole formed by interfacial polarization will almost completely mask the dipole formed by bulk polarization of the particle [93]. The dielectric constant of the particle, in this case, is almost meaningless. Furthermore, amorphous ER particles have a convoluted morphology.

Because the above assumptions regarding a/r, polarization mechanisms, and the external electric field are not representative of ER fluids, the point-dipole pair interaction model can not quantitatively describe ER phenomena. Better models for describing ER phenomena have focused on improving the assumption on a/r [156, 157, 158], and the electric field configuration [32, 33, 54]. Some of these kinematic models have successfully described the behavior of certain ER materials. None of these models address the irregular shapes of ER particles and how the morphology influences polarization and the ER effect.

The mechanism by which the dipoles form is important to the ER effect. An understanding of this mechanism, and an ability to control it, appears to be an obstacle to the wide-spread commercial application of ER materials. To date, no good polarization model has been found. In fact, a single model for polarization mechanisms probably does not exist for every ER material. ER materials, like composites in general, encompass a range of solutions and suspensions. Only through intensive study of the physics and chemistry of the particles, dispersants, and their synergetic effects will ER materials achieve their commercial potential.

In summary, point dipole approximations for the ER effect lead to errors because

- higher order multipoles are important,
- electric fields are not uniform near the particles,
- the polarization vectors of the particles are not always aligned,
- the particle's dielectric constant, k_p is meaningless if polarization is accomplished by mobile ions in the dispersant, and
- many particles are not spherical, but have mobile ions which reside in deep

canyons on the particle's surface.

APPENDIX B

Solution of the Poiseuille Flow Equations

B.1 Analytic Solution for Fixed Walls

The cubic equation relating the pressure gradient along the flow of a Bingham fluid in a narrow duct with fixed walls, ($p' = -\frac{\partial p}{\partial x}$) to the flow rate, Q, viscosity, η, and the yield stress, τ_y, is [220]

$$P^3 - P^2(1 + 3T) + 4T^3 = 0, \tag{B.1}$$

where the non-dimensional pressure gradient is

$$P = \frac{p'}{p'_N} = \frac{bh^3 p'}{12Q\eta} \tag{B.2}$$

and the non-dimensional yield stress is

$$T = \frac{\tau_y}{p'_N h} = \frac{bh^2 \tau_y}{12Q\eta}. \tag{B.3}$$

The pressure gradient p', is normalized by the pressure gradient of a Newtonian fluid, p'_N, with the same viscosity, the same flow rate, and through the same duct. Equation (B.1) is cubic in both the pressure gradient and the yield stress. Similar methods can be used to solve (B.1) for P or T. The solution $P(T)$ is required for simulation of Bingham flow given the properties of the fluid (τ_y and η) and the flow,

Q. The flow rate between plates in a device is usually determined by assuming incompressibility and solving a mass conservation equation. The solution $T(P')$ is required for identification of the fluid yield stress given η, Q, and p'. The flow rate and pressure gradient are measurable properties; η can be determined from tests on the ER fluid at $E = 0$. The implicit assumption is that η is independent of E. Solving for η and τ_y as a function of Q and p' requires numerical methods. Numerical methods are also required to solve the equations describing flow between moving plates (general Poiseuille flow). A numerical method based on the simplex method to solve these problems, and closed form uniform approximations are presented in following sections.

B.1.1 Simulation: $P(T)$

The solution of (B.1) for P follows a procedure outlined by W.H. Beyer [25]. The cubic equation (B.1) can be transformed into an expression of the form

$$x^3 + a_1 x + a_2 = 0 \tag{B.4}$$

by the substitution

$$P = x + \frac{1}{3}(1 + 3T). \tag{B.5}$$

The coefficients in (B.4) are then

$$a_1 = -\frac{1}{3}(1 + 3T)^2 \tag{B.6}$$

$$a_2 = -\frac{2}{27}(1 + 3T)^3 + 4T^3. \tag{B.7}$$

The trigonometric identity

$$4\cos^3\theta - 3\cos\theta - \cos(3\theta) \equiv 0. \tag{B.8}$$

can be used to solve (B.4) for x by substituting

$$x = m\cos\theta \tag{B.9}$$

into (B.4) and equating coefficients. Carrying out these steps leads to

$$m = \frac{2}{3}(1 + 3T) \tag{B.10}$$

and

$$\theta_1 = \frac{1}{3}\arccos\left(1 - \frac{54T^3}{(1+3T)^3}\right) \tag{B.11}$$

Solutions $\theta = \theta_1$, $\theta = \theta_1 + \frac{2\pi}{3}$, and $\theta = \theta_1 + \frac{4\pi}{3}$ are the three roots of (B.4). If the argument of the arccos() in (B.11) is not in the interval [-1,1], then some or all of the roots are complex [25]. Re-applying the substitutions (B.9) and (B.5) leads to the three roots

$$P_1(T) = \frac{2}{3}(1+3T)\left[\cos\left(\frac{1}{3}\arccos\left(1 - 54\left(\frac{T}{1+3T}\right)^3\right)\right) + \frac{1}{2}\right] \tag{B.12}$$

$$P_2(T) = \frac{2}{3}(1+3T)\left[\cos\left(\frac{1}{3}\arccos\left(1 - 54\left(\frac{T}{1+3T}\right)^3\right) + \frac{2\pi}{3}\right) + \frac{1}{2}\right] \tag{B.13}$$

$$P_3(T) = \frac{2}{3}(1+3T)\left[\cos\left(\frac{1}{3}\arccos\left(1 - 54\left(\frac{T}{1+3T}\right)^3\right) + \frac{4\pi}{3}\right) + \frac{1}{2}\right] \tag{B.14}$$

after some simplification. The behavior of $P_1(T)$ is representative of a flowing Bingham fluid, ($P > 1$ for every $T > 0$). $P_2(T)$ and $P_3(T)$ are less than 1 over a portion of the domain $T > 0$. The expression

$$P(T) \approx 1.0 + 2.07T + \frac{T}{1 + 0.4T} \tag{B.15}$$

uniformly approximates $P_1(T)$ over the range $0 < T < 1000$, and is somewhat easier to evaluate than $P_1(T)$. A comparison of this approximation to the exact solution of the cubic (B.1) is illustrated in Figure B.1. Examples of the error in the approximation (B.15) are illustrated in Figure B.2. These errors are uniformly less than 2% and are much smaller over significant regions of the domain $0 \leq T \leq 1000$. The errors become very small for $T \ll 1$.

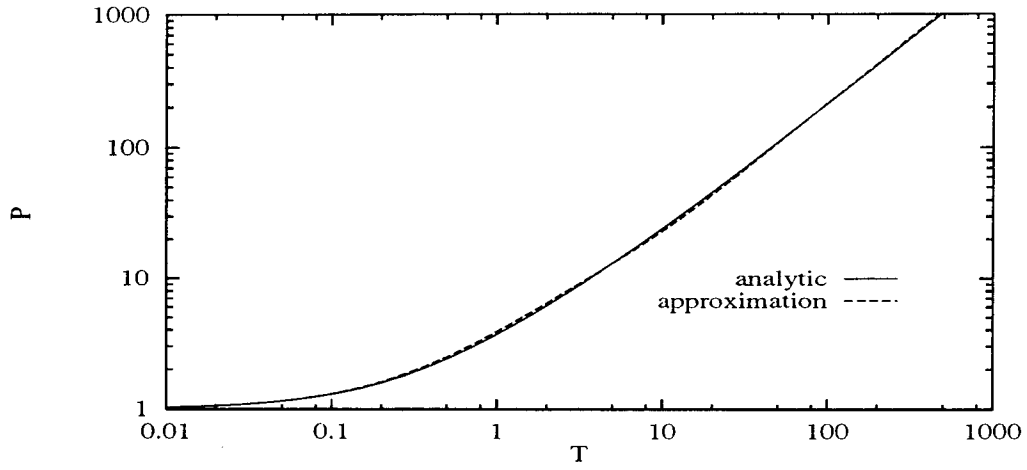

Figure B.1: Variation of dimensionless pressure gradient, P, with yield stress, T. Solid line: exact, Dashed line: approximation

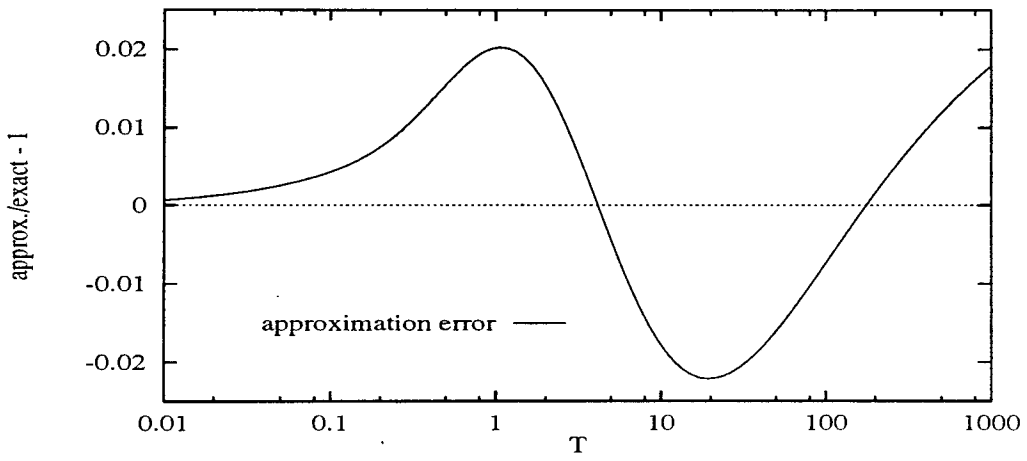

Figure B.2: Approximation errors of $P \approx 1 + 2.07T + T/(1 + 0.4T)$ to the exact solution, $P_1(T)$.

B.1.2 Identification: $T(P)$

Equation (B.1) can be expressed as

$$T^3 - \frac{3}{4}P^2T + \frac{1}{4}P^3 - 14P^2 = 0, \tag{B.16}$$

which is in the same desired form as (B.4) for the trigonometric substitution (B.9). The coefficients of (B.4) are simply

$$a_1 = -\frac{3}{4}P^2 \tag{B.17}$$

$$a_2 = \frac{1}{4}(P^3 - 3P^3) \tag{B.18}$$

Substituting $T = Pcos\theta$ into (B.16) and equating coefficients with (B.8) leads to

$$\theta_1 = \frac{1}{3}\arccos\left(\frac{1}{P} - 1\right) \tag{B.19}$$

Evaluating $T = Pcos\theta$, and recognizing the periodicity of T in θ, leads to the three real roots

$$T_1(P) = P\cos\left(\frac{1}{3}\arccos\left(\frac{1}{P} - 1\right)\right) \tag{B.20}$$

$$T_2(P) = P\cos\left(\frac{1}{3}\arccos\left(\frac{1}{P} - 1\right) + \frac{2\pi}{3}\right) \tag{B.21}$$

$$T_3(P) = P\cos\left(\frac{1}{3}\arccos\left(\frac{1}{P} - 1\right) + \frac{4\pi}{3}\right) \tag{B.22}$$

Using the fact that $P > 1$, bounds can be placed on the roots of (B.16).

$$\frac{P}{2} \leq T_1 \leq \frac{\sqrt{3}P}{2} \tag{B.23}$$

$$-P \leq T_2 \leq -\frac{\sqrt{3}P}{2} \tag{B.24}$$

$$0 \leq T_3 \leq \frac{P}{2} \tag{B.25}$$

$$\tag{B.26}$$

The yield stress, τ_y, is specified as a non-negative quantity. For $T > P/2$, the shear stress in the fluid is nowhere greater than τ_y, and there is no flow. In steady flows,

the pressure gradient is constant and the shear stress profile is linear between the plates, with a slope equal to p'. Because the walls are fixed, the shear flow profile is symmetric. So the maximum stress in the fluid is at the walls and is equal to $hp'/2$. Therefore, $(T/P) > (1/2) \Longleftrightarrow \tau_y > (hp'/2)$. Equation (B.1) describes only *flowing* Bingham fluids. T_3 is therefore the desired root. Calculating τ_y using (B.22) requires that η is known. If η is not known accurately, then τ_y calculated using (B.22) can be in error by as much as 100%. Using the zero-field viscosity as an estimate of η and assuming that η is not field dependent has nevertheless given good results in estimating τ_y in some ER fluids [40]. The errors associated with this assumption are probably fluid-dependent.

B.2 Numerical Solutions and an Approximation for Moving Walls

The equation describing the flow of Bingham fluids between parallel, but moving walls,

$$P^3 - (1+3T)P^2 + 4T^3 + P^2V + \frac{P^2TV^2}{3A^2} = 0 \tag{B.27}$$

is a fifth order polynomial in P, and has no analytic solution for the roots $P(T, V)$. The non-dimensional pressure gradient, P, and yield stress, T, are the same as in (B.2) and (B.3). The non-dimensional wall velocity, V, is the ratio of the flow rate for a shear flow to the flow rate of the Bingham Poiseuille flow,

$$V = \frac{Q_s}{Q} = \frac{bhU}{2Q}, \tag{B.28}$$

where U is the wall velocity. The dimensionless excess pressure, A,

$$A = P - 2T \tag{B.29}$$

is the pressure gradient in excess of the pressure gradient required to yield the Bingham material. Equation (B.27) reduces to (B.1) when $V = 0$ (fixed walls).

Equation (B.27) describes Bingham flow only for certain values of V, [220]

$$|V| \leq \frac{3A^2}{P}. \tag{B.30}$$

Equations for other values of V are given by (3.17), (3.18), and (3.19). In a dash-pot style damper, V is fixed by the damper geometry. Consider the flow between the outer plates and the case of the damper illustrated in Figure 4.3. If the plates are moving with a velocity U with respect to the case, the mean flow rate between the plates, with respect to the plates, is

$$Q = U\left(1 + \frac{N}{N+1}\frac{t}{h}\right)hb, \tag{B.31}$$

assuming equal partition of flow. In (B.31) N is the number of plates, t is the plate thickness, and h is the gap between the plates. Substituting U/Q from (B.31) into (B.28), and recognizing that N, t, and h can not be negative, leads to bounds on V.

$$0 \leq V = \frac{1}{2}\frac{1}{\left(1 + \frac{N}{N+1}\frac{t}{h}\right)} \leq \frac{1}{2}. \tag{B.32}$$

Solutions to (B.27) satisfy (B.30) for $0 < V < 0.5$ [220]. This will be shown at the end of the next section. Therefore the plug in mixed mode damping devices using Bingham materials is never attached to the plates or the case, and the flow is described by (B.27).

B.2.1 Simulation: $P(T, V)$

In typical ER damper geometries, $0.1 < V < 0.3$. In this range of V the behavior of the desired root of (B.27) is smooth in the $T - V$ plane. See Figure B.3. So given a good estimate of the bounds on the solution $P(T, V)$, (B.27) can be solved

using simple numerical methods. The method used here simply uses a lower bound on $P(T,V)$ and increases P until (B.27) and (B.30) are satisfied to within a pre-specified tolerance. The smallest possible value of P corresponds to the case $T = 0$ (Newtonian flow). Substituting $T = 0$ into (B.27) gives $P = 1 - V$. The solution for the case $V = 0$ is also known and is uniformly approximated by (B.15). The expression for the lower bound of $P(T,V)$ was therefore chosen to be

$$P(T,V) > \max\left[0.5 - V, 0.5 - V + 2T + \frac{T}{1+T}\right]. \tag{B.33}$$

Numerical experiments with this solution method led to a uniform approximation for $P(T,V)$ in the range $0 \leq V \leq (1/2)$.

$$P(T,V) \approx 1 + 2.07T - V + \frac{T}{1+0.4T} - \frac{1.5TV^2}{1+0.4T^2}. \tag{B.34}$$

A comparison of this approximation to the "exact" numerical solution of the fifth order polynomial (B.27) is illustrated in Figure B.3. It is clear from Figure B.3 that the desired solution to (B.27) varies smoothly with T and V for damper devices ($0 \leq V \leq (1/2)$). Examples of the error in the approximation (B.34) are illustrated in Figure B.4. These errors are slightly biased, but are uniformly less than 4%. The errors become very small for $T \ll 1$. This approximation is not at all valid outside of the range $0 \leq V \leq (1/2)$. Omitting the term $1.5TV^2/(1+0.4T^2)$ will make the approximation accurate for $-\infty < V \leq 0$. But for $(1/2) < V$, an approximation of a different form is required.

The inequality (B.30) can now be checked. Substituting $A = P - 2T$ into (B.30), expanding the quadratic, setting the right hand side of the quadratic equal to (1/2), and solving for P, leads to two relations between P and T. For the solution of (B.27) to be valid, the root must lie outside of the region bounded by these two relations.

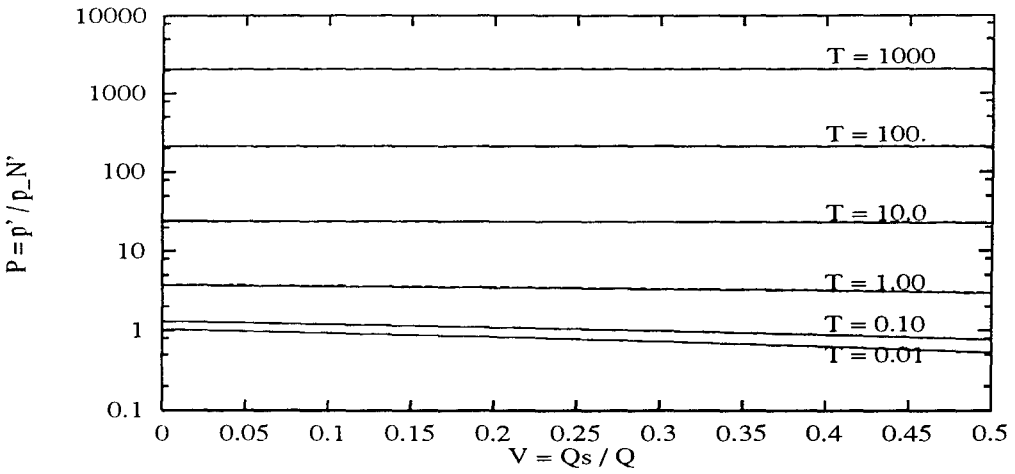

Figure B.3: Variation of dimensionless pressure gradient, P, with wall velocity, V, and yield stress, T. —: numerical solution, - - - -: closed form approximation

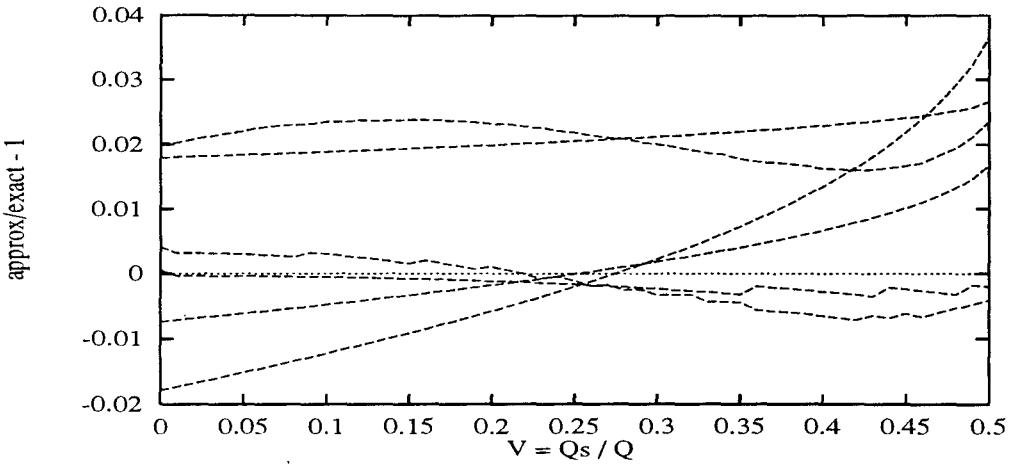

Figure B.4: Approximation errors of $P \approx 1 - V + 2.07T + \frac{T}{1+0.4T} - \frac{1.5TV^2}{1+0.4T^2}$ to the numerical solution.

This is demonstrated in Figures B.5 and B.6 over the range $0 \leq T \leq 1000$ and $0 \leq V \leq (1/2)$.

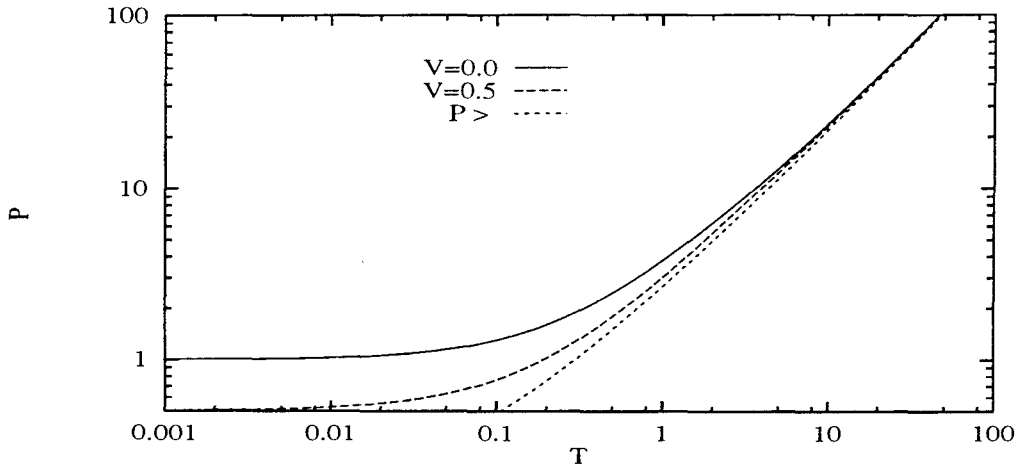

Figure B.5: Verification of the inequality $|V| \leq \frac{3A^2}{P}$ for small T. $\frac{1}{2} < \frac{3A^2}{P}$ when $P(T,V)$ is above the line labeled: $P >$ - - - -.

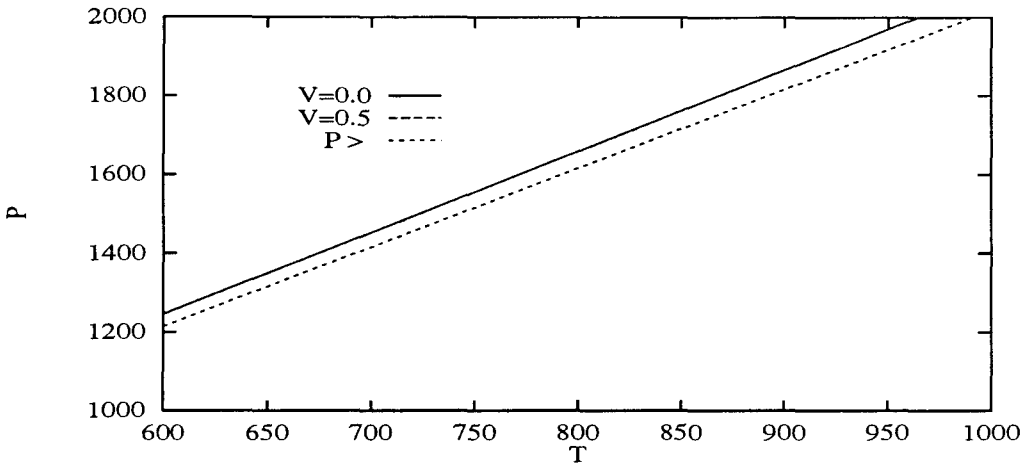

Figure B.6: Verification of the inequality $|V| \leq \frac{3A^2}{P}$ for large T. $\frac{1}{2} < \frac{3A^2}{P}$ when $P(T,V)$ is above the line labeled: $P >$ - - - -.

B.2.2 Identification: $T(P,V)$

The numerical solution of (B.27) for T is analogous to the solution procedure for P. The expression for the lower bound of $T(P,V)$ was chosen to be the analytic root

of (B.1) for T ($T_3(P)$), plus $V/4$.

$$T(P,V) > \max\left[0, P\cos\left(\frac{1}{3}\arccos\left(\frac{1}{P}-1\right)+\frac{4\pi}{3}\right)+\frac{V}{4}\right]. \qquad \text{(B.35)}$$

To converge upon the exact root, T is increased until (B.27) and (B.30) are satisfied to within a pre-specified tolerance. In numerical experiments, this initial guess was usually within 5% of the "exact" numerical answer. While the ability to identify the yield stress from flow measurements is desirable, it is more useful to be able to identify both the yield stress and the viscosity. The variation of η on E in some ER fluids is most significant at low values of E [36, 38, 43], whereas in other fluids, η appears to be a constant, or a function of temperature alone [47].

B.3 Estimating Parameters τ_y and η from Experimental Data

The yield stress τ_y and the viscosity η both can not be uniquely determined from a single equation (B.1) or (B.27). However, given two (or more) "measurements" of Q, V, and p', estimates for τ_y and η may be found. Hence, the identification problem with τ_y and η unknown represents a system of two or more nonlinear equations. Usually one desires to estimate physical parameters from experimental data. Because all measurements contain some noise, estimation problems are commonly formulated as the minimization of the sum of errors squared $\sum e^2$ (least squares estimation). The goodness of fit criterion, is then, $J(\eta,\tau_y) = \sum e(\eta,\tau_y)^2$, and the minimization problem seeks to minimize J by adjusting η and τ_y. Numerical minimization procedures iteratively move the coordinate (η,τ_y) down the slope of the surface $J(\eta,\tau_y)$ until a minimum is reached. A pitfall common to many minimization methods is that the minimum converged upon is only a local minimum, and that the desired (global) minimum lies elsewhere. This problem is especially pernicious if the error, e, to be minimized is a polynomial of the parameters, such as (B.1) or (B.27), with a plurality

of real roots. There is no guarantee that the minimization will not converge upon a "wrong" root. Of course, if the minimization procedure is started near the desired solution, the converged upon minimum will probably be the "right" one. But a robust parameter estimation method should be insensitive to the initial guess. To side-step this potential problem, the approximation (B.34) was chosen to be model the damper behavior. This equation closely approximates the dependence of the desired root on η and τ_y, is simpler than (B.27), and in numerical experiments identified η and τ_y accurately.

The parameter estimation problem can be formalized as follows. Given M measurements of the wall velocity U_m, flow rate Q_m, and pressure gradient p'_m, $(m = 1, ..., M)$, minimize the function $J(\eta, \tau_y) = \sum e_m^2$, where

$$e_m = 1 - P_m - V_m + 2.07T_m + \frac{T_m}{1 + 0.4T_m} - \frac{1.5T_m V_m^2}{1 + 0.4T_m^2}, \tag{B.36}$$

and P_m, T_m, and V_m are the previously defined dimensionless quantities evaluated with U_m, Q_m, and p'_m. A variety of methods exist for solving nonlinear minimization problems [222, 226]. The procedure implemented in this study is a nonlinear analogue of the simplex method, used to solve linear programming problems [226].

This estimation method gives better results when $\frac{\tau_y}{\eta\dot{\gamma}}$ is small. The method is also sensitive to noise on the measurements. In a simulation of a mixed mode damper, the pressure gradient responding to sinusoidal damper motions was calculated, assuming ideal Bingham behavior. The yield stress was ramped from 1 kPa to 0 kPa and the viscosity was kept constant at 0.5 Pa-sec over the course of the simulation. One thousand data points (U, Q, p') were simulated. Parameters were estimated from two sets of data. The first set had no noise, and the second set had one percent Gaussian white noise. These simulated measurements are shown in Figures B.7 and

B.8. Parameters τ_y and η were estimated using $M = 20$ points of data at a time.

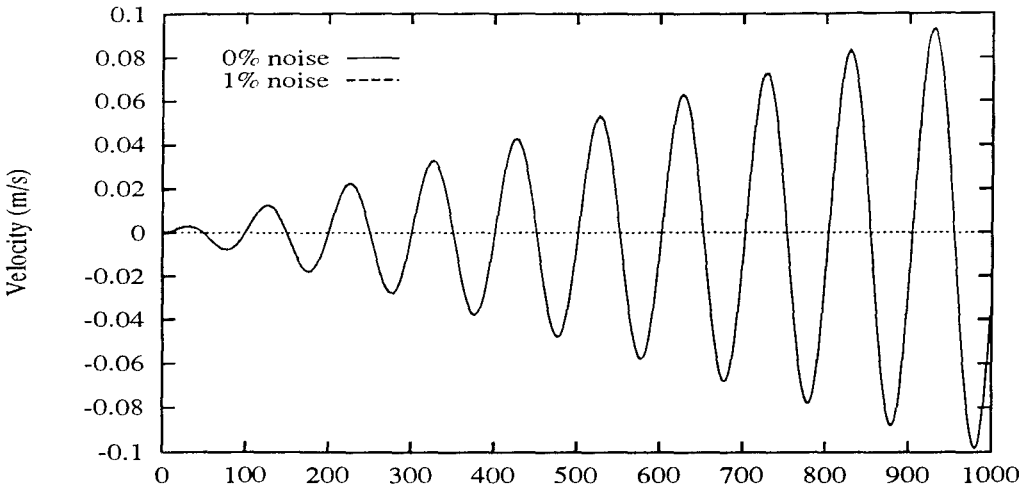

Figure B.7: Damper velocity for the parameter estimation

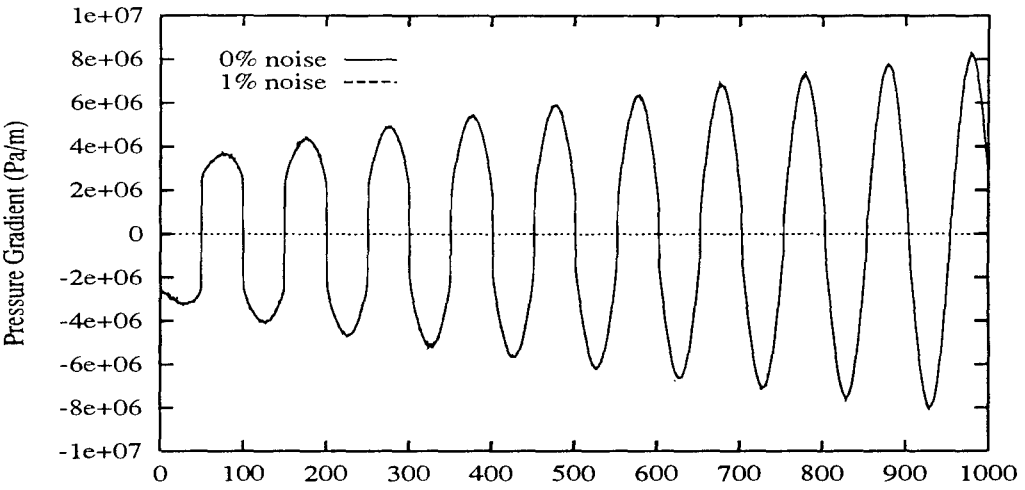

Figure B.8: Calculated pressure gradient

The simulated and estimated yield stress and viscosity are shown in Figures B.9 and B.10. The characteristics of this parameter estimation method are:

- The parameter estimates become more accurate as the damper velocity is increased and as the yield stress is decreased. Parameters estimated from regions of data where the viscous stress is small in comparison to the yield stress are

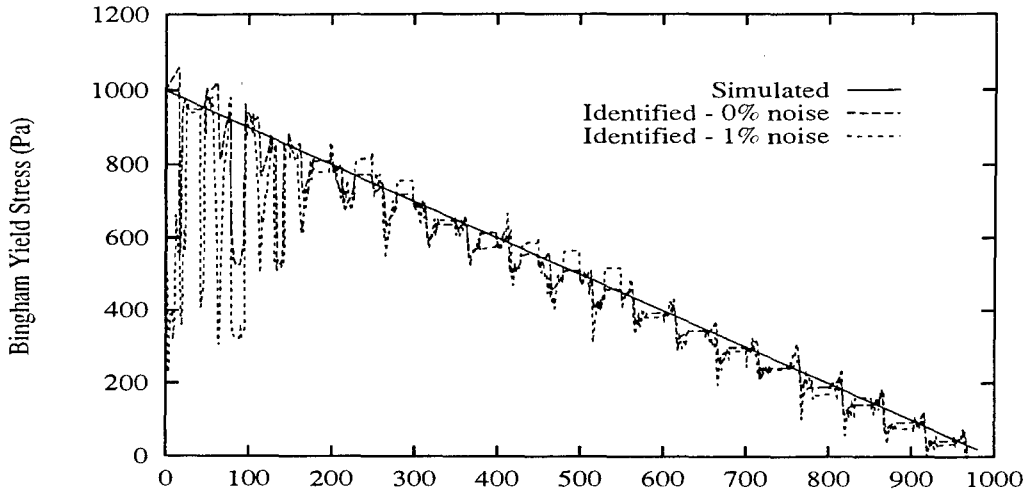

Figure B.9: Identified Yield Stress, τ_y.

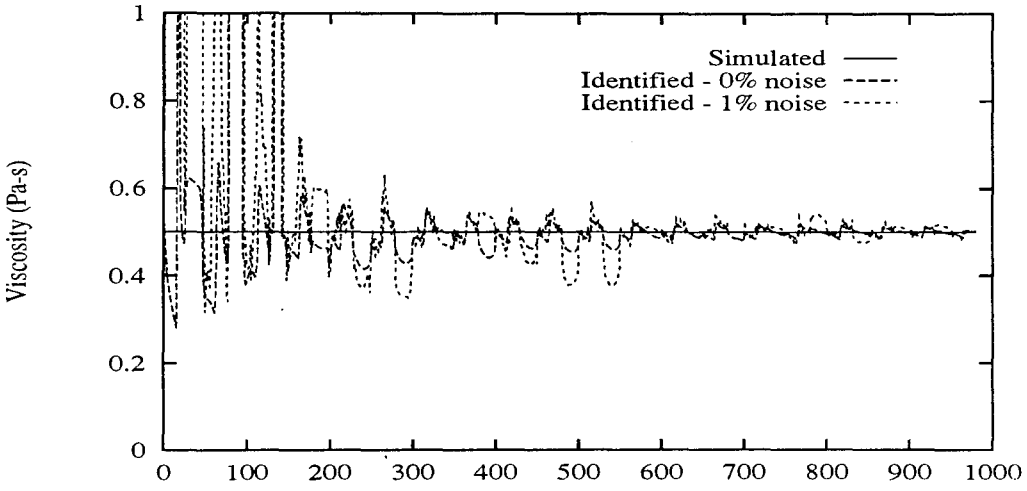

Figure B.10: Identified viscosity, η

not at all close to the values used in the simulation.

- This parameter estimation method is sensitive to noise. Measurement noise as low as 1 percent can influence the estimated parameters significantly.

B.4 Summary

The flow of a Bingham fluid through a rectangular duct can be described by a cubic equation if the walls are fixed and a fifth order polynomial if the walls are moving. An exact solution of the cubic equation can be used to calculate the pressure gradient or the yield stress, given all the other properties of the flow. A simple quadratic expression relating the material and flow properties to the pressure gradient is accurate to within 2 percent, over wide ranges of the yield stress. The flow of a Bingham fluids in a dash-pot style device is described by the fifth order polynomial. The flow rate to wall velocity ratio is fixed by the damper geometry in dash-pot style devices. This fact restricts the domain of the desired solution of the fifth order polynomial. This root can be found using a simple numerical method, given a reliable estimate of its lower bound. A lower bound making use of the approximate solution of the cubic equation works well. A simple closed-form expression relating the material and flow properties to the pressure gradient is accurate to within 3%, over a wide range of yield stresses and wall velocities.

Estimating the yield stress *and* the viscosity from pressure and flow measurements of a Bingham flow between parallel plates is more difficult. Least squares methods are favored when estimating parameters from noisy measurements. One such method estimates the yield stress and viscosity more accurately when the yield stresses are small in comparison to the viscous stresses. This method is expected to work better with high shear rate data.

APPENDIX C

A Note on Chebyshev Polynomials

Chebyshev polynomials are frequently discussed in the context of uniform, or minimax approximation. The desirable characteristic of a minimax approximation is that it is as accurate in one part of the domain as in any other part of the domain. The error criterion of a uniform approximation is the infinity norm, $||e||_\infty$, whereas the error criterion of a least-squares approximation is the Euclidean norm, $||e||_2$. Coefficients of a polynomial approximation are usually found by minimizing the error criterion in the space of polynomial coefficients. The attraction of the Euclidean norm is that this minimization can be done by setting the derivatives of the criterion with respect to the coefficients equal to zero, and solving for the coefficients. The difficulty of finding the minimax approximation is that $||e||_\infty$ is not generally differentiable [98].

Consider a function $f(x)$ continuously evaluable on $x \in \Omega$. An N^{th} degree approximation $\hat{f}_N(x)$ for $f(x)$ on Ω can be of the form

$$\hat{f}_N(x) = \sum_{i=0}^{N} c_i \phi_i(x) \tag{C.1}$$

where c_i are constant coefficients of the approximation and $\phi_i(x)$ are basis functions mutually orthogonal over $x \in \Omega$. That is,

$$\int_\Omega \phi_i(x)\phi_j(x)dx = \begin{cases} ||\phi_i||_2^2 & \text{if } i = j \\ 0 & \text{if } i \neq j \end{cases} \tag{C.2}$$

The coefficients c_i of the approximation $\hat{f}_N$ satisfy a minimum norm property on Ω. Two such norms are the least squares norm and the minimax norm. The least squares norm, J_2, is defined by

$$J_2(\bar{c}) = \int_\Omega (f(x) - \hat{f}_N(x))^2 dx \tag{C.3}$$

The set of $N+1$ equations, $\frac{\partial J_2}{\partial c_i} = 0$, results in a system of linear equations for the coefficients c_i. These equations are un-coupled if the error criterion recognizes the orthogonality of the basis functions.

The minimax norm, J_∞, is defined by

$$J_\infty(\bar{c}) = \max_{x \in \Omega}(|(f(x) - \hat{f}_N(x)|) \tag{C.4}$$

In general, the least squares approximation, $\hat{f}_N$ of f, does not minimize (C.4). Nothing in the development so far implies that a least squares approximation approaches the minimax property. If, however,

1. extreme values of the basis functions, $\phi_i(x)$ are either +1 or −1,

2. adjacent extreme values of $\phi_i(x)$ have opposite signs, and

3. the error $e_N(x)$ to the N^{th} degree approximation (C.1) is dominated by $c_{N+1}\phi_{N+1}(x)$,[1]

then the error of the N^{th} degree approximation (C.1) is roughly uniform. Whether this approximation minimizes (C.4) is not clear.

In choosing Chebyshev polynomials, conditions (1) and (2) are satisfied at the expense of emphasizing the accuracy of the curve-fit near the boundary of the domain Ω. Condition (3) is not guaranteed by the choice of basis functions, and depends largely upon the data and the number of terms in the approximation. When approximating functions whose behavior is not captured by function evaluations at discrete

[1] In other words, $c_{N+1} \gg c_i \forall i > N+1$.

points, a truncated approximation may not be uniformly accurate. Because evaluation points for a Chebyshev approximation are more widely spaced near the center of the domain, non-uniform errors can be expected if the function is not adequately sampled, and the curve-fit is of insufficient order. In this case, approximating with other polynomials, such as Legendre or Forsythe, may result in a more uniform error, or an error which is small where desired.

BIBLIOGRAPHY

BIBLIOGRAPHY

[1] Adriani, Paul M. and Gast, Alice P., "A microscopic model of electrorheology" *Physics of Fluids* **31**(10), (Oct. 1988): 2757–2768.

[2] Adriani, Paul M. and Gast, Alice P., "Electric-field-induced Aggregation in Dilute Colloidal Suspensions" *Faraday Discussions Chemical Society* **90** (1990): 17–29.

[3] Agrawal, A.K., Fujino, Y. and Bharitia, B.K., "Instability Due to Time Delay and Its Compensation in Active Control of Structures" *Earthquake Engineering and Structural Dynamics* **22** (1993): 211–224.

[4] Akbay, Zekal and Aktan, Haluk M., "Vibration control of Building Structures by Active Energy Dissipation" *Proc. U.S. Nat'l Workshop on Structural Control Research,* 25–26 Oct. 1990, USC, Los Angeles, CA, (USC Publication No. CE-9013): 74–79.

[5] Aldersey-Williams, Greg, "A solid future for smart fluids" *New Scientist* (17 March 1990): 37–40.

[6] Amato, Ivan, "Smart as a Brick" *Science News* **137** (10 Mar. 1990): 152–155.

[7] Anaskin, I.F., Gleb, V.K., Korobko, E.V., Khizhinskii, B.P. and Khusid, B.M., "Effect of External Electric Field on Amplitude-Frequency Characteristics of Electrorheological Damper" *J. Engineering Physics* **46** (1984): 233–238.

[8] anon. "Electro-rheological fluids: Solid Results" *The Economist* (5 Dec. 1987): 94.

[9] anon. "Electrorheological Fluids" *Engineering* (Feb. 1988): i–iv.

[10] anon. "Smart fluids could form a new kind of hydraulics" *Machine Design* (23 Jun. 1988): 12.

[11] anon. "Liquid Assets" *Discover* (Sept. 1988): 8+.

[12] anon. "MSU researchers announce 'smart' materials" *Materials Performance* **26** (Sep. 1988): 67.

[13] anon. "Smart fluids control hydraulic equipment" *Radio Electronincs* **60** (Spt. 1989): 4.

[14] anon. "Solid fluids that give a softer ride" *The Engineer* (2 Nov. 1989): 45.

[15] anon. "When is a fluid not a fluid?" *The Engineer* (14–28 Dec. 1989): 37–39.

[16] anon. "Composites get smart" *Engineering* (Mar. 1990): ACE 21–22.

[17] anon. "FP industry facing innovation gap" *Machine Design* (12 Jul. 1990): 36–37.

[18] anon. "Rheology Update" *Hydraulics & Pneumatics* (Nov. 1991): 10.

[19] anon. "Animating the Material World" *Science* **255** (Jan. 1992): 284.

[20] anon. "Electric Jell-O" *Technology Review* (Apr. 1993): 80.

[21] Arguelles, J., Martin, H.R. and Pick, R., "A Theoretical Model for Steady Electroviscous Flow Between Parallel Plates" *J. Mechanical Engineering Science* **16**(4), (1974): 232–239.

[22] Atkin, R.J., Shi, Xiao and Bullough, W.A., "Solution of the constitutive equations for the flow of an electrorheological fluid in the radial configuration" *J. Rheology* **35**(7), (Oct. 1991): 1441–1461.

[23] Bangs, S., "Scientist Pioneers Electrohydraulic Modulation Using Winslow Effect" *Hydraulics and Pneumatics* (Sep. 1966): 146–148.

[24] Batchelor, G.K., "The stress system in a suspension of force-free particles" *J. Fluid Mechanics* **41**(3), (1970): 545–570.

[25] Beyer, William H., *ed. CRC Standard Mathematical Tables, 27th ed.*, (Boca Raton, FL: CRC Press, Inc., 1984).

[26] Bhadra, D.K., Harder, C.R. and Thompson, W.B., "Electroviscous Damping for Landing Aircraft" *Proc. 2nd Int'l Conf. on ER Fluids* 7–9 Aug. 1989, Raleigh, NC. (Lancaster: Technomic Publishing Co.): 402–408.

[27] Block, H. and Kelly, J.P., "Electrorheological Fluids" *UK Patent 8,503,581* (1986).

[28] Block, H. and Kelly, J.P., "Review Article: Electro-rheology" *J. Physics D: Applied Physics* **21** (1988): 1661–1677.

[29] Block, H., Kelly, J.P., Qin, A., and Watson, T., "Materials and Mechanisms in Electrorheology" *Langmuir* **6** (1990): 6–14.

[30] Block, H. "Electrorheological fluids" *Chemtech* (Jun. 1992): 368.

[31] Bonnecaze, R.T. and Brady, J.F., "Dynamic Simulation of a Suspension of Dielectric Particles Forming an Electrorheological Fluid" *Proc. 2nd Int'l Conf. on ER Fluids,* 7–9 Aug. 1989, Raleigh, NC. (Lancaster: Technomic Publishing Co.): 27–40.

[32] Bonnecaze, R.T. and Brady, J.F., "Yield stresses in electrorheological fluids" *J. Rheology* **36**(1), (Jan 1992): 73–115.

[33] Bonnecaze, R.T. and Brady, J.F., "Dynamic simulation of an electrorheological fluid" *J. Chemical Physics* **96**(3), (1 Feb. 1992): 2183–2202.

[34] Bossis, G. and Lemaire E., "Yield stresses in magnetic suspensions" *J. Rheology* **35**(7), (Oct. 1991): 1345–1355.

[35] Boyle, F.P., "Performance Characterization of ER Fluids: Durability" *Proc. Int'l Conf. on Electrorheological Fluids,* 15–16 Oct. 1991, Carbondale, IL, (Singapore: World Scientific): 236–245.

[36] Brooks, Doug A., "Electro-Rheological devices" *Chartered Mechanical Engineer* Sept. 1982, 91–93.

[37] Brooks, D., Goodwin, J., Hjelm, C., Marshal, L. and Zukoski, C., "Visco-Elastic Studies on an Electro-Rheological Fluid" *Colloids and Surfaces* **18** (1986): 293–312.

[38] Brooks, Doug A., "Fluids get tough" *Physics World* **2** (Aug. 1989): 35–38.

[39] Brooks, Doug A., "Devices Using Electro-Rheological Fluids" *Proc. 2nd Int'l Conf. on ER Fluids,* 7–9 Aug. 1989, Raleigh, NC. (Lancaster: Technomic Publishing Co.): 371–401.

[40] Brooks, Douglas Alan, "Design And Development Of Flow Based Electro-Rheological Devices" *Proc. Int'l Conf. on Electrorheological Fluids,* 15–16 Oct. 1991, Carbondale, IL, (Singapore: World Scientific): 367–397.

[41] Brooks, Douglas, "Applicability of Simplified Expressions for Design with Electro-Rheological Fluids" *J. Intelligent Material Systems and Structures* **4** (Jul. 1993): 409–414.

[42] Bullough, W.A., and Foxon, M.B, "A Proportionate Coulomb and Viscously Damped Isolation System" *J. Sound and Vibration* **56**(1), (1978): 35–44.

[43] Bullough, W.A. and Peel, D.J., "Progress Towards a Hydraulic Semiconductor for Vehicle Applications" *SAE paper 881786* (1988): 1–15.

[44] Bullough, W.A., "Miscellaneous Electro-Rheological Phenomena, Part I" *Proc. 2nd Int'l Conf. on ER Fluids,* 7–9 Aug. 1989, Raleigh, NC. (Lancaster: Technomic Publishing Co.): 115–123.

[45] Bullough, W.A., "Miscellaneous Electro-Rheological Phenomena, Part II" *Proc. 2nd Int'l Conf. on ER Fluids,* 7–9 Aug. 1989, Raleigh, NC. (Lancaster: Technomic Publishing Co.): 125–140.

[46] Bullough, W.A., "Electrorheological fluids and the control of high-speed machines" *Endeavour* **15**(4), (1991): 165–169.

[47] Carlson, J. David and Duclos, Theodore G., "ER Fluid Clutches and Brakes–Fluid Property and Mechanical Design Considerations" *Proc. 2nd Int'l Conf. on ER Fluids,* 7–9 Aug. 1989, Raleigh, NC. (Lancaster: Technomic Publishing Co.): 353–367.

[48] Ceccio, Steven L. and Wineman, Alan S., "Influence of Electric Field Orientation on Shear Flow of Electrorheological Fluids" *Electrorheological Flows* FED-Vol. **164** (ASME, 1993): 21–27.

[49] Chappell, P.H. and Campden, K.J., "Switching performance of power MOSFETS with capacitive loads at high frequency and high voltage for square wave generators" *Measurement Science Technology* **3** (1992): 356–361.

[50] Chassiakos, Anastassios G. and Masri, Sami F., "Vibration Control of Building Structures by Active Energy Dissipation" *Proc. U.S. Nat'l Workshop on Structural Control Research,* 25–26 Oct. 1990, USC, Los Angeles, CA, (USC Publication No. CE-9013): 103.

[51] Chen, Gun-Shing, Lurie, Boris J. and Wada, Ben K., "Active Member Control for Vibration Suppression in Truss Structures" *Intelligent Structures* (London: Elsevier Applied Science, 1990).

[52] Chen, Tian-jie, Zitter, R.N. and Tao, R., "Laser Diffraction Determination of the Crystalline Structure of an Electrorheological Fluid" *Physical Review Letters* **68**(16), (20 Apr. 1992): 2555–2558.

[53] Chen, Tian-jie, Zhang, Xuesong, Zitter, R.N., and Tao, R., "Deformation of an electrorheological chain under flow" *J. Applied Physics* **74**(2), (15 Jul. 1992): 942–944.

[54] Chen, Y., Sprecher, A.F. and Conrad, H., "Electrostatic particle-particle interactions in electrorheological fluids" *J. Applied Physics* **70**(11), (1 Dec. 1991): 6796–6802.

[55] Cheng, D.C.-H. and Richmond, R.A., "Some observations on the rheological behavior of dense suspensions" *Rheologica Acta* **17** (1978): 446–453.

[56] Cheng, D.C.-H., "Yield stress: A time-dependent property and how to measure it" *Rheologica Acta* **25** (1986): 542–554.

[57] Chenguan, W., "The Prospect of Engineering Applications of the Electro-Rheological Technique in China" *Proc. 2nd Int'l Conf. on ER Fluids,* 7–9 Aug. 1989, Raleigh, NC. (Lancaster: Technomic Publishing Co.): 349–352.

[58] Chenguan, W. and Aixia, W., "The Research in the Applications of ER Technology in Engineering" *Proc. Int'l Conf. on Electrorheological Fluids,* 15–16 Oct. 1991, Carbondale, IL, (Singapore: World Scientific): 465–409.

[59] Coelho, Roland, *Physics of Dielectrics* (Amsterdam: Elsevier, 1979)

[60] Conrad, H., Chen, Y. and Sprecher, A.F., "Electrorheology of Suspensions of Zeolite Particles in Silicone Oil" *Proc. 2nd Int'l Conf. on ER Fluids,* 7–9 Aug. 1989, Raleigh, NC. (Lancaster: Technomic Publishing Co.): 252–264.

[61] Conrad, H., Sprecher, A.F., Choi, Y. and Chen, Y., "The temperature dependence of the electrical properties and strength of electrorheological fluids" *J. Rheology* **35**(7), (Oct. 1991): 1393–1409.

[62] Conrad, Hans and Sprecher, Arnold F., "Characteristics and Mechanisms of Electrorheological Fluids" *J. Statistical Physics* **64**(5/6), (1991): 1073–1091.

[63] Conrad, H., "Electrorheological Fluids: Characteristics, Structure, and Mechanisms" *Electrorheological Flows* FED-Vol. **164** (ASME, 1993): 99–113.

[64] Coulter, J.P., Duclos, T.G. and Acker, D.N., "The Usage of Electrorheological Materials in Viscoelastic Layer Damping Applications," *Proc. Damping '89,* 8-10 Feb. 1989, West Palm Beach, FL (Wright-Patterson Air Force Base, Ohio: Wright Research & Development Center, Technical Report, TR-89-3116, Vol. I, 1989): CAA1–CAA17.

[65] Coulter, J.P. and Duclos, T.G., "Applications of Electrorheological Materials in Vibration Control" *Proc. 2nd Int'l Conf. on ER Fluids,* 7–9 Aug. 1989, Raleigh, NC. (Lancaster: Technomic Publishing Co.): 300–325.

[66] Coulter, J.P., "An Investigation of Electrorheological Material Based Controllable Damping Devices" *Electrorheological Flows* FED-Vol. **164** (ASME, 1993): 115–127.

[67] Coulter, J.P., Weiss, K.D. and Carlson, J.D., "Engineering Applications of Electrorheological Materials" *J. Intelligent Material Systems and Structures* **4** (Apr. 1993): 248–259.

[68] Davies, P., Popplewell, J., Martin, G., Bradbury, A., and Chantrell, R.W., "Monte Carlo simulations of the structure of magnetic fluid composites" *J. Physics D: Applied Physics* **19** (1986): 469–476.

[69] Davis, L.C., "Finite-element analysis of particle-particle forces in electrorheological fluids" *Applied Physics Letters* **60**(3), (20 Jan. 1992): 319–321.

[70] Davis, L.C., "Polarization forces and conductivity effects in electrorheological fluids" *J. Applied Physics* **72**(4), (15 Aug. 1992): 1334–1340.

[71] Davis, L.C., "The metal-particle/insulating oil system: An ideal electrorhological fluid" *J. Applied Physics* **73**(2), (15 Jan. 1993): 680–683.

[72] Dehghanyar, T.J., Masri S.F., Miller, R.K. and Caughey, T.K., "On-Line Parameter Control of Nonlinear Flexible Structures" *Structural Control: Proc. 2nd Int. Symp. on Structural Control* (Waterloo, Ontario: Martinus Nijhoff Publishers, 1985)

[73] Dienega, Yu. F. and Vinogradov, G.V., "Electric fields in the rheology of disperse systems" *Rheologica Acta* **23** (1984): 636–651.

[74] Demetriades, S.T., "Effect of Electrostatic Fields on the Orientation of Colloidal Particles Immersed in Shear Flow" *J. Chemical Phyics* **29**(5), (Nov. 1958): 1054–1063.

[75] Dem'yanov, V.F. and Malozemov, V.N., *Introduction to Minimax* (New York: Dover Press, 1990).

[76] Den-Hartog, Jacob Pieter, *Mechanical Vibrations* (New York: Dover Press, 1985).

[77] Department of Energy, *Electrorheological (ER) Fluids: A Research Needs Assessment Final Report* DOE/ER/30172 May 1993 (Oak Ridge, TN: Office of Scientific and Technical Information, 1993).

[78] Druchas, "Electroviscous Fluid Control Device" *U.S. Patent 4,790,522* (13 Dec. 1988).

[79] Duclos, Theodore G., "An Externally Tuneable Hydraulic Mount which Uses Electro-Rheological Fluid" *SAE paper 870963* (1987): 131–137.

[80] Duclos, Theodore G., "Design of Devices Using Electrorheological Fluids" *SAE paper 881134* (1988): 1–5.

[81] Duclos, Theodore G., "Inertia Type Fluid Mount Using Electrorheological and Other Fluid" *U.S. Patent 4,720,087* (19 Jan. 1988).

[82] Duclos, Theodore G., Acker, Debra N., and Carlson, L. David, "Fluids That Thicken Electrically" *Machine Design* (21 Jan. 1988): 42–46.

[83] Duclos, Theodore G., et al. "Tuneable Electrorheological Fluid Mount" *US Patent 4,733,758* (29 Mar. 1988).

[84] Duclos, Theodore G., "Electrorheological fluids and devices" *Automotive Engineering* **96**(12), (Dec. 1988): 45–48.

[85] Duff, A. Wilmer, "The Viscosity of Polarized Dielectrics" *Physical Review* **4**(10), (Mar. 1896): 23–39.

[86] Dunne, Jim, "Inside Detroit: Miracle Fluid" *Popular Mechanics* (Sep. 1988): 25.

[87] Ehrgott, R.C. and Masri, S.F., "Modeling the oscillatory dynamic behavior of electrorheological materials in shear" *Smart Materials and Structures* **1** (1992): 275–285.

[88] Evans, M.W. and Heyes, D.M., "Group Theory Statistical Mechanics and Simulation Studies of Electrorheology" *J. Physical Chemistry* **95** (1991): 5287–5292.

[89] Feng, Q., Fujii, S., Shinozuka, M. and Fujita, T., "Hybrid Isolation System Using Friction-Controllable Sliding Bearings" *Proc. 8th VPI & SU Symp. on Dynamics and Large Structures* 6–8 May 1991, Blacksburg, VA.

[90] Feng, Qing and Shinozuka, Masanobu, "Control of Seismic Response of Bridge Structures Using Variable Dampers" *J. of Intelligent Material Systems and Structures* **4** (Jan. 1993): 117–122.

[91] Filisko, Frank E. and Armstrong, W.E., "Electric field dependent fluids" *US Patent 4,744,914* (1988).

[92] Filisko, Frank E. and Radzilowski, Leonard H., "An intrisic mechanism for the activity of alumino-silicate based electrorheological materials" *J. Rheology* **34**(4), (May 1990): 539–552.

[93] Filisko, Frank E., "Materials in Electrorheology" Technical report, (1991), Department of Materials Science and Engineering, University of Michigan, Ann Arbor, MI.

[94] Filisko, Frank E., "Rheological Properties and Models of Dry ER Materials" *Proc. Int'l Conf. on Electrorheological Fluids,* 15–16 Oct. 1991, Carbondale, IL, (Singapore: World Scientific): 116–128.

[95] Filisko, Frank E., "Electrorheological Materials: Smart Materials of the Future" *Chemistry & Industry* (18 May 1992): 370–373.

[96] Filisko, Frank E. and Gamota, Daniel R., "Dielectric Studies of ER Systems Under High Bias Fields" *Electrorheological Flows* FED-Vol. **164** (ASME, 1993): 63–69.

[97] Filisko, Frank E., and Wang, Hwei-Rung, "The Dynamic Character of ER Materials" *Polymer Preprints* **35**(2) (Aug. 1994): 329–330.

[98] Forsythe, G.E., "Generation and Use of Orthogonal Polynomials for Data-Fitting with a Digital Computer" *J. Soc. Indust. Appl. Mathematics* **5** (2), (Jun. 1957): 74–87.

[99] Gamota, Daniel R. and Filisko, Frank E., "Dynamic mechanical studies of electrorheological materials: Moderate frequencies" *J. Rheology***35**(3), (Apr. 1991): 399–425.

[100] Gamota, Daniel R. and Filisko, Frank E., "High frequency dynamic mechanical study of an aluminosilicate electrorheological material" *J. Rheology***35**(7), (Oct. 1991): 1411–1425.

[101] Gandhi, M.V., Thompson, B.S. and Choi, S.B., "A New Generation of Innovative Ultra-Advanced Intelligent Composite Materials Featuring Electro-Rheological Fluids: An Experimental Investigation" *J. Composite Materials* **23** (Dec. 1989): 1232–1255.

[102] Gandhi, M.V. and Thompson, B.S., *Smart Materials and Structures* (London: Champan & Hall Publ., 1992).

[103] Gartling, David K. and Phan-Thien, N., "A Numerical Simulation of a Plastic Fluid in a Parallel-Plate Plastometer" *Journal of Non-Newtonian Fluid Mechanics* **14** (1984): 347–360.

[104] Gast, Alice P., and Zukoski, Charles F., "Electrorheological Fluids as Colloidal Suspensions" *Advances in Colloid and Interface Science* **30** (1989): 153–202.

[105] Gavin, H.P. and Hanson, R.D., "Utilization of Active Members to Control the Dynamic Response of Structures" *Proc. US/China/Japan Trilateral Workshop on Structural Control* 5–7 Oct. 1992, Shanghai, China: 277–286.

[106] Gavin, Henri P., Ortiz, David S. and Hanson, Robert D., "Use of ER Fluid Dampers for Reduction of Seismic Structural Response" *Proc. UJNR Workshop on Smart Structures and High Performance Materials and Systems* 14–15 May 1993, Building Research Institute, Tsukuba, Japan.

[107] Gavin, Henri P., Ortiz, David S. and Hanson, Robert D., "Testing and Modeling of a Proto-type ER Damper for Seismic Structural Response Control" *Proc. Int'l Workshop on Structural Control* 5–7 August 1993, Honolulu, HI (Los Angeles: Univ. Southern Calif., USC Publication No. CE-9311): 166–180.

[108] Gavin, Henri P. and Hanson Robert D., "Characterization of an ER Active Member" *Proc. 1994 ASCE Structures Congress* 22-24 Apr. 1994, Atlanta, GA.

[109] Gavin, Henri P. and Hanson, Robert D., "Characterization of an Electrorheological Active Member" *Proc. Fifth U.S. Nat'l Conf. on Earthquake Engineering* 10–14 Jul. 1994, Chicago, IL.

[110] Gavin, Henri P., Hose, Yael D., and Hanson, Robert D., "Design and Control of Electrorheological Dampers" *Proc. First World Conf. on Structural Control* 3–5 Aug. 1994, Pasadena, CA.

[111] Ghanem, R. and Shinozuka, M., "Development of Vibration Suppression Devices Using Variable Dampers" *NCEER Bulletin*, National Center for Earthquake Engineering Research, Buffalo, NY. (Jul. 1992): 5–8.

[112] Goldstein, Gina, "Electrorheological Fludis: Applications begin to gel" *Mechanical Engineering* (Oct. 1990): 48–52.

[113] Gow, C.J. and Zukoski IV, C.F., "The Electrorheological Properties of Polyaniline Suspensions" *Journal of Colloid and Interface Science* **136**(1), (Apr. 1990): 175–188.

[114] Guez, Allon, Eilbert, James L., and Kam, Moshe, "Neural Network Archetecture for Control" *IEEE Control Systems Magazine* Apr. 1988.

[115] Hasse, David, "Electrorheological Liquids" *The Physics Teacher* **31** (Apr. 1993): 218–219.

[116] Halsey, Thomas C. and Toor, Will, "Structure of Electrorheological Fluids" *Physical Review Letters* **65**(22), (26 Nov. 1990): 2820–2823.

[117] Halsey, Thomas C., "The Structure and Dynamics of Electrorheological Fluids" *Proc. Int'l Conf. on Electrorheological Fluids,* 15–16 Oct. 1991, Carbondale, IL, (Singapore: World Scientific): 37–52.

[118] Halsey, Thomas C., Martin, James E. and Adolf, Douglas, "Rheology of Electrorheological Fluids" *Physical Review Letters* **68**(10), (9 Mar. 1992): 1519–1522.

[119] Halsey, Thomas C., "Electrorheological Fluids" *Science* **258** (30 Oct. 1992): 761–766.

[120] Halsey, Thomas C. and Martin, James E., "Electrorheological Fluids" *Scientific American* (Oct. 1993): 58–64.

[121] Hanson, Robert D., and Firmansjah, Jodi, "Energy Concerns for Active Response Control" *Proc. Japan National Symposium/Workshop on Structural Response Control,* 23–25 Mar. 1992, Tokyo, Japan, (Tokyo: Science Council of Japan): 69–75.

[122] Hartsock, D.L., Novak, R.F. and Chaundy, G.J., "ER fluid requirements for automotive devices" *J. Rheology* **35**(7), (Oct. 1991): 1305–1325.

[123] Henke, Russ, "Electromagnetic Fluids Update" *Control Engineering* (Apr. 1992): 57.

[124] Hespel, C., and Jacob, G., "Approximation of nonlinear systems by bilinear ones" *Algebraic and Geometric Methods in Nonlinear Control Theory* (Reidel Publishing Company, 1986): 511–520.

[125] Hill, John C. and Van Steenkiste, Thomas H., "Response times of electrorheological fluids" *J. Applied Physics* **70**(3), (1 Aug. 1991): 1207–1211.

[126] Hill, John C. and Vaz, Nuno A., "Experimental and Theoretical Response Times of Electrorheological Fluids" *Proc. Int'l Conf. on Electrorheological Fluids,* 15–16 Oct. 1991, Carbondale, IL, (Singapore: World Scientific): 280–287.

[127] Holnichi-Szulc, J. Lopez-Almansa, F., Rodellar, J. and Cruells, P., "Optimal location of structural control devices: A progressive collapse analogy" *Proc. 1st European Conf. on Smart Structures and Materials,* 1992, Glasgow, Scotland, (EOS/SPIE and IOP Publ., 1992): 313–316.

[128] Honda, T., Kurosawa, K. and Sasada, T., "Transient Pressure-Drop Fluctuations in Electroviscous Effect" *Japanese J. of Applied Physics* **18**(11), (Nov. 1979): 2059–2063.

[129] Hosseini-Sianaki, A., Bullough, W.A., Firoozian, R., Makin, J. and Tozer, R.C., "Experimental Measurements of the Dynamic Torque Response of an Electro-Rheological Fluid in the Shear Mode." *Proc. Int'l Conf. on Electrorheological Fluids,* 15–16 Oct. 1991, Carbondale, IL, (Singapore: World Scientific): 219–235.

[130] Hrovat, D. Basrak, P. and Rabins, M., "Semi-Active versus Passive or Active Tuned Mass Dampers for Structural Control" *ASCE J. Engineering Mechanics* **109**(3), (Jun. 1983): 691–705.

[131] Hrovat, D., Margolis, D.L. and Hubbard, M., "An Approach Toward the Optimal Semi-Active Suspension" *ASME J. Dynamic Systems, Measurement, and Control* **110** (Sep. 1988): 288–296.

[132] Hunter, L.W. *et. al.* "Optical Effects of Electro-Rheological Fluids" *J. Intelligent Material Systems and Structures* **4** (Jul. 1993) 415–418.

[133] Ikeda, Yoshiki and Kobori, Takuji, "Active-Variable Stiffness System Based on Instantaneous Optimization" *Proc. Japan National Symposium/Workshop on Structural Response Control,* 23–25 Mar. 1992, Tokyo, Japan, (Tokyo: Science Council of Japan)

[134] Inaudi, Jose A. and Kelly, James M., "Active Isolation" *Proc. U.S. Nat'l Workshop on Structural Control Research,* 25–26 Oct. 1990, USC, Los Angeles, CA, (USC Publication No. CE-9013): 125–131.

[135] Ingrasia, Paul, "Michigan Scientist To Receive Patent For 'Smart Fluids' " *The Wall Street Journal* (17 May 1988): 58.

[136] Jaggi, N.K., "Structure and Dynamics of a Dense Dipolar System in an Electric Field and their Relevance to Electrorheological Fluids" *J. Statistical Physics* **64**(5/6), (1991): 1093–1102.

[137] James, A.E., Williams, J.A. and Williams, P.R., "Direct measurement of static yield properties of cohesive suspensions" *Rheologica Acta* **26** (1987): 437–446.

[138] Johnson, A.R., Bullough, W.A. Firoozian, R., Hosseini-Sianaki, A., Makin, J. and Xiao, S., "Testing on a High Speed Electro-Rheological Clutch" *Proc. Int'l Conf. on Electrorheological Fluids,* 15–16 Oct. 1991, Carbondale, IL, (Singapore: World Scientific): 424–441.

[139] Johnston, Peter R., "Axial conduction and the Graetz problem for a Bingham plastic in laminar tube flow" *Int'l J. Heat Mass Transfer* **34**(4/5), (1991): 1209–1217.

[140] Jordan, Therese C. and Shaw, Montgomery T., "Electrorheology" *IEEE Transactions on Electrical Insulation* **24**(5), (Oct. 1989): 849–878.

[141] Jordan, T.C., Shaw, M.T. and McLeish, T.C.B., "Viscoelastic response of electrorheological fluids. II. Field strength and strain dependence" *J. Rheology* **36**(3), (Apr. 1992): 441–463.

[142] Karlin, Samuel and Studden, William J., *Tchebycheff Systems: With Applications in Analysis and Statistics* (New York: John Wiley and Sons, Interscience Publ., 1966).

[143] Karnopp, D., Crosby, M.J. and Harwood, R.A., "Vibration Control Using Semi-Active Force Generators" *ASME J. Engineering for Industry* (May 1974): 619–626.

[144] Katebi, Reza, "Control design for smart flexible structures" *Proc. 1st European Conf. on Smart Structures and Materials,* 1992, Glasgow, Scotland, (EOS/SPIE and IOP Publ., 1992): 305–308.

[145] Kawashima, Kazuhiko, Unjoh Shigeki and Shimizu, Hideyuki, "Earthquake Response Control of Highway Bridges by Variable Damper" *Proc. Japan National Symposium/Workshop on Structural Response Control,* 23–25 Mar. 1992, Tokyo, Japan, (Tokyo: Science Council of Japan)

[146] Kawashima, Kazuhiko, Unjoh Shigeki and Shimizu, Hideyuki, "Experiment on Dynamic Characteristics of Variable Damper" *Proc. Japan National Symposium/Workshop on Structural Response Control,* 23–25 Mar. 1992, Tokyo, Japan, (Tokyo: Science Council of Japan)

[147] Kelly, Louis G., *Handbook of Numerical Methods and Applications* (New York: Addison Wesley Pub. Co., 1967).

[148] Kerr, John, "Freeze! A Solid Chance to Jam Liquid Flow Lines" *The Engineer* 23 July 1981, p 67.

[149] Ketchum, Mark A., and Seim, Charles, "Golden Gate Bridge Seismic Evaluation", T.Y. Lin International, Golden Gate Bridge, Highway and Transportation District, San Francisco. November 7, 1990.

[150] Ketchum, Mark A., and Seim, Charles, "Golden Gate Bridge Seismic Retrofit Studies", T.Y. Lin International, Golden Gate Bridge, Highway and Transportation District, San Francisco. July 10, 1991.

[151] Khan, S.A., Schnepper, C.A. and Armstrong, R.C., "Foam Rheology: III. Measurement of Shear Flow Properties" *J. Rheology* **32**(1), (1988): 69–92.

[152] Kim, Y.S., Wang, K.W. and Lee, H.S., "Feedback control of ER-fluid-based structures for vibration suppression" *Smart Materials and Structures* **1** (1992): 139–145.

[153] Klass, Donald L. and Martinek, Thomas W., "Electroviscous Fluids. I. Rheological Properties" *J. Applied Physics* **38**(1), (Jan. 1967): 67–74.

[154] Klass, Donald L. and Martinek, Thomas W., "Electroviscous Fluids. II. Electrical Properties" *J. Applied Physics* **38**(1), (Jan. 1967): 75–80.

[155] Klein, R.E. and Healy, M.D., "Semi-Active Control of Wind Induced Oscillations in Structures" *Structural Control: Proc. 2nd Int. Symp. on Structural Control* (Waterloo, Ontario: Martinus Hijhoff Publishers, 1985).

[156] Klingenberg, D.J., and Zukoski IV, C.F., "Studies on the Steady-Shear Behavior of Electrorheological Suspensions" *Langmuir* **6** (1990): 15–24.

[157] Klingenberg, D.J., van Swol, Frank, and Zukoski IV, C.F., "The small shear rate response of electrorheological suspensions. I. Simulation in the point-dipole limit" *J. Chemical Physics* **94**(9), (1 May 1991): 6160–6169.

[158] Klingenberg, D.J., van Swol, Frank, and Zukoski IV, C.F., "The small shear rate response of electrorheological suspensions. II. Extension beyond the point-dipole limit" *J. Chemical Physics* **94**(9), (1 May 1991): 6170–6178.

[159] Klingenberg, D.J., Zukoski IV, C.F. and Hill, J.C., "Kinetics of structure formation in electrorheological suspensions" *J. Applied Physics* **73**(9), (1 May 1993): 4644–4648.

[160] Kobori, Takuji and Kamagata, Shuichi, "Evaluation of Necessary Capacity of Active Adjustable Stiffness System" *Proc. Japan National Symposium/Workshop on Structural Response Control,* 23–25 Mar. 1992, Tokyo, Japan, (Tokyo: Science Council of Japan)

[161] Kobori, Takuji, Takahashi, Motoichi, Hiehata, Sigeto, Nasu Tadashi, Niwa, Naoki and Ogasawara, Katsura, "Forced Vibration Test and Earthquake Observation of Actual Seismic Response Controlled Structure with AVS System"

Proc. Japan National Symposium/Workshop on Structural Response Control. 23–25 Mar. 1992, Tokyo, Japan, (Tokyo: Science Council of Japan)

[162] Kobori, T., Takahashi, M., Niwa, N. and Kurata, N., "Analytical Study on the Active Seismic Response Control System Which Provides Variable Structure Characteristics to a High-Rise Building" *Proc. Japan National Symposium/Workshop on Structural Response Control,* 23–25 Mar. 1992, Tokyo, Japan, (Tokyo: Science Council of Japan)

[163] Kobori, T., Motoichi, T., Nasu, T. and Niwa, N., "Seismic Response Controlled Structures with Active Variable Stiffness System" *Earthquake Engineering and Structural Dynamics* **22** (1993): 925–941.

[164] Koh, Severino L., "Theory of a second-order microfluid" *Rheologica Acta* **12** (1973): 418–424.

[165] Korane, Kenneth J., "Putting ER Fluids To Work" *Machine Design* (9 May 1991): 52–60.

[166] Kordonsky, V.I., Korbko, E.V. and Lazareva, T.G., "Electrorheological polymer-based suspensions" *J. Rheology* **35**(7), (Oct. 1991): 1427–1439.

[167] Kovaly, K.A., "Hydraulic fluids are getting smarter" *Hydraulics and Pneumatics* (Oct 1990): 38–39+.

[168] Krieger, Irvin M., "Shear Rate in the Couette Viscometer" *Transactions of the Society of Rheology* **12**(1), (1968): 5–11.

[169] Kuroda, Y., Ura, T. and Morishita, S., "Damping-Controllable Dynamic Damper with Neural Network Based Adaptive Control System" *Proc. 1991 IEEE Joint Conf. on Neural Networks, Vol 2.* Singapore (1991): 1808–1812.

[170] Lang, G.F., "Demystifying Complex Modes", *Sound and Vibration Magazine* Jan. 1989.

[171] Leitmann, G and Reithmeier, E., "Semiactive Control of a Vibrating System by Means of Electrorheological Fluids" *Dynamics and Control* **3** (1993): 7–33.

[172] Lemaire, E., Grasselli, Y. and Bossis, G., "Field induced structure in magneto and electro-rheological fluids" *J. Phys II France* **2** (1992): 359–369.

[173] Lew, H.S. and Young, Y.C., "Entry Flow Into Blood Vessels At Arbitrary Reynolds Number" *J. Biomechanics* **3** (1970): 23–38.

[174] Liang, X.Z. and Han, X.M., "On Chebyshev Approximation in Several Variables (III)" *Approximation, Optimization and Computing: Theory and Applications* (North-Holland: Elsevier Science Publishers, 1990): 125–128.

[175] Lindberg, Gene, "Dirty Oil: the discovery and application of the Winslow effect" *Hydraulics and Pneumatics* (Sep. 1966): 144–145.

[176] Lingard, S., Bullough, W.A. and Shek, W.M, "Tribological performance of an electrorheological fluid" *J. Physics D: Applied Physics* **22** (1989): 1639–1645.

[177] Lipscomb, G.G. and Denn, M.M., "Flow of Bingham Fluids in Complex Geometries" *Journal of Non-Newtonian Fluid Mechanics* **14** (1984): 337–346.

[178] Lou, Zheng, Ervin, Robert D., and Filisko, Frank E., "Behaviors of Electrorheological Valves and Bridges" *Proc. Int'l Conf. on Electrorheological Fluids*, 15–16 Oct. 1991, Carbondale, IL, (Singapore: World Scientific): 398–423.

[179] Lou, Zheng, Ervin, Robert D., and Filisko, Frank E., "An Electro-Rheological Servo Position Control System" *Proc. Int'l Conf. on Electrorheological Fluids*, 15–16 Oct. 1991, Carbondale, IL, (Singapore: World Scientific): 453–464.

[180] Lou, Zheng, Ervin, Robert D. and Filisko, Frank E., "A Preliminary Parametric Study of Electrorheological Dampers" *Electrorheological Flows* FED-Vol. **164** (ASME, 1993): 143–155.

[181] Luco, J.E., Wong, H.L., and Mita, A., "Active Control of the Seismic Response of Structures by Combined Use of Base Isolation and Absorbing Boundaries" *Earthquake Engineering and Structural Dynamics* **21** (1992): 525–541.

[182] Lykov, A.V., Shul'man, Z.P., Gorodkin, R.G., and Matsepuro, A.D. "Mechanical Behavior of Electroviscous Nonaqueous Disperse Systems in Shear Flow in a Transverse Electric Field" *J. Engineering Physics* **18** (1970): 669–674.

[183] Mahmoodi, P., "Structural Dampers" *ASCE J. Structural Division* **95**(ST8), (Aug. 1969).

[184] Mahjoob, M.J., Martin, H.R. and Ismail, F., "Distributed Vibration Control Using Electrorheological Fluids," *Proc. IMAC 11* 1–4 Feb 1993, Kissimmee, FL (SEM): 768–774.

[185] Mandell, Mel, "Smart Fluids: Wavelet of the Future?" *High Technology Business* (Jul.-Aug. 1989): 20–23.

[186] Margolis, Donald L. and Vahdati, Nader, "The Control of Damping in Distributed Systems Using ER-Fluids" *Proc. 2nd Int'l Conf. on ER Fluids*, 7–9 Aug. 1989, Raleigh, NC. (Lancaster: Technomic Publishing Co.): 326–348.

[187] Marshall, Louise, Zukoski IV, Charles F., and Goodwin, James W., "Effects of Electric Fields on the Rheology of Non-aqueous Concentrated Suspensions" *J. Chemical Soc., Faraday Trans. 1* **85**(9), (1989): 2785–2795.

[188] Martin, James E., Odenik, Judy and Halsey, Thomas C., "Evolution of Structure in a Quiescent Electrorheological Fluid" *Physical Review Letters* **69**(10), (7 Sep. 1992): 1524–1527.

[189] Masri, S.F. and Caughey, T.K., "A Nonparametric Identification Technique for Nonlinear Dynamic Problems" *Trans. ASME J. Applied Mechanics* **46** (Jun. 1979): 433–447.

[190] McClamroch, N. Harris, Ortiz, David S., Gavin, Henri P., and Hanson, Robert D., "Electrorheological Dampers and Semi-Active Structural Control" *Proc. 33rd IEEE Conf. on Decision and Control,* Orlando, FL, 1994.

[191] McLeish, T.C.B., Jordan, T. and Shaw, M.T., "Viscoelastic response of electrorheological fluids. I. Frequency dependence" *J. Rheology* **35**(3), (Apr. 1991): 427–449.

[192] Mewis, J., "Thixotropy — A General Review" *J. Non-Newtonian Fluid Mechanics* **6** (1979): 1–20.

[193] Miyazaki, M. and Mitsusaka, Y., "Design of a building with 20 percent or greater damping" *Proc. 10th World Conf. on Earthquake Engineering* **7** 19–24 Jul. 1992, Madrid, Spain, (Rotterdam: A.A. Balkema): 4143–4148.

[194] Mokeev, A.A., Korobko, E.V. and Vedernikova, L.G., "Structural viscosity of electrorheological fluids" *J. Non-Newtonian Fluid Mechanics* **42** (1992): 213–230.

[195] Montgomery, Allan R., "Sealed Dashpots for Precise Control" *Machine Design* (7 Aug. 1986): 76+.

[196] Morishita, Shin and Mitsui, Jun'ichi, "Squeeze Film Damper as an Application of Electro-Rheological Fluid" *Proc. Int. Conf. on Rotordynamics.* 10–13 Sep. 1990, Lyon, France.

[197] Morishita, Shin and Mitsui, Jun'ichi, "Controllable Shock Absorber System (An Application of Electro-Rheological Fluid)" SAE Paper Offer 90FL–10.

[198] Morishita, Shin and Ura, Tamaki, "Semi-Active Structural Vibration Control System" *Proc. Japan National Symposium/Workshop on Structural Response Control,* 23–25 Mar. 1992, Tokyo, Japan, (Tokyo: Science Council of Japan)

[199] Morishita, Shin and Mitsui, Jun'ichi, "An Electronically Controlled Engine Mount Using Electro-rheological Fluid" *SAE paper 922290,* (1992).

[200] Morishita, Shin and Mitsui Jun'ichi, "Controlable Squeeze Film Damper (An Application of Electro-Rheological Fluid)" *Trans. ASME J. Vibration and Accoustics* **114** (Jul. 1992): 354–357.

[201] Morishita, Shin and Ura, Tamaki, "ER Fluid Applications of Vibration Control Devices and an Adaptive Neural-Net Controller" *J. Intelligent Material Systems and Structures* **4** (Jul. 1993)

[202] Mors, Paulo M., Botet, Robert and Remi, Jullien, "Cluster-cluster aggregation with dipolar interactions" *J. Physics A: Mathematical and General Physics* **20** (1987): L975–L980.

[203] Mottershead, J.E. and Stanway, R., "Identification of N^{th} Power Velocity Damping" *J. Sound and Vibration* **105**(2), (1986): 309–319.

[204] Mullins, Peter J., "Fluid Powerful!" *Automotive Industries* (Sept. 1988): 68–69.

[205] Naj, Amal Kumar, "Engineers Want New Buildings to Behave Like Human Beings" *The Wall Street Journal* (20 Jan. 1994): B1+.

[206] Nguyen, Q.D. and Boger, D.V., "Measuring the Flow Properties of Yield Stress Fluids" *Annual Review of Fluid Mechanics* **24** (1992): 47–88.

[207] Nishimura I., Kobori, T., Sakamoto, M., Koshika, N., Sasaki, K. and Ohrui, S., "Acceleration feedback method applied to active tuned mass damper" *Proc. 1st European Conf. on Smart Structures and Materials,* 1992, Glasgow, Scotland, (EOS/SPIE and IOP Publ., 1992): 301–304.

[208] Noguchi, et al., "Electroviscous Liquid-Filled Suspension Device and Control Damping Device Therefore" *U.S. Patent 4,858,733* (22 Aug. 1989).

[209] Osada, Yoshihito and Ross-Murphy, Simon B., "Intelligent Gels" *Scientific American* (May 1993): 82–87.

[210] Ota, Montonori and Miyamoto, Tetsuo, "Many-body effect in the static yield stress of electrorheological fluid" *J. Applied Physics* **74**(2), (15 Jul. 1993): 938–941.

[211] Otsubo, Y., "Electrorheological properties of silica suspensions" *J. Rheology* **36**(3), (Apr. 1992): 479–496.

[212] Oz, H., "Fundamental Aspects of Structure Control" *Structural Control: Proc. 2nd Int. Symp. on Structural Control* (Waterloo, Ontario: Martinus Hijhoff Publishers, 1985).

[213] Parkinson, Gerald, "Liquids with an IQ" *Chemical Engineering* (Nov. 1992): 35+.

[214] Peel, D.J. and Bullough, W.A., "Miscellaneous Electro-Rheological Phenomena, Part III" *Proc. 2nd Int'l Conf. on ER Fluids,* 7–9 Aug. 1989, Raleigh, NC. (Lancaster: Technomic Publishing Co.): 141–157.

[215] Peel, D.J. and Bullough, W.A., "Effect of Flow Rate, Excitation Level and Solids Content on the Time Response in an Electro-Rheological Valve" *J. Intelligent Material Systems and Structures* **4** (Jan. 1993): 54–64.

[216] Pennisi, E., "New suspension may smooth maglev ride" *Science News* (25 Jan. 1992): 55.

[217] Petek, Nicholas K., Goudie, Robert J. and Boyle, Frederick P., "Actively Controlled Damping in Electrorheological Fluid-Filled Engine Mounts" *SAE paper 881785* (1988): 1–8.

[218] Petek, Nicholas K., "Shock absorber uses electrorheological fluid" *Automotive Engineering* **100**(6), (Jun. 1992): 27–30.

[219] Phelan, Mark, "Fluids pack puch: Charged liquids could replace moving parts" *Ward's Auto World* (Feb. 1987): 95+.

[220] Phillips, R.W., *Engineering Applications of Fluids with a Variable Yield Stress* Ph.D. Dissertation, U.C. Berkeley, Dept. of Mechanical Engineering, 1969.

[221] Phillips, Robert W. and Auslander, David M. "The Electroplastic Flow Modulator," *Proc. Symp. Measurement in Science and Industry* 1971, Pittsburgh, PA: 1243–1251.

[222] Pierre, Donald A., *Optimization Theory With Applications* (New York: Dover Press, 1996).

[223] Pinkos, A., Shtarkman, E., and Fitzgerald, T., "An Actively Damped Passenger Car Suspension System with Low Voltage Electro-Rheological Magnetic Fluid" *SAE paper 930268* (Mar. 1993): 87–92.

[224] Pinkos, A. and Shtarkman, E., "Active damping using ERM fluids" *Automotive Engineering* (Jun. 1993): 19–23.

[225] Pool, Robert, "The Fluids With a Case Of Split Personality" *Science* **247** (9 Mar. 1990): 1180–1181.

[226] Press, William H. et al., *Numerical Recipes in C*, (Cambridge, England: Cambridge University Press, 1988).

[227] Rajagopal, K.R. and Wineman, A.S., "Flow of electrorheological materials" *Acta Mechanica* **91** (1992): 57–75.

[228] Richardson, M.H. and Formenti, D.L., "Parameter Estimation from Frequency Response Measurements Using Rational Fraction Polynomials" *Proc. 1st Int'l Modal Analysis Conf.* Orlando, FL, 1982.

[229] Richardson, M.H. and Formenti, D.L., "Global Curve-Fitting of Frequency Response Measurements Using the Rational Fraction Polymomial Method" *Proc. 3rd Int'l Modal Analysis Conf.* Orlando, FL, 1985.

[230] Rothman, Tony, "Phase Transition: Electrorheological fluids flourish in drought" *Scientific American* **259** (Sep. 1988): 30–31.

[231] Rowand, Roger, "Frank Filisko's fluids: Prof's electro-rheological fluids hold promise for hydraulics" *Automotive News* (8 Aug. 1988): E24.

[232] Ruthern, Russel, "Fickle Fluids" *Scientific American* (Jul. 1992).

[233] Schlichting, H., *Boundary Layer Theory, 6th ed.* (New York: McGraw Hill, 1968)

[234] Schmidt, F.W., "Laminar Flows in Inlet Sections of Tubes and Ducts" *AIChE J.* **15**(4), (Jul, 1969): 612–614.

[235] Schubring, Adam W. and Filisko, Frank E., "Study of the Variation of the Substitutional Atoms in Amorphous Alumino- Silicates as an Electrorheological Material" *Polymer Preprints* **35**(2) (Aug. 1994): 369–370.

[236] Scott, David and Yamaguchi, Jack, "Solidifying fluid transforms clutches and flow valves" *Automotive Engineering* **91**(11), (Nov. 1983): 61–66.

[237] Scott, David, "Amazing hardening fluid opens a new world of hydraulic devices" *Popular Science* (Apr. 1984): 82–85.

[238] Scott, David and Yamaguchi, Jack, "ER Fluid devices near commercial stage" *Automotive Engineering* **93**(11), (Nov. 1985): 75–79.

[239] See, Howard, and Doi, Masao, "Aggregation Kinetics in Electro-Rheological Fluids" *J. Physical Soc. Japan* **60**(8), (Aug. 1991): 2778–2782.

[240] Shih, C.Y., Tsuei, Y.G., Allemang, R.J., and Brown, D.L., "A Frequency Domain Global Parameter Estimation Method for Multiple Reference Frequency Response Measurements" *Journal of Mechanical Systems and Signal Processing* **2**(4), (1988).

[241] Shulman, Z.P., Gorodkin, R.G., Korobko, E.V. and Gleb, V.K., "The Electrorheological Effect and its Possible Uses" *J. Non-Newtonian Fluid Mechanics* **8** (1981): 29–41.

[242] Shulman, Z.P., Khusid, B.M., Khizhinskii, B.P. and Korobko, E.V., "Characteristics of an Electrorheological Damper in a Vibration Insulator" *J. Engineering Physics* **52**(2), (1987): 175–179.

[243] Shulman, Z.P., Khusid, B.M., Korobko, E.V. and Khizhinskii, B.P., "Damping of Mechanical-Systems Oscillations by a Non-Newtonian Fluid with Electric-Field Dependent Parameters" *J. Non-Newtonian Fluid Mechanics* **25** (1987): 329–346.

[244] Shulman, Z.P., Korobko, E.V. and Yanovskii, Yu.G., "The Mechanism of the Viscoelastic Behavior of Electrorheological Suspensions" *J. Non-Newtonian Fluid Mechanics* **33** (1989): 181–196.

[245] Siem, C. and Ketchum, M. A., "Golden Gate Bridge Transit Feasibility Study", T.Y. Lin International, Golden Gate Bridge, Highway and Transportation District, San Francisco, CA. (Oct. 1990).

[246] Simmonds, A.J., "Electro-rheological valves in a hydraulic circuit" *IEE Proceedings-D* **138**(4), (Jul. 1991): 400–404.

[247] Slotine, Jean-Jacques E., "Sliding controller design for non-linear systems," *Int'l J. Control* **40**(2), (1984): 421–434.

[248] Snyder, Martin Avery, *Chebyshev Methods in Numerical Approximation* (Englewood Cliffs, N.J.: Prentice Hall, 1966).

[249] Soong, T.T., *Active Structural Control: Theory and Practice*, (Essex, England: Longman Scientific and Technical, 1990).

[250] Sorenson, H.W., "Parameter and state estimation: introduction and interrelation", *IFAC Identification and System Parameter Estimation* 1982, 85–87.

[251] Sprecher A.F., Carlson, J.D. and Conrad, H., "Electrorheology at Small Strains and Strain Rates of Suspensions of Silica Particles in Silicone Oil" *Materials Science and Engineering* **95** (1987): 187–197.

[252] Sproston, J.L. *et. al.* "A Prototype Automotive Engine Mount Using Electrorheological Fluids" *J. Intelligent Material Systems and Structures* **4** (Jul. 1993): 418–419.

[253] Spurk, J.H. and Huang, Zhen, "Electrorheological Material under Oscillatory Shear" *J. Intelligent Material Systems and Structures* **4** (Jul. 1993): 403–408.

[254] Standrud, Halvor T., "Voltage Blocks Flow in Valveless Vibrator" *Hydraulics and Pneumatics* (Jul. 1966): 126.

[255] Standrud, Halvor T., "Electric-field valves inside cylinder control vibrator" *Hydraulics & Pneumatics* (Sep. 1966): 139–143.

[256] Stangroom, J.E., "Electrorheological Fluids" *Physics and Technology* **14** (1983): 290–296.

[257] Stangroom, J.E., "The Bingham Plastic Model of ER Fluids and Its Implications" *Proc. 2nd Int'l Conf. on ER Fluids,* 7–9 Aug. 1989, Raleigh, NC. (Lancaster: Technomic Publishing Co.): 199–206.

[258] Stangroom, J.E., "Basic Considerations of Flowing Electrorheological Fluids" *J. Statistical Physics* **64**(5/6), (1991): 1059–1072.

[259] Stanway, R. Sproston, J.L. and Stevens, N.G., "Non-Linear Identification of an Electro-rheological Vibration Damper" *IFAC Identification and System Parameter Estimation* (1985): 195–200.

[260] Stanway, R. Sproston, J.L. and Stevens, N.G., "Non-Linear Modelling of an Electro-Rheological Vibration Damper" *J. Electrostatics* **20** (1987): 167–184.

[261] Stanway, R. Sproston, J.L. and Firoozian, "Identification of the Damping Law of an Electro-Rheological Fluid: A Sequential Filtering Approach" *J. Dynamic Systems, Measurement, and Control* **111** (Mar. 1989): 91–96.

[262] Stanway, R. Sproston, J.L., Prendergast, M.J., Case, J.R. and Wilne, C.E., "ER fluids in the squeeze-flow mode: an application to vibration isolation" *J. Electrostatics* **28** (1992): 89–94.

[263] Stevens, N.G., Sproston, J.L. and Stanway, R., "Experimental Evaluation of a Simple Electroviscous Damper" *J. Electrostatics* **15** (1984): 275–283.

[264] Stevens, N.G., Sproston, J.L. and Stanway, R., "The Influence of Pulsed D.C. Input Signals on Electrorheological Fluids" *J. Electrostatics* **17** (1985): 181–191.

[265] Stevens, N.G., Sproston, J.L. and Stanway, R., "On the Mechanical Properties of Electro-Rheological Fluids" *ASME J. Applied Mechanics* **54** (Jun. 1987): 456–458.

[266] Sugimoto, Noboru, "Winslow effect in ionic exchange resin dispersion" *Bulletin of the JSME* **20**(149), (Nov. 1977): 1476–1483.

[267] Tachibana, E., Inoue, Y. and Creamer B.G., "Fuzzy Theory for the Active Control of the Dynamic Response in Buildings" *Microcomputers in Civil Engineering* **7** (1992): 179–189.

[268] Tanaka, K., Yoshida, T. and Koyama, K., "Transient Response of ER Fluids" *Proc. Int'l Conf. on Electrorheological Fluids,* 15–16 Oct. 1991, Carbondale, IL, (Singapore: World Scientific): 289–299.

[269] Tao, R., Woestman, J.T. and Jaggi, N.K., "Electric field induced solidification" *Applied Physics Letters* **55**(18), (30 Oct. 1989): 1844–1849.

[270] Tao, R. and Sun, R., "Three-Dimensional Structure of Induced Electrorheological Solid" *Physical Review Letters* **67**(3), (15 Jul. 1991): 398–401.

[271] Tao, R., "Electric-field-induced phase transition in electrorheological fluids" *Physical Review E* **47**(1), (Jan. 1993): 423–426.

[272] Tao, R., "Phase Transition and Structure of Electrorheological Fluids" *Electrorheological Flows* FED-Vol. **164** (ASME, 1993): 11–19.

[273] Tappley, Byron D., ed., *Eshbachs Handbook of Engineering Fundamentals, 4th ed.*, 1990

[274] Tessler, Sandra Rubin, "Smart Materials" *Technology Review* **92** (Apr. 1989): 8–9.

[275] Thurston, G.B. and Caertner, E.B., "Viscoelasticity of electrorheological fluids during oscillatory flow in a rectangular channel" *J. Rheology* **35**(7), (Oct. 1991): 1327–1343.

[276] Tsai, C.S. and Lee, H.H., "Applications of Viscoelastic Dampers to High-Rise Buildings" *ASCE J. Structural Engineering* **119**(4), (Apr. 1993): 1222–1233.

[277] Tseitlin, A.I. and Kusainov, A.A. *Role of Internal Friction in Dynamic Analysis of Structures*, (Rotterdam: A.A. Balkema, 1990).

[278] Uejima, Hideyuki, "Dielectric Mechanism and Rheological Properties of Electro-Fluids" *Japanese J. Applied Physics* **11**(3), (Mar. 1972): 319–326.

[279] Ushijima, T., Takano, K. and Kojima, H., "High Performance Hydraulic Mount for Improving Vehilce Noise and Vibration" *SAE paper 880073* (1988): 1–9.

[280] Ushijima, T., Takano, K. and Takeshi, N., "Rheological Characteristics of ER Fluids and Their Appliation to Anti-Vibration Devices with Control Mechanism for Automobiles" *SAE paper 881787* (1988): 1–9.

[281] Utkin, Vadim I., "Variable Structure Systems with Sliding Modes," *IEEE Trans. on Automatic Control* **AC-22**(2), (Apr. 1977): 212–220.

[282] Vinogradov, G.V., Shul'man, Z.P., Yanovskii, Yu.G., Barancheeva, V.V., Korobko, E.V. and Bukovich, I.V., "Viscoelastic Behavior of Electrorheological Suspensions" *J. Engineering Physics* **50**(4), (1986): 429–432

[283] von Hippel, Arthur R., *Dielectrics and Waves* (Cambridge, Mass: M.I.T. Press, 1954)

[284] von Hippel, Arthur R., ed., *Dielectric Materials and Applications* (Cambridge, Mass: M.I.T. Press, 1954)

[285] Vradis, George C. and Otugen, M. Volkan, "The Flow of Bingham Plastics of a Sudden Expansion in a Pipe" *Recent Advances in Non-Newtonian Flows* AMD-Vol. **153**/PED-Vol. **141**, (ASME, 1992): 129–136.

[286] Vradis, George C., Dougher, J. and Kumar, S., "Entrance pipe flow and heat transfer for a Bingham plastic" *Int'l J. Heat Mass Transfer* **36**(3), (1993): 543–552.

[287] Walton, I.C. and Bittleston, S.H., "The axial flow of a Bingham plastic in a narrow eccentric annulus" *J. Fluid Mechanics* **222** (1991): 39–60.

[288] Wang, K.C., McLay, R., and Carey, G.F., "ER Fluid Modelling" *Proc. 2nd Int'l Conf. on ER Fluids,* 7–9 Aug. 1989, Raleigh, NC. (Lancaster: Technomic Publishing Co.): 41–52.

[289] Wang, K.W. and Kim, Y.S., "Semi-Active Vibration Control of Flexible Structures," *Proc. ASME Int'l Computers in Engineering Conf. and Exposition*, Vol 1., 1991: 449–454.

[290] Weidlinger, Paul and Ettouney, Mohammed, "Sequential Coupling: New Structural Connection for Seismic Control" *ASCE J. Structural Engineering* **119**(1), (Jan. 1993): 181–201.

[291] Weiss, Keith D. and Carlson, J. David, "Macroscopic Behavior of Electrorheological Fluids: Techniques for Measuring Response Time" *Proc. Int'l Conf. on Electrorheological Fluids,* 15–16 Oct. 1991, Carbondale, IL, (Singapore: World Scientific): 264–279.

[292] Weiss, Keith D., Carlson, J. David, and Coulter, John P., "Material Aspects of Electrorheological Systems" *J. Intelligent Material Systems and Structures* **4** (Jan. 1993): 13–34.

[293] Werbos, Paul J., "Links Between Artificial Neural Networks (ANN) and Statistical Pattern Recognition" *Artificial Neural Networks and Statistical Pattern Recognition* (Elsevier Science Publishers B.V. 1991).

[294] White, Frank M. *Viscous Fluid Flow* (New York: McGraw Hill, 1974).

[295] White, Frank M. *Fluid Mechanics* (New York: McGraw Hill, 1979).

[296] Whittle, Martin, "Modelling two-phase fluids" *Physics World* **2** (Aug. 1989): 39–42.

[297] Whittle, Martin, "Computer Simulation of an Electrorheological Fluid" *J. Non-Newtonian Fluid Mechanics* **37** (1990): 233–263.

[298] Whittle, M. Firoozian, R., Peel, D.J. and Bullough, W.A., "A Model For The Electrical Characteristics of an ER valve" *Proc. Int'l Conf. on Electrorheological Fluids,* 15–16 Oct. 1991, Carbondale, IL, (Singapore: World Scientific): 343–366.

[299] Whittle, M. and Bullough, W.A., "The structure of smart fluids" *Nature* **358** (30 Jul. 1992): 373.

[300] Whittle, M., Firoozian, R., Peel, D.J., and Bullough, W.A., "Decomposition of the Pressure Response in an ER Valve Control System" *J. Intelligent Material Systems and Structures* **5** (Jan. 1994): 105–111.

[301] Williams, E.W., Rigby, S.G., Sproston, J.L. and Stanway, R., "Electrorheological fluids applied to an automotive engine mount" *J. Non-Newtonian Fluid Mechanics* **47** (1993): 221–238.

[302] Wilson, S.D.R., "Squeezing flow of a Bingham material" *J. Non-Newtonian Fluid Mechanics* **47** (1993): 211–219.

[303] Winslow, W.M., "Induced Fibration of Suspensions" *J. Applied Physics* **20** (Dec, 1949): 1137–1140.

[304] Yang, Ji-Bin, "Rheological Characteristics of Some Electro-Rheological Fluids With High Shear Strength" *Electrorheological Flows* FED-Vol. **164** (ASME, 1993): 85–97.

[305] Yang, Zhi-chun, Zhao, Ling-cheng, and Jiang, Jie-sheng, "Semi-Active Control of Structural Nonlinear Flutter" *Proc. IMAC 11* 1–4 Feb 1993, Kissimmee, FL (SEM): 775–780.

[306] Young, P., "Recursive identification, estimation, and control" *Handbook of Statistics* (Elsevier Science Publisher, 1985): 213–255.

[307] Yoshimura, Ann S. and Prud'homme, Robert K., "A Comparison of Techniques for Measuring Yield Stresses" *J. Rheology* **31**(8), (1987): 699–710.

[308] Yoshimura, Ann S. and Prud'homme, Robert K., "Response of an elastic Bingham fluid to oscillatory shear" *Rheologica Acta* **26** (1987): 428–436.